Neutral Pion Production in High Energy Heavy Ion Collisions at the PHENIX Experiment

Egyetemi doktori (PhD) értekezés

Tarján Péter
témavezető: Dávid Gábor, PhD

Debreceni Egyetem
Természettudományi Doktori Tanács
Fizika Doktori Iskola
Debrecen, 2009.

Contents

Introduction

This dissertation describes the work done at the PHENIX detector on the Relativistic Heavy Ion Collider of Brookhaven National Laboratory (USA), with Gabor David (PhD) as my advisor.

The topic of the thesis is the measurement of neutral pion spectra in high energy heavy ion (specifically, Au + Au) collisions. The prerequisite of this work (or indeed, of any other high energy physics analysis), the calibration of the detector is also described.

One of the main goals of RHIC and the PHENIX detector is to allow us a glimpse into the properties of nuclear matter under extreme conditions and to determine if the Quark Gluon Plasma predicted by theory is created. This particular analysis takes us one step closer to achieving that goal, although it is by no means the final word on the subject.

Regarding the order and the titles of the chapters, I have deviated from the letter of the rules laid down in the faculty regulations; I feel, however, that I did not violate their spirit. The first chapter gives an insight into the theory of the Quark Gluon Plasma. Chapters 2 and 3 deal with the collider and the PHENIX detector. Chapter 4 introduces the Electromagnetic Calorimeter of PHENIX, which can be regarded both as previous work and as "Material and method", since the calibrations described there incorporate my work too. Chapter 5 is about our experimental technique, our methods. Chapter 6 discusses the results. The thesis is summarized in English and Hungarian in Chapters 7 and 8. After the bibliography, Appendix A lists the explanations of acronyms used in the text; Appendix B lists my publications relevant to the dissertation.

I would like to thank everyone who directly or indirectly helped completing this dissertation: my advisor, my friends, colleagues and family.

Chapter 1

Quark matter

What is the world made of? What holds it together? These are questions that have fascinated countless thinkers over the ages. Our knowledge about the structure of the world has undergone substantial transformations. Today, the Standard Model of particle physics describes the world as being built of "bricks" called fermions, which are held together by 4 fundamental forces: the gravitational, the electromagnetic, the weak and the strong force. Apparently different as these forces are, there are signs which give basis to the suspicion that under certain circumstances these forces can be "unified", that is, their effects described in a common mathematical framework. This unification has already been done for the electromagnetic and the weak forces and thus we can talk about the "electroweak" force. The strong force, however, has so far resisted the unification attempts due to some of its peculiar characteristics.

One of the most fascinating aspects of the strong force is that its particles, the quarks and the gluons can never be observed in a free state, only confined in composite particles, hadrons. This impossibility does not originate from the imperfections of our experimental apparatus, it is in the very nature of the strong force. Yet according to nuclear theorists [1], [2], this behavior changes under extreme conditions. At high temperatures and/or high densities, nuclear matter will undergo a phase transition and quarks and gluons become deconfined:

> When the energy density ϵ exceeds some typical hadronic value $\sim 1\,\mathrm{GeV/fm^3}$, matter no longer consists of separate hadrons (protons, neutron, etc.), but as their fundamental constituents, quarks and gluons. Because of the apparent analogy with similar phenomena

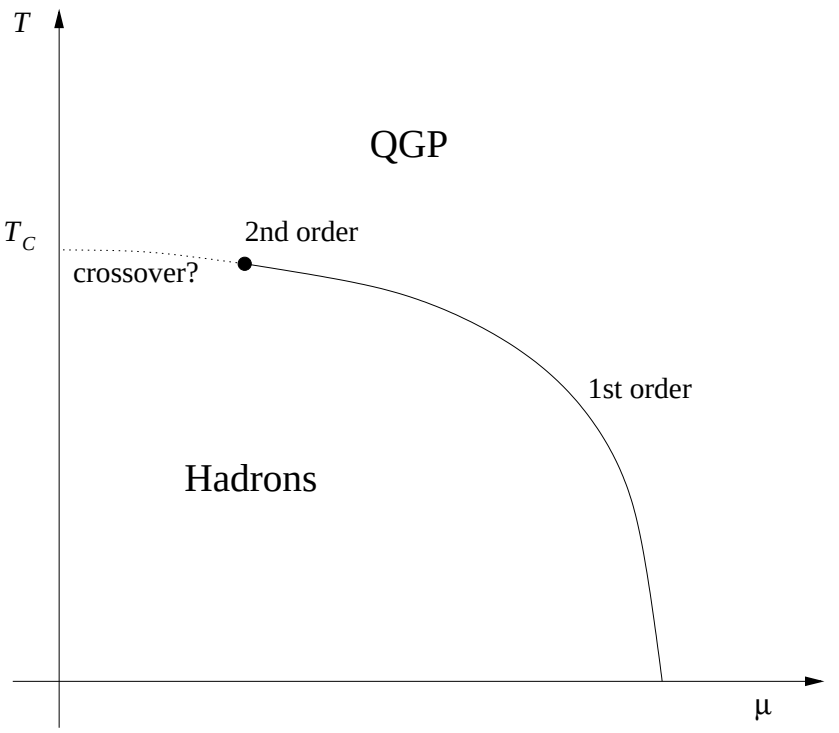

Figure 1.1: Simplified theoretical phase diagram of nuclear matter: temperature T vs baryon chemical potential μ.

> in atomic physics we may call this phase of matter the QCD (or quark-gluon) plasma.

A simplified theoretical phase diagram of nuclear matter is shown in Fig. 1.1. It shows that to cross from hadronic matter to QGP, one must produce extreme high temperatures and/or high baryon densities, but the order of the phase transition may depend on the path chosen. The exact order of the phase transition is not known.

Both theory and experiment suggest that collisions at RHIC are characterized by low net baryon density [3], where theory predicts a smooth transition

from one phase to the other. This makes it more difficult to determine if such a transition has occurred.

It is relatively simple to estimate the critical temperature ($T_C \approx 170\,\mathrm{MeV}$) and the critical energy density ($\epsilon_C \approx 1\,\mathrm{GeV/fm^3}$). In this (experimentally achievable) energy range, however, the value of the strong coupling constant is of order unity, which makes perturbative QCD calculations unreliable.

Thus, *creating* the QGP is not the main difficulty, the real challenge is how to *observe* it and measure its properties. The experimental problems are the following:

- probably smooth transition from one phase to the other, no sharp changes
- theoretically difficult to make predictions
- even if we produce the QGP, it lasts only a fraction of a second, then it thermalizes and reverts back to normal nuclear matter.

It is therefore imperative that we examine as many *signatures* of the QGP as possible and compare and combine the results acquired with different methods to get a picture of what is happening inside that hot and dense medium. One of these signatures is *jet quenching* [4].

The phenomenon of jet quenching means that if a hot and dense, strongly interacting medium is formed, it slows down and/or absorbs quarks flying out of it. This in turn means that the hadrons that the quarks hadronize into will be produced with lower energies and in lower numbers. Then the hadrons are said to be *suppressed*. Thus suppression is one the many signatures of the QGP.

Chapter 2

The Relativistic Heavy Ion Collider

The Relativistic Heavy Ion Collider, or RHIC for short [5], at Brookhaven National Laboratory in the USA is a unique machine designed to collide nuclei of practically any type. The main job of RHIC is to create temperatures above the critical temperature for hadronic matter and provide a means to investigate the region that lies beyond. RHIC achieves that goal by accelerating heavy ions to a very high energy and colliding them. QCD suggests that in the resulting fleeting "fireball" hadronic matter "melts", losing all its properties as we know them and an entirely new form of matter, the so-called Quark-Gluon Plasma, or QGP arises. Four detectors are built along the RHIC ring to record everything coming out of the collisions. The information acquired is used to determine the characteristics of the collision; find out if the QGP has been created; investigate the properties of matter beyond the critical temperature; and map how the transition occurs.

The idea of RHIC was born in 1983, with a recommendation of the US Nuclear Science Advisory Committee, the Department of Energy and the National Science Foundation. Support for R&D began in 1987. Detector development started in 1990 and the actual construction of RHIC began a year later. The accelerator was completed in 1999 and the physics program started in 2000.

RHIC is by no means a standalone machine, but rather an extension to Brookhaven's already existing accelerator complex. The existing expertise and infrastructure were fully utilized and built upon in the design and construction

of RHIC. Some of the existing infrastructure that contributed to the reduction of the cost was that the tunnel of the machine was already dug: it was left over from the earlier abandoned ISABELLE project[1]; and so was a 25 kW helium refrigerator. Then, of course, the existing accelerator chain can be used to pre-accelerate heavy ions (and protons) before injecting them into RHIC.

The collider consists of two quasi-circular concentric accelerators, which can independently accelerate, store and collide virtually any types of ions. The maximum design energy for gold ions is 100 GeV per nucleon, with a luminosity of $2 \times 10^{26}\,\mathrm{cm}^{-2}\mathrm{s}^{-1}$. (By the fourth running period there has been a factor of 2 improvement over the design goal and more is expected.) The maximum design energy for protons is 250 GeV, with a luminosity of $1.4 \times 10^{31}\,\mathrm{cm}^{-2}\mathrm{s}^{-1}$. The two rings are denoted "Blue Ring" and "Yellow Ring" and beams circulate in them clockwise and counter-clockwise, respectively. The rings (3.8 km in circumference) have 6 arc sections, each ≈ 356 m long and 6 insertion sections, each ≈ 277 m long, with a collision point at their center. Each arc section is composed of 11 FODO cells with a modified half-cell on each end. Each full cell consists of two 9.45 m long dipoles and two composite units, each containing one 0.75 m long sextupole, one 1.11 m long quadrupole and one 0.50 m long corrector assembly. In the arc sections, the counter-rotating beams are separated by 90 cm horizontally. Two dipole magnets (DX and D0) on each side of the collision points steer ions to a co-linear path for head-on collisions. The dipole magnets, along with the rest of the magnets in RHIC (a total of 1740) are superconducting.

The RHIC acceleration scenario for Au ion beams is shown in Fig. 2.1. Three accelerators in the injector chain will successively boost the energy of ions, and strip electrons from the atoms. Negatively charged gold ions from the pulsed sputter ion source at the Tandem Van de Graaff (100 mA, 700 ms) are partially stripped of their electrons with a foil at the Tandem's high voltage terminal, and then accelerated to the energy of 1 MeV per nucleon by the second stage of the Tandem. After further stripping at the exit of the Tandem and a charge selection by bending magnets, beams of gold ions with the charge state of +32 are delivered to the Booster Synchrotron and accelerated to 95 MeV/A. Ions are stripped again at the exit from the Booster to reach the charge state of +77, a helium-like ion, and injected to the Alternating Gradient Synchrotron (AGS) for acceleration to the RHIC injection energy of 10.8 GeV/A. Gold ions, injected into the AGS in 24 bunches, are debunched and then rebunched to

[1]ISABELLE was a 200+200 GeV proton-proton colliding beam particle accelerator partially built by the United States government at Brookhaven National Laboratory in Upton, New York, before it was cancelled in July, 1983. [6]

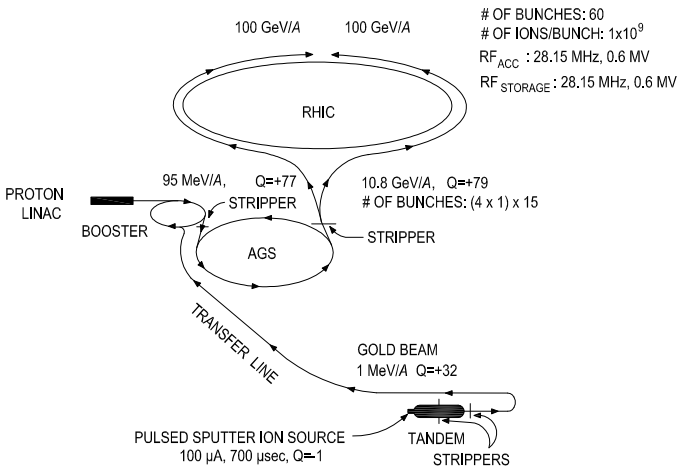

Figure 2.1: The RHIC accelerator complex.

four bunches at the injection front porch prior to the acceleration. These four bunches are ejected at the top energy, one bunch at a time, and transferred to RHIC through the AGS-to-RHIC Beam Transfer Line. Gold ions are fully stripped to the charge state of +79 at the exit from the AGS.

Acceleration and storage of beam bunches at RHIC uses two RF systems, one operating at 28 MHz, the other operating at 197 MHz. The synchrotron phase transition of the RHIC lattice is at $\gamma_{\mathrm{T}} = 24.7$; thus all ions, except protons, must go through this transition. The RHIC collider is the first superconducting accelerator that passes through the synchrotron phase transition and associated beam instability.

Polarized protons are injected from the existing 200 MeV Linac for the spin physics program with collisions of polarized protons. Polarized beams become increasingly difficult to maintain with increasing energy due to the increased density and strength of the spin resonances. RHIC is by far the highest energy polarized beam facility yet envisaged and a different approach was necessary. The use of Siberian Snakes [7] to preserve beam polarization has been postulated for a long time and has been implemented at RHIC. A Snake providing a full 180° spin flip was designed and fabricated as part of this program. Each Snake is constructed from four 2 m helical dipole modules. Four such Siberian Snakes that were built as part of the RIKEN-BNL Spin Physics Collaboration and

with RIKEN funding are installed in the collider rings (two in each ring, 180° apart). These Snakes make it possible to accelerate, store, and collide (both longitudinally and transversely) polarized proton beams, providing a unique opportunity to carry out the spin physics program at an ultra-high center of mass energies. Other hardware that is built for the spin physics program under this Collaboration includes two sets of four spin rotators that are to be installed on both sides of the collision points for PHENIX and STAR detectors, respectively, and polarimeters.

Out of the 6 possible interaction regions at RHIC, currently 4 host an experiment. There are two major, wide-scope experiments (STAR and PHENIX) and two minor, somewhat more specialized ones (PHOBOS and BRAHMS).

The **STAR (Solenoidal Tracker At RHIC)** detector, as the name implies, utilizes a solenoidal geometry with a large cylindrical Time Projection Chamber (4 m both in diameter and length) inside a large solenoidal magnet. The TPC completely surrounds the interaction point, providing a close to 4π coverage for charged particle tracking. With its three-dimensional tracking capability, the TPC can handle thousands of tracks from an event. The $\mathrm{d}E/\mathrm{d}x$ measurements of track segments allow an identification of particles over a significant momentum range of interest. A Silicon Vertex Detector (SVT) that surrounds the beam pipe improves the momentum resolution of the system and facilitates detection of decay vertices of short-lived particles. The Barrel Electromagnetic Calorimeter and the Endcap Electromagnetic Calorimeter add capability for photon and electron detection and for the determination of their energy.

The other major detector, **PHENIX (Pioneering High Energy Nuclear Interaction eXperiment)** is described in detail in Chapter 3.

The **PHOBOS** detector consists of a two-arm magnetic spectrometer as its central detector and a series of ring multiplicity detectors, which surround the beam pipe at various distances from the collision point and provide a close to 4π solid angle coverage. The exclusive use of high-resolution and high-speed silicon micro-strip devices for the detection element makes the spectrometer table-top size and also provide it with a very high data rate capability for detection of charged hadrons and leptons in selected solid angles. The Time-of-Flight screens improve the particle identification capability of the detector.

The **BRAHMS (Broad RAnge Hadron Magnetic Spectrometer)** detector consists of a two-arm magnetic spectrometer: one in the forward direction for measurement of high momentum particles but with a small solid angle; the other on the side of the collision point for the mid-rapidity region. Both arms are movable to variable settings to cover wide ranges of kinematical regions. The

technology used in this detector is more or less conventional in a sense that the design is quite similar to a spectrometer often used in a traditional fixed-target experiment at a high energy accelerator facility. (In fact, BRAHMS inherited most of the detector and its crew from the E802/E866 experiment at the AGS at Brookhaven National Laboratory.) The spectrometers consist of room temperature narrow gap dipole magnets, drift chamber planes, other tracking devices, Cherenkov counters, and Time-of-Flight detectors.

In order to provide universal characterization of heavy ion collisions, all the four detectors have one common detector subsystem, namely a pair of Zero Degree Calorimeters (ZDCs) that are located behind the beam-splitting points outside the DX magnets. The ZDC is a small calorimeter, consisting of layers of tungsten plates and scintillator slabs, and detects neutron multiplicities from the heavy ion collisions, giving one of the collision centrality measures. The ZDC pair at each crossing point is also used as a luminosity monitor in steering the beams to collide. With the later addition of the Shower Max Detector, an $x - y$ hodoscope, the ZDCs have become capable of measuring the beam position with great accuracy. (For a more detailed description of the ZDC, see Chapter 3.)

Because of the extraordinary complexity of the collision events at RHIC, the detectors are equipped to sample and record massive amounts of data at unprecedented rates. A key part of the experimental program is the RHIC Computing Facility (RCF). Raw data from each of the experiments is sent directly to this dedicated computing center over fiber optic lines. The RCF provides disk and robotic tape storage, as well as CPU processing for data analysis, for all of the RHIC experiments. The processing and storage capacity of the facility is provided in a scalable configuration and through a series of annual upgrades it has kept pace with the growing demands of the collider and the experiments.

Chapter 3

The PHENIX Experiment

3.1 Introduction

PHENIX, the Pioneering High Energy Nuclear Interaction eXperiment [8] is one of the two major, multi-purpose experiments at RHIC. It is designed with versatility in mind: it records information from heavy ion and proton collisions via a number of "probes" or types of particles. Its goals are to study the spin structure of nucleons and to investigate nuclear matter under extreme conditions, proving (or disproving) the existence of Quark-Gluon Plasma (QGP) and study its properties. To that end there formed a large international collaboration of physicists, engineers and technicians, consisting of about 550 people, coming from 60+ institutions in 13 countries.

PHENIX, the detector, measures and characterizes several facets of collisions (events) in RHIC. Using a wide variety of probes, sensitive to all timescales, we can describe systematic changes (with respect to colliding particle species, center of mass energy, collision centrality, etc.) in the properties of nuclear matter. Particles which are detected include muon pairs, electron pairs, photons and hadrons. By measuring their energies and momenta with excellent resolution, we gain information on the dynamics of the collision and the time development thereof; thus understanding each probe contributes to our understanding the big picture – what could have really happened in the collisions. It is in fact a fundamental common denominator of all RHIC experiments that no single signal is sufficient to prove or disprove the existence of the QGP; for better

understanding we have to combine independent results from within the same experiment as well as from other experiments.

At high energy density nuclear matter is thought to transform into a state called QGP, in which quarks and gluons (normally confined inside hadrons) are liberated and form a liquid– or gas-like phase. This is what the Universe is thought to have been like just a few μs after the Big Bang. Measuring leptons and photons coming out of this fireball probes directly this phase, as those particles do not participate in the strong interaction and thus can escape the dense medium virtually unperturbed. For the strongly interacting quarks this medium offers significantly more resistance, and so the emerging hadrons provide information mainly on the later hadronization or "breakdown" of the QGP phase.

The other main goal of RHIC, and thus that of PHENIX is to investigate the spin structure of the nucleon. RHIC accelerates proton beams up to 250 GeV. Proton spins in the beam can be aligned to a great extent, achieving up to 50% polarization. By studying the collisions of such proton beams, PHENIX tries to understand how the spins of the protons arise from that of the gluons and the quarks. This is done by measuring prompt photons with high transverse momentum in the Electromagnetic Calorimeter and by observing the parity violating asymmetry for W particle production in their muon– or electron decay channel, using the muon arms or the central spectrometer, respectively.

To carry out its broad physics agenda, the PHENIX detector uses a variety of subsystems, based on a variety of principles. These subsystems can be described as belonging to one of the following three groups: the so-called *global detectors*, the *central spectrometers* and the *forward spectrometers*. Global detectors characterize collisions and measure some global variables (hence the name), including the start time, the position of the vertex and the multiplicity of the interactions. The pair of central spectrometers (or *arms*) consist of a number of subsystems working together to measure the trajectory, momentum, velocity and energy of leptons, photons and hadrons. Both the East and West arms cover a solid angle of about one steradian and are to the side of the interaction point, at mid-rapidity. The forward spectrometers (North and South) detect muons via a Muon Tracker and a Muon Identifier on each side. They surround the beam pipe in a full circle and have a geometric acceptance of about one steradian each.

It is perhaps worth noting some of the unusual features of PHENIX, which set it apart from most of the other high energy physics detectors. Some of these features were conscious design decisions, trade-offs to lower the overall cost or

Figure 3.1: The PHENIX detector in July 2003. Some of the detectors (including the whole East Arm) are (re)moved from their operational positions for maintenance. (photo by Roger Stoutenburgh)

size of the detector. The final design of the detector, however, allows PHENIX to fulfill its goal: to search for rare events at high data rates.

1. PHENIX is by far not a 4π detector, it only covers parts of the total solid angle and does not "hermetically" surround the interaction point, like STAR's TPC does (see Fig. 3.3).

2. PHENIX's Central Magnet is a dipole magnet rather than a solenoid. This means a non-uniform field for the central spectrometers, which makes tracking charged particles more difficult. On the other hand, the pole tips of the Central Magnet double as hadron absorbers for the North and South muon arms, which are behind them.

Figure 3.2: When not partially disassembled for maintenance, PHENIX is extremely difficult to photograph due to the fact the detector practically fills all available space. The walls of the experimental hall are very close to the outside of the detector and there is no single point from which one can get a good look. This picture was taken with an extremely wide angle lens from the railing giving access to the Muon Identifier. (photo by Roger Stoutenburgh)

3. The North and South muon arms have their dedicated magnet coils, which create a radial magnetic field. All magnets are "warm", non-superconducting ones and have a field integral of about 0.8 Tm [9].

4. Due to spatial and financial constraints, PHENIX does not feature a dedicated hadronic calorimeter. Although identification is possible, this makes precisely measuring hadron energies a challenge in PHENIX.

5. PHENIX was designed to have very little material before its Electromagnetic Calorimeter to make the measurement of energy deposit more accurate.

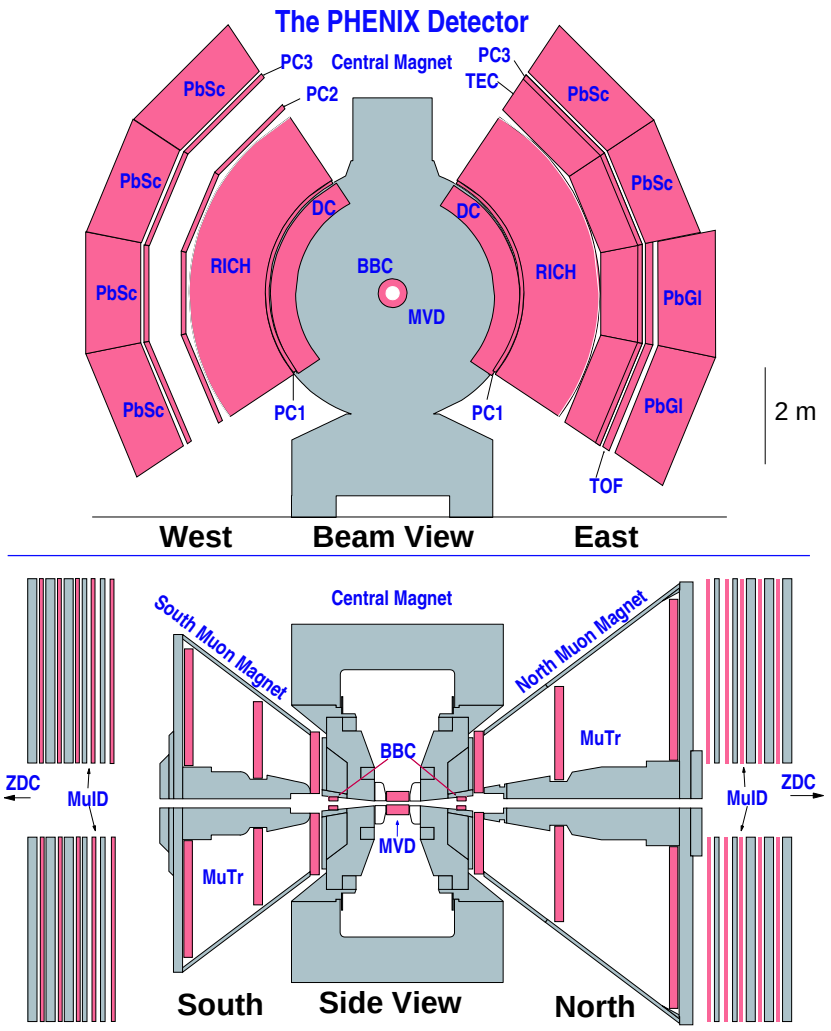

Figure 3.3: Schematic layout of the PHENIX detector in the 2003 RHIC run

3.2 Global detectors

The aim of the global detectors is to supply global information about heavy ion collisions. They consist of a pair of Zero Degree Calorimeters, a pair of Beam-Beam Counters and a Multiplicity-Vertex Detector. Later a Normalization Trigger Counter was also added.

The **Zero Degree Calorimeters (ZDC)** [10] are hadron calorimeters located behind the Y-shaped beam splitting points at $z \approx 18\,\mathrm{m}$ on each side of the interaction regions outside the dipole magnets. The ZDC is used by all four RHIC detectors for triggering and to provide compatible luminosity estimates as well as for measuring the time and location of individual collisions. The splitting beam pipes allow the detector to sit at exactly $\vartheta = 0°$ rather than just at a very low angle. The downside is that this imposes hard spatial constraints on the size of the ZDC; on the other hand, its position makes it ideal for catching neutrons evaporated from beam nuclei due to the collision. Neutrons (or neutral beam fragments) with $\vartheta \leq 4\,\mathrm{mrad}$ fly downstream and, unperturbed by the beam splitting magnets, exit the beam pipe and enter the ZDC. The purpose of the RHIC ZDCs is to detect neutrons emitted within this cone along both beam directions and measure their total energy (multiplicity). The neutron multiplicity is also used to help determine the geometry (centrality) of the collision. The ZDC is a sampling Cherenkov calorimeter, composed of 3 consecutive modules, giving a total thickness of 6 interaction lengths. Each module consists of 27 layers of scintillator interleaved with tungsten plates. Wavelength-shifting fibers carry the light to a photomultiplier tube sitting on top of each module. Later each ZDC was outfitted with a scintillator strip hodoscope called the Shower Maximum Detector. The SMD is located between the first and second ZDC modules. (This location approximately corresponds to hadronic shower maximum depth, hence the name.) Its task is to measure the centroid of the showers in the ZDC and thus to provide valuable feedback to steering the beams.

A pair of **Beam-Beam Counters (BBC)** provide a measure of the Time of Flight (ToF) of forward particles to determine the time of the collision, provide a trigger for the more central collisions and provide a measure of the collision position along the beam axis. The BBC also provides a start signal for the Time of Flight measurements in the central spectrometer, thus its accuracy is crucial for charged hadron identification.

The BBCs are 144 cm away from the center of the detector on either side (North and South) and totally surround the beam pipe. This gives them a pseudorapidity coverage of $3.0 < |\eta| < 3.9$. Each counter is composed of 64 photomultiplier tubes with 3 cm of quartz on the head of the PMT as a Cherenkov

radiator. The Beam-Beam Counters have to function in a very challenging environment: very high particle flux and strong magnetic field. The tightly packed PMTs have to be air-cooled to avoid dangerously high temperatures. Moreover, the BBCs have to function reliably whether only a few particles per event hit the detector (p + p collisions) or a few thousand (Au + Au collisions).

The **Multiplicity-Vertex Detector (MVD)** provides a more precise determination of event position and multiplicity and measures fluctuations of the charged particle distribution. It consists of two concentric barrels of silicon strip detectors ($\approx 70\,\mathrm{cm}$ long, $\approx 64\,\mathrm{cm}$ active) around the beampipe and two endcaps of silicon pad detectors. The two concentric barrels are 5 cm and 7.5 cm from the beam line. For events at $z = 0$, the pseudorapidity coverage of the inner layer is $-2.5 < \eta < 2.5$ and that of the outer layer is $-2.0 < \eta < 2.0$. The disk-shaped endcaps cover the range $1.79 < |\eta| < 2.64$.

The **Normalization Trigger Counters (NTC)**, whose aim is to extend the capabilities of the BBC at low particle multiplicites, are placed between the MVD endcaps and the central magnet's brass nosecones for p + p and p + A running. The two identical counters cover the radial area between the beam pipe and the outer ring of the MVD on each side of the interaction point. The counters consist of plastic scintillating material, read out by wavelength-shifting fibers, which are embedded in the surface of the scintillator. Light from the fibers are coupled into Hamamatsu photomultiplier tubes.

3.3 Central Spectrometers

The central arm spectrometers are placed on either side of the beam pipe and consist of a number of subsystems for charged particle tracking, particle identification and electromagnetic calorimetry. Both spectrometer arms (East and West) have 90° azimuthal and ± 0.35 units of pseudorapidity coverage (or $\approx 44°$ in polar angle), although some of the detectors have smaller acceptance. The main parameters of the subdetectors are shown in Table 3.1.

The cylindrically shaped **Drift Chambers (DC)** [11] are located in the region from 2 m to 2.4 m from the center of the beam pipe (z axis) and are therefore in a residual magnetic field of the central magnet. The multiwire focusing drift chambers provide high resolution p_{T} measurements needed for determination of the invariant mass of particle pairs. The DC also participates in the pattern recognition at high particle track densities by providing position information that is used to link tracks through the various PHENIX detector subsystems.

Table 3.1: Main parameters of the PHENIX subsystems

Element	Granularity	$\Delta\eta$	$\Delta\varphi$	Purpose and special features
Magnets				
Central Magnet (CM)		± 0.35	360°	Up to 1.15 Tm
Muon Magnet South (MMS)		$-(1.1-2.2)$	360°	0.72 Tm for $\eta = 2$
Muon Magnet North (MMN)		$+(1.1-2.4)$	360°	0.72 Tm for $\eta = 2$
Global detectors				
Beam-Beam Counter (BBC)	2×64	$\pm(3.1-3.9)$	360°	Start timing, fast vertex
Multiplicity-Vertex Detector (MVD)	20,736	± 2.6	360°	$\mathrm{d}^2N/\mathrm{d}\eta\mathrm{d}\varphi$, precise vertex, reaction plane determination
Normalization Trigger Counter (NTC)	2×4	$\pm(1-2)$	320°	Extend coverage of BBC for p + p and p + A
Zero Degree Calorimeter (ZDC)	2×3	± 2 mrad	360°	Minimum bias trigger, collision point, collision time
+ Shower Max Detector (SMD)	2×56	± 2 mrad	360°	part of the ZDC
Central Arm Tracking				
Drift Chambers (DC)	$2 \times 6,400$	± 0.35	$2 \times 90^\circ$	Good momentum and mass resolution $\Delta m/m = 1.0\%$ at $m = 1.0$ GeV
Pad Chambers (PC) West	103,680	± 0.35	$2 \times 90^\circ$	Pattern recognition, tracking
East	69,120			for nonbend direction
Time Expansion Chamber (TEC)	20,480	± 0.35	90°	Pattern recognition, $\mathrm{d}E/\mathrm{d}x$ Good momentum resolution for $p_\mathrm{T} > 4\,\mathrm{GeV}/c$
Central Arm Particle Identification				
Ring Imaging Cherenkov (RICH)	$2 \times 2,560$	± 0.35	$2 \times 90^\circ$	Electron identification
Time Of Flight (TOF)	960	± 0.35	45°	Good hadron identification, $\sigma < 100$ ps
Central Arm Calorimeter				
Lead–Scintillator (PbSc) West	10,368	± 0.35	$90^\circ + 45^\circ$	For both calorimeters, photon and electron
East	5,184			detection and energy measurement
Lead–Glass (PbGl)	9,216	± 0.35	45°	Good $\mathrm{e}^\pm/\pi^\pm$ separation at $p > 1\,\mathrm{GeV}/c$ by EM shower and $p < 0.35\,\mathrm{GeV}/c$ by ToF $\mathrm{K}^\pm/\pi^\pm$ separation up to $1\,\mathrm{GeV}/c$ by ToF
Muon Arms				
Muon Tracker South (MuTrS)	21,984	$-(1.15-2.25)$	360°	Tracking for muons
Muon Tracker North (MuTrN)	21,984	$+(1.15-2.25)$	360°	Muon Tracker North installed for 2003 run
Muon Identifier South (MuIdS)	3,170	$-(1.15-2.25)$	360°	Steel tubes and Iarocci tubes
Muon Identifier North (MuIdN)	3,170	$+(1.15-2.25)$	360°	for muon/hadron separation

The task of the PHENIX **Pad Chambers (PC)** task is to provide precise three-dimensional space points for pattern recognition. They consist of three layers in the West Arm and two in the East Arm. Each layer is a multiwire proportional chamber and consists of a single plane of anode wires, bounded by two cathode planes. One cathode is finely segmented into an array of pixels. When a charged particle starts an avalanche on an anode wire, it induces charge on a number of pixels, which is read out through specially designed readout electronics. Pad Chamber layers are numbered from the inside out. PC1 is located right behind the Drift Chamber; PC2 (missing in the East Arm) comes after the RICH; and PC3 is the last detector in front of the calorimeter. All PC layers are outside of the magnetic field and thus tracks through the Pad Chamber layers are straight lines. The information provided by the Pad Chambers is essential in particle identification in RICH and the EMCal. The fact that PHENIX does not have 4π acceptance makes this task even more important, as there are tracks (from secondary– or low-momentum particles) originating outside the DC and PC1 aperture, but hitting one of the outer detectors.

The **Time Expansion Chamber (TEC)** – located behind the RICH detector and before PC3 ($4.23\,\mathrm{m} < r < 4.88\,\mathrm{m}$) – covers the entire East Arm acceptance. It is composed of 24 large multiwire tracking chambers arranged in 4 sectors. Six chambers are stacked to form a sector, each of which covers 22.5° in azimuth and ± 0.35 in η. The TEC in this configuration measures all charged particles passing through its active area. The TEC's tracks are combined with those from the DC and the PCs to solve the complex pattern recognition problems that arise at high particle multiplicities. The TEC is useful for rejecting background for the EMCal, and, by measuring ionization energy losses of charged particles, also helps identifying particles.

Both the East and West Central Arms contain a **Ring Imaging Cherenkov (RICH)** detector system, which provide e/π separation up to the π Cherenkov limit, about $4.65\,\mathrm{GeV}/c$ in CO_2. The RICH detector can be found between the DC and PC2 in the West Arm and between the DC and the TEC in the East Arm. The RICH detectors in both arms are identical and each uses two intersecting spherical mirrors to reflect Cherenkov light onto the array of 1280 outward-looking photomultiplier tubes on both sides of the RICH entrance window. RICH was designed to operate with ethane or CO_2 radiator gas. In the first few years CO_2 was used despite in its lower photon yield, which results in poorer electron-pion separation. Carbon-dioxide, however, has a higher-than-ethane Cherenkov threshold for pions ($4.65\,\mathrm{GeV}/c$ versus $3.71\,\mathrm{GeV}/c$), is more suitable at low multiplicities and is non-flammable, so a decision was made to keep CO_2 as the radiator. It is worth noting that there are several subsystems

behind the RICH detector, so the amount of material within RICH has to be as low as possible. The total thickness of the RICH system is indeed only $\approx 4\%$ of the total radiation length.

The **Time Of Flight (TOF)** detector is placed at a distance 5.1 m from the collision point in the lower half of the East Arm. Its aim is to precisely measure the time of flight for charged hadrons (the momentum of which is already known from the tracking detectors), and thus help identify particles. Its resolution is ≈ 100 ps, sufficient to provide π/K separation up to 2.4 GeV/c and K/p separation up to 4 GeV/c. It consists of 960 plastic scintillator elements (slats) read out by 1920 PMTs, and each slat provides time and longitudinal position information. The high segmentation of TOF was necessary to keep the occupancy low.

The final stage of the central spectrometer arms, the **Electromagnetic Calorimeter (EMCal)** is described in more detail in Chapter 4.

3.4 Muon Arms

The Central Magnet nosecones double as hadron absorbers for the two forward muon spectrometer arms (North and South). The Muon Arms [13] give PHENIX acceptance for J/Ψ decaying into a muon pair at forward rapidities. Each Muon Arm consists of a Muon Tracker inside a radial magnetic field and a Muon Identifier, both with full azimuthal acceptance. The Muon Arms provide on the order of 10^{-3} rejection for pions and kaons.

The **Muon Trackers (MuTr)** consist of three stations of cathode-strip readout tracking chambers. The tracking chambers have multiple cathode strip orientations and readout planes in each station and reside inside a conical-shape "lampshade", in a radial magnetic field. The mass resolution of the Muon Trackers is $\approx \sigma(M)/M = 6\%/\sqrt{M}$ and the spatial resolution is about 100 μm.

The **Muon Identifiers (MuId)** are used to provide more identification for energetic particles escaping the Muon Trackers. It utilizes steel absorbers to efficiently reject hadrons and planar drift tubes operated in proportional mode, called Iarocci tubes. There are 4 layers of absorbers in the MuId, in order 10 cm, 10 cm, 20 cm and 20 cm thick (starting from the front of the detector). The 30 cm (20 cm for the South side) thick steel backplate of the Muon Tracker in front of the MuId provides additional absorbing power. The nosecone of the Central Magnet, the steel in the MuTr and the 60 cm of steel in the MuId reduces the punch-through probability of pions with energy less than 4 GeV/c to about 3%. The 5 gaps created by the absorber steel plates are instrumented

with the Iarocci tubes to provide low-resolution tracking for muons and the surviving hadrons.

3.5 Electronics and Computing

PHENIX selects and archives events of potential physics interest at the maximum rate consistent with the available RHIC luminosity. In order to obtain this high data-collection efficiency, a high degree of coordination between the electronics and computing efforts is required. Custom Front-End Electronics (FEE) were designed for the PHENIX subsystems. Signals from the FEEs are transported by optical fibers to the level-1 trigger that processes signals from a number of subsystems and then either accepts or rejects the event. The trigger operates in a synchronous pipelined mode with a latency of 40 beam crossings, and thus generates a decision for each crossing. The timing of the above operations is coordinated by a master timing system that distributes the RHIC clocks to granule timing modules that communicate with the FEEs.

In order to study the rare event physics for which PHENIX was designed, it is necessary to have a higher level of event rejection than possible with the level-1 trigger alone. Therefore a level-2 software trigger – that makes its selection after a complete event is assembled – was developed.

Once the level-1 trigger accepts an event, the data from the various subsystems is routed via fiber-optic cable to the data collection modules, that interact with the subsystems by means of daughter cards, that format and zero-suppress the data. Data packets are generated by digital signal processors and sent to event builders, that assemble the events in their final form. The control and monitoring of the electronics and triggering is handled by the Online Computing System (ONCS). ONCS configures and initializes the online system, monitors and controls the data flow and interlocks the data acquisition process with the slow controls systems. After the data is collected, the offline system provides event reconstruction, data analysis and information management. It provides the tools to convert raw data into physics results.

Chapter 4

The Electromagnetic Calorimeter in PHENIX

4.1 Hardware

The EMCal [14], [15] consists of two different detector subsystems, with one quarter of the central arm acceptance covered by 9216 lead-glass (PbGl) Cherenkov modules and the other three quarters of the acceptance covered by 15552 lead-scintillator (PbSc) sampling calorimeter modules.

The calorimeter is located at a radial distance of $\approx 5.4\,\mathrm{m}$ from the beam axis in order to maintain an acceptable occupancy in the high particle multiplicity environment of central ("head-on") Au + Au collisions. It covers the range between -0.35 and 0.35 in pseudo-rapidity and $2 \times 90^\circ$ in azimuth.

The calorimeter measures position, energy and time of flight of the incoming particles. The energy information is very accurate for electrons and photons, but not for hadrons – most hadrons in the energy range typical to RHIC only deposit part of their energy in the EMCal.

Both parts of the calorimeter are equipped with their respective reference systems, the principles of which are very similar, but their implementations differ. The reference system of the calorimeter provides online quality control and calibration capabilities.

4.1.1 PbSc

Structure

The PbSc part of the calorimeter is a sampling calorimeter. It consists of 6 sectors, each about 4 m × 2 m in size, at a distance of 5.1 m from the z axis. The sectors consist of 72 × 36 towers, which have a sandwich-like structure (Fig. 4.1). Each "sandwich" has 66 layers, where the layers consist of 1.5 mm of Pb absorber plus 4 mm scintillating material (1.5% PTP/0.01%POPOP). The cross-section of towers is $5.54 \times 5.54\,\mathrm{cm}^2$.

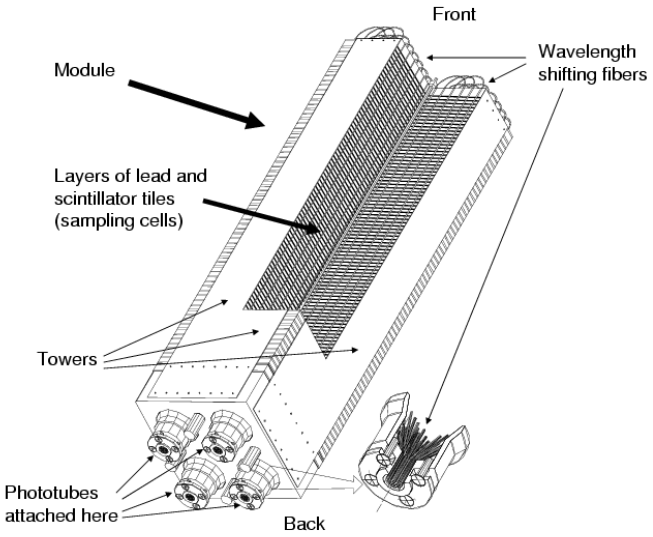

Figure 4.1: Schematic layout of a quad-tower module in the PHENIX PbSc calorimeter.

Incoming electromagnetically interacting particles generate electromagnetic showers in the lead absorber and the showers in turn generate flashes in the scintillating material.

Towers have 36 holes bored into them (in a 6 × 6 configuration), which go through all layers. Penetrating wavelength-shifting fibers weave through these

holes and carry the scintillator's light to the phototubes mounted at the back end of the tower. Note that there are 36 holes, but only 18 fibers: fiber ends on the front face of the tower are looped back through another hole. This arrangement ensures that light ends up at the phototubes at the back end of the calorimeter, regardless of its initial direction in the fiber. It also helps decrease the longitudinal non-uniformity of the energy response.

Reference system

Fig. 4.2 shows the basic layout of the PbSc reference system. A Nd:YAG laser fires in anti-coincidence with physics events. (The laser's base frequency is tripled to move its light from the IR region to UV, $\lambda = 355\,\mathrm{nm}$). Its light is split multiple times and carried to the calorimeter by delivery fibers. In the final stage, every four towers share a special fiber which goes through all layers in the middle of a quad-tower module. This fiber is special in that it has a non-uniform spiral etched into its outer surface; this results in light leaking from the fiber into the calorimeter. The spiral was etched in such a way that the depth distribution of the leaked light imitates the shower depth profile of a 1 GeV electromagnetic shower.

To eliminate the error from the varying intensity and the uneven distribution of the laser light, PIN diodes were installed at several places in the system to provide normalization.

4.1.2 PbGl

Structure

The PbGl part of the calorimeter is based on the Cherenkov principle. It consists of 2 sectors, which are the same size as the PbSc sectors. The PbGl, however, has finer granularity: sectors consists of 96×48 towers, which are consequently smaller than those in PbSc: $4 \times 4\,\mathrm{cm}^2$. The front face of the PbGl sectors is at a distance of 5.4 m from the z axis.

Charged particles hitting the calorimeter that are faster than the speed of light in the medium ($n = 1.648$) produce Cherenkov light. The Cherenkov photons propagate with a wavelength-dependent attenuation through the (homogeneous) PbGl to the photomultipliers at the back end of the towers.

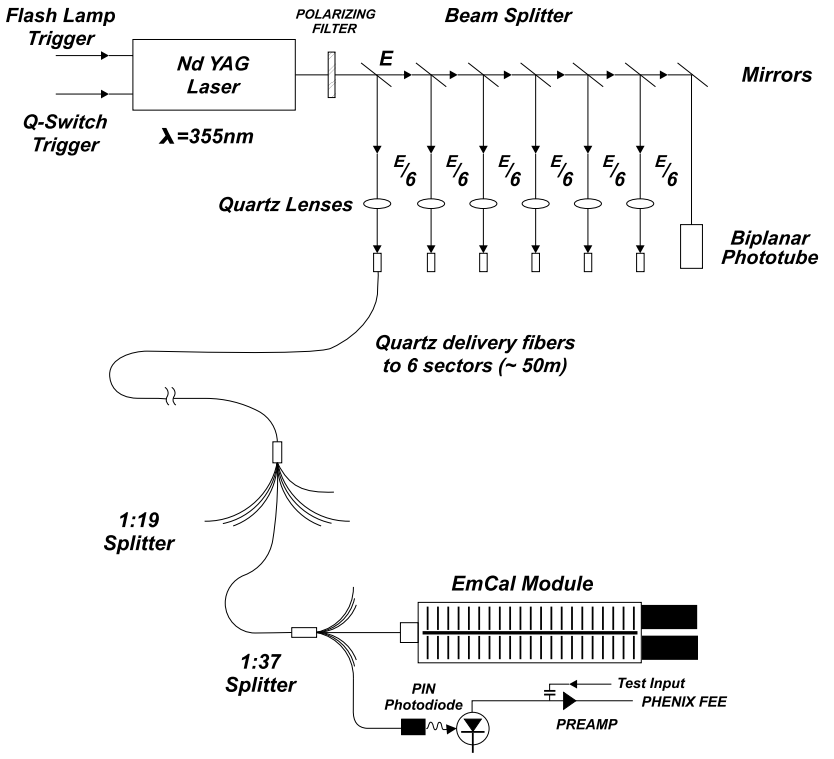

Figure 4.2: The reference system of the PbSc calorimeter.

Reference system

The reference system of the PbGl calorimeter works along the same lines as that of the PbSc: we inject light into the towers and the light propagates through the calorimeter to the phototubes at the back end. The signal of the photomultiplier is then treated similarly as in real, "physics" data, i.e. digitized and recorded in the normal data stream. Unlike the PbSc, each PbGl supermodule (6×4 array of towers, see Fig. 4.3) has its own reference system. This consists of an LED board on the front face of the supermodule, a reflective cover ("dome") over it and a photodiode. When one of the LEDs are fired, the dome reflects its

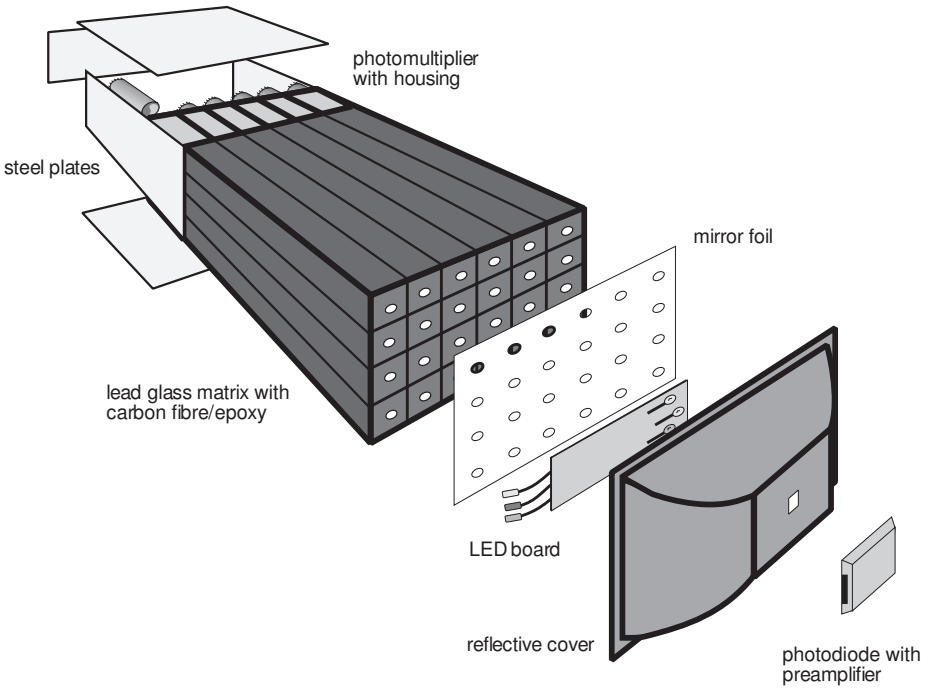

Figure 4.3: Exploded view of a PbGl supermodule.

light back to the towers, which carry the light to their respective phototubes. To eliminate uncertainty which comes from the fact that the emitted light intensity is not the same in every pulse, the light is also observed by a photodiode on top of the dome, and its signal is used for normalization.

4.2 Monitoring

The optical monitoring system is designed to track shifts in the gain as well as in the timing response of the individual towers of the calorimeter. Inbetween "physics" events, the monitoring system (the details of which were discussed earlier) injects light into the calorimeter and the light is transferred to the pho-

tomultipliers. The signal of the photomultipliers is then digitized, their data are recorded in the normal data stream and are readily available for online quality control and (offline) calibration. Gain tracing with the optical monitoring system ensures the stability (less than 1% variation) of EMCal gains over an extended period, which is crucial when analyzing rare processes. (As a matter of fact, when dealing with steep (exponential or power-law) spectra, even a 1% error on the energy scale alone can easily cause systematic errors on the order of tens of percents.)

4.3 Calibration

4.3.1 Calibration principles

The energy– and timing response of the EMCal have to be calibrated and the "dead" and "hot" towers need to be found before doing any analysis based on the calorimeter. We use a number of methods, which complement each other and provide valuable cross-checks. Our calibrations include:

- test beam data from the construction phase
- calibration inherited from WA98 (the original owners of our PbGl detector)
- calibrations based on the reference system (both PbSc and PbGl, energy and timing)
- calibrations based on physics data

Here I will discuss the principles of some of calibration methods based on physics data; more details on how the calibration was carried out in RHIC Runs 2 and 3 will follow in 4.3.2.

Dead and hot towers

Finding dead and hot towers can be done in several different ways – the main idea, however, stays more or less the same. The recipe is the following: take a sufficiently large data sample; count how many hits the individual towers registered in the sample; plot this hit frequency distribution; tag towers that are too far off the average number of hits as either dead or hot, depending on which side of the average they are on. You can tune the strictness of your cut

depending on how large fraction of the calorimeter you can afford to lose in your particular analysis.

Experience shows, however, that this simple method is not good enough. There are towers which do not fire very frequently, and thus not considered hot by the previous method; but when they *do* fire, they consistently fire with a relatively high (very improbable) energy. Therefore, the aforementioned "hit frequency method" has to be applied separately in different energy ranges, which means that the amount of statistics needed dramatically increases.

Physics-based energy calibration methods

Since the EMCal is not a hadron calorimeter, the hadrons created in the high-energy collisions of RHIC usually don't stop in the detector, they go through it as Minimum Ionizing Particles (MIPs). The typical energy deposited by hadrons is almost independent of their total energy, but is characteristic to the material they traverse. This typical energy is known to be $\approx$ 270 MeV for the PbSc and $\approx$ 350 MeV for the PbGl. These values give a stable point of reference on the energy scale. (Since the depth of the EMCal is about 1 nuclear interaction length, hadronic showers also start to develop, but this energy deposit is typically small.)

We can also exploit the fact that, due to their low mass, electrons and positrons are practically always relativistic in high energy physics. This means that their energy E and momentum p, measured in GeV and GeV/c, resp., are equal: $E = p$. We can use the Ring Imaging Cherenkov counter (RICH) of PHENIX to identify electrons, and our tracking detectors measure their momentum. Then they are stopped by the EMCal, so their energy is also measured. Therefore, we can plot the distribution of E/p for electrons, and fit the prominent peak. If it is not at 1, the peak position gives us a correction factor for the energy scale.

The difficulty of the electron method is that to collect enough electrons in each individual tower, a tremendous amount of statistics is needed, and electrons are quite rare.

Neutral pions decay to two photons with a lifetime of $\approx 10^{-16}$ s. This makes the π^0 yield measurement an ideal analysis to do with the EMCal, since the main focus of this detector is detecting and measuring electromagnetic particles. (Note that from the point of view of the calorimeter, the π^0 is not a hadron! It decays long before leaving the vertex, so the π^0 analyses are practically photon correlation measurements.) Additionally, neutral pions also provide a way to check the energy scale. If we plot the invariant mass of photon pairs suspected to

come from the same π^0 (see Fig. 4.4, middle panel), the distribution should peak at 135 MeV, the mass of the π^0. This is not the case in nucleus-nucleus collisions: due to the high number of particles, showers in the calorimeter often overlap, and this effect systematically distorts the mass distribution. RHIC, however, also collides (polarized) proton beams, and the low-multiplicity, clean environment of collisions allowed us to also use neutral pions for energy calibration.

This method is also quite statistics-intensive, but less so than the electron calibration. The reason for that is that the largest producer of electrons is the Dalitz decay of neutral pions ($\pi^0 \to e^+ + e^- + \gamma$), which has a branching ratio of 1.2%, thus calibrating with electrons requires more than 80 times more data for the same number of particles.

Physics-based timing calibration methods

Photons travel with c, so they are the fastest particles possible. RHIC tells us the exact moment when a collision occurs – after that, we look at the energy deposit vs time in the calorimeter. Even when hundreds or thousands of particles are created in a collision, the first to arrive must be the photons, all the hadrons lag behind – so we look for the first, large peak.

Since we are free to choose the starting point of the time measurements, in the photon and π^0 analyses we choose 0 to be the instant when a photon created early in the collision reaches the front face of the calorimeter. Since in the raw data 0 is chosen quite arbitrarily, we have to shift all the measured times to conform with this convention. So, the procedure is more or less the following: we collect a large (uncalibrated) data set; we select photons with a few well-placed cuts; check where the photon peak lies in the individual towers; and apply offsets to move them to 0.

Since the timing response of the towers varies, shifting them by offsets to a common point is essential to get a good timing resolution. (In 62.4 GeV Au+Au collisions we have achieved $\sigma \approx 300$ ps.)

The (squared) mass distribution of hadrons can be measured by measuring their momentum, time of arrival and path length. If the time scale we use is wrong, the particle masses also come out wrong and have to be shifted back to their proper position. This also gives a correction to the underlying time measurement.

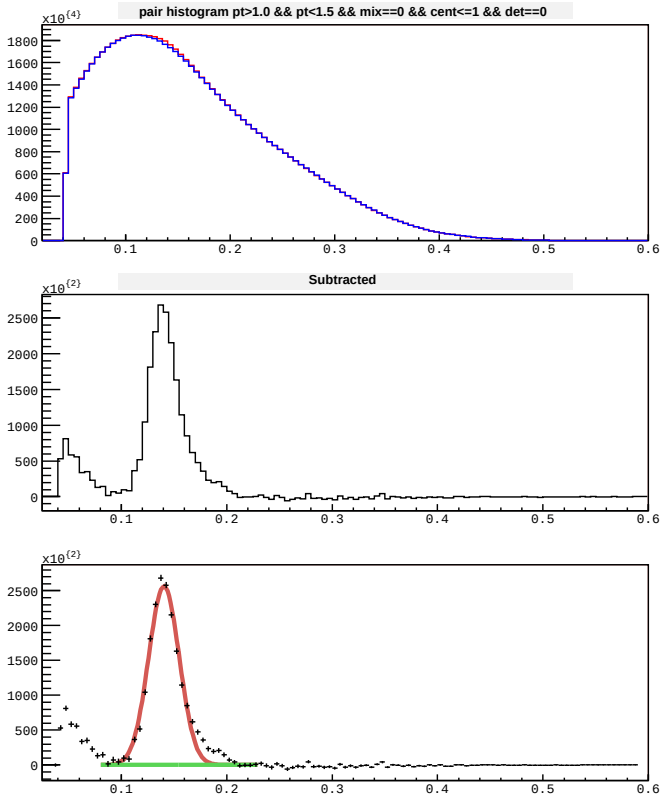

Figure 4.4: Top panel: Invariant mass distribution of photon pairs in $\sqrt{s_{NN}} = 62.4\,\mathrm{GeV}$ central $\mathrm{Au} + \mathrm{Au}$ collisions. Middle panel: The same invariant mass distribution, with the background subtracted. Bottom panel: π^0 peak fitted with a Gaussian.

4.3.2 Calibration details

In this section I will describe the actual calibration work done by myself and others in preparation for our analysis on neutral pions done for Quark Matter 2002 conference. We had to ensure several things, namely that the conversion from the detector's raw data (ADC counts and TDC counts) to energy and time information is done correctly; that signals from the two large detectors (PbSc and PbGl) are consistent and are stable in time; that the effect of "hot" and "dead" towers are taken into account; that we have a way of assessing the quality of a particular set of data from a detector; and finally that the software framework applying all the calibrations and corrections does what it should.

The basic idea behind the calibration process in RHIC Run 2 was that we tried to get the essential parameters about right from the start and we started applying corrections once we had more statistics and more information available. This approach was helped by the fact that we already had good estimates on the basic parameters from test beam data, from the previous year's running and – in the case of the PbGl – from data taken at the WA98 experiment at CERN. A major advantage of this method was that by making small corrections late during data reconstruction we did not have to reprocess raw data files over and over again. Doing that would have been a tremendously computing-intensive task, taking weeks or even months even on the high-performance computer farm of the experiment.

Gains

Raw data files contain very basic information coming from the detector. The analog signal – which is proportional to the energy deposited by a particle in an individual tower – is digitized by the electronics on the detector itself and we record these *ADC counts* in the data files. To get physically meaningful *energies*, the ADC counts have to be multiplied by empirically determined gain factors. This is done during the (offline) reconstruction. Gains vary in time due to changing operating conditions and the variation is constantly monitored by the monitoring system described earlier. This process is also called *gain tracing*.

Raw data files contain the output of the monitoring system, so they can be used to analyze gain variations. Fig. 4.5 shows the time evolution of gains. Each dot on the 2-D histograms represent one channel (tower) of the calorimeter, and all gains are normalized with their initial values. It is clear from the graphs that gains tend to change in time and some of the drift is uncorrelated, i.e. towers at different places in the calorimeter may drift in opposite directions.

But there are correlated jumps as well, the biggest one happening during the shutdown halfway through the data-taking period. In RHIC Run 2, the last of the PbSc sectors, W3[1] was not yet fully operational – before the shutdown it had 10 working supermodules out of 18, and during the shutdown 4 more were instrumented, raising the total to 14 out of 18. The maintenance, however, affected the other sectors as well.

Due to lack of confidence in the correct operation of the gain tracing system and limited statistics to better understand it, we have decided *not* to use these results for corrections in the analyses to be presented at Quark Matter 2002. We have only used two gain sets for the whole RHIC run, one which is valid from the beginning of the run to the shutdown and an other which is valid from the shutdown to the end of the run. We fine-tuned the energy calibration using 'physics' events instead, namely by looking at the Minimum Ionizing Particle (MIP) peak at the Quality Assurance (QA) stage (see 4.3.2). Setting the gains constant was favored over the default gain tracing because we found that that way the width of the π^0 peak got *narrower*. The gain tracing system is naturally expected to make energy measurements more accurate and thus peak widths smaller rather than larger, so we decided not to use it for the QM2002 analyses.

Timing

In addition to the energy of the incoming particles, their time of arrival is also measured. The origin of the time scale is chosen to be the instant when photons coming from the interaction vertex hit the front face of the calorimeter. In reality, the arrival time of photons has an offset, which has to be corrected.

Initial calibration of the timing system was also carried out using the monitoring system, with varied laser delays and amplitudes. There are, however, major differences between "laser events" and "physics events" from the calorimeter's point of view. One such difference is that in laser events, the electromagnetic shower shape and the penetration depth does not depend much on the laser amplitude, whereas it does depend on the energy of the particle in physics events. Another difference is that in physics events only a fraction of the towers fire (detector occupancy is low), whereas in laser events all towers fire, so a cross-talk between channels can distort the response of the detector. For these reasons it was understood that the initial calibration was indeed just that, a first approximation, and we will have to use physics events to tune the timing

[1] I denote the sectors of the calorimeter by a letter and a number showing their position in the detector. W is for West Arm, E is for East Arm. Sectors on both sides are numbered 0 through 3, 0 being the lowermost sector in both arms. The PbGl sectors are E0 and E1.

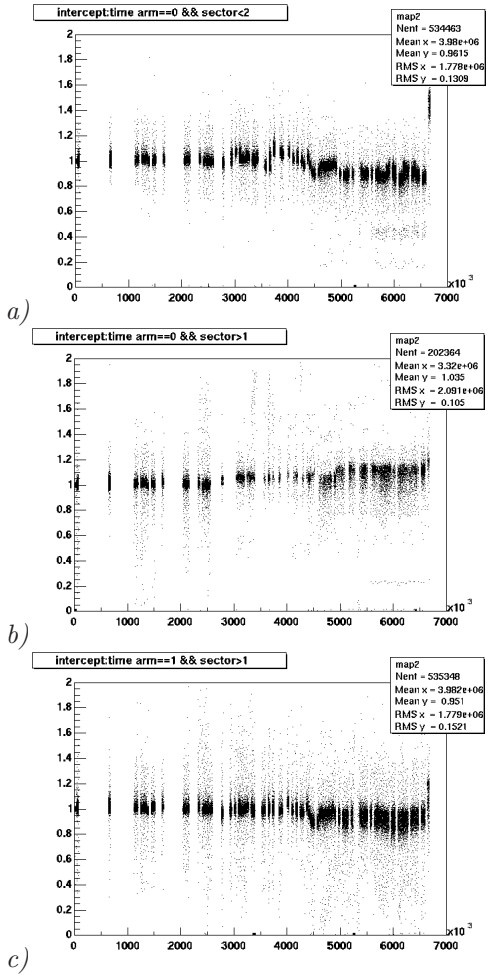

Figure 4.5: Time variation of gains in the 3 PbSc granules. *a)* Sectors W0 and W1; *b)* sectors W2 and W3; *c)* sectors E2 and E3. The horizontal axis shows time measured in seconds; gains are normalized to the gain in the first bin.

performance of the calorimeter. The calibration based on physics data was done in two stages:

- global (i.e. time-independent) tower-by-tower corrections compensate the differences in the response time of individual channels (9216 in the PbGl part of EMCal, 15552 in PbSc, although some towers are not instrumented) thus reducing the width of the photon timing peak;

- sector-wide run-by-run corrections (8 numbers per detector run, see below), which move the photon peak to 0 and follow variations in time.

Tower-by-tower corrections were produced from a large, relatively clean sample of photon-like showers. The amount of statistics required was such that each tower have enough hits (on the order of 10^4) that a Gaussian can be fitted to their distribution. The position of the peak on the time axis relative to 0 gives the calibration constant for that tower. These offsets were determined separately for the pre–Oct 11 and the post–Oct 11 periods. The reason for this division was that many calibration changes occurred during the shutdown around Oct 11 2001, which were clearly observable as a "jump" in the uncalibrated data, discovered by the QA code.

Run-by-run corrections were established using a subset of data from each detector run. A detector run is an interval of data-taking (ranging from a few minutes to a couple hours at most) during which the detector operating conditions do not change. If something *does* change, the run is stopped, problems (if any) are fixed and a new run is started. It is thus reasonable to follow variations of detector parameters based on run number rather than time.

Extraction of the run-by-run corrections for the 8 sectors of the calorimeter was done by my Quality Assurance (QA) code (a detailed description will follow in 4.3.2). Only a portion of the data from each run was analyzed, due to limited CPU time and disk space. The QA code selects photon-like showers in the calorimeter, based mainly on the parametrized shape of the showers and their arrival times; it then subtracts the time of the start signal (given by the BBC detector) and plots the time distribution of photons for each sector. The distribution is fitted with a Gaussian, whose parameters are written out into a text file. Ideally, the mean of the Gaussian should be at 0, so the offset gives the (additive) correction itself for that particular run and sector. These corrections were then inserted into the calibration database, and were applied during the reconstruction of the data. Additionally, the width of the distribution is useful for checking the sanity of the check and the resolution of the calorimeter.

All timing calibration was done with photons, as they are the only particles whose speed – and therefore their theoretical time of arrival – we know. Charged hadrons, however, provide a useful cross-check for the quality of timing. We selected hadron-like showers in the calorimeter with a matching track in the Drift Chamber and plotted the distribution of their squared rest masses, m_0^2. Using high energy physics units ($\hbar = c = 1$), $m_0^2 = E^2 - p^2$, where E and p are the total energy and momentum of the particle, respectively. Momentum is measured in the Drift Chamber and, knowing the path length s and the time of arrival t of the particle, the total energy can be calculated:

$$E = \frac{m_0 c^2}{\sqrt{1 - \frac{v^2}{c^2}}} = \frac{m_0 c^2}{\sqrt{1 - \frac{s^2}{t^2 c^2}}} \qquad \text{(in SI units)}, \tag{4.1}$$

$$E = \frac{m_0}{\sqrt{1 - \frac{s^2}{t^2}}} \qquad \text{(in HEP units)}. \tag{4.2}$$

Thus a problem with the timing affects the calculated energy of a hadron, which in turn appears to shift the rest mass of the particle. Indeed, one such problem was encountered in sectors W2 and W3 and was promptly solved.

As a result of all these corrections, the photon peak is generally within 100 ps of 0 and in the PbSc part of the calorimeter has a standard deviation around or lower than 400 ps, as shown in Fig. 4.6. Sector W3 is the worst of the PbSc sectors: it can at times be more than 200 ps off and have a resolution of 550 ps. The resolution of the PbGl sectors is approximately 600 ps. As an example, I plotted the timing peak separately in each sector from a calibrated data file in Fig. 4.7.

An additional improvement over previous year's data is that the photon peak does indeed have Gaussian shape. This is demonstrated in Fig. 4.8, where the fraction of extracted π^0s is plotted versus the width of the ToF cut for different transverse momentum bins.

We also investigated whether the position of the timing peak is dependent on the energy of the particles, and it turned out that it was. The effect was such that particles with more energy appeared to have arrived *later*. Even though simulations predicted a systematic shift with energy, its direction was counter-intuitive, we expect high energy photons to (seemingly) arrive earlier. The reason for this is that high energy photons cause more extended, deeper showers in the calorimeter, thus the scintillation photons in the wavelength-shifting fibers have a shorter path to travel until they reach the phototubes at the back end of the calorimeter. Since the development of the shower happens

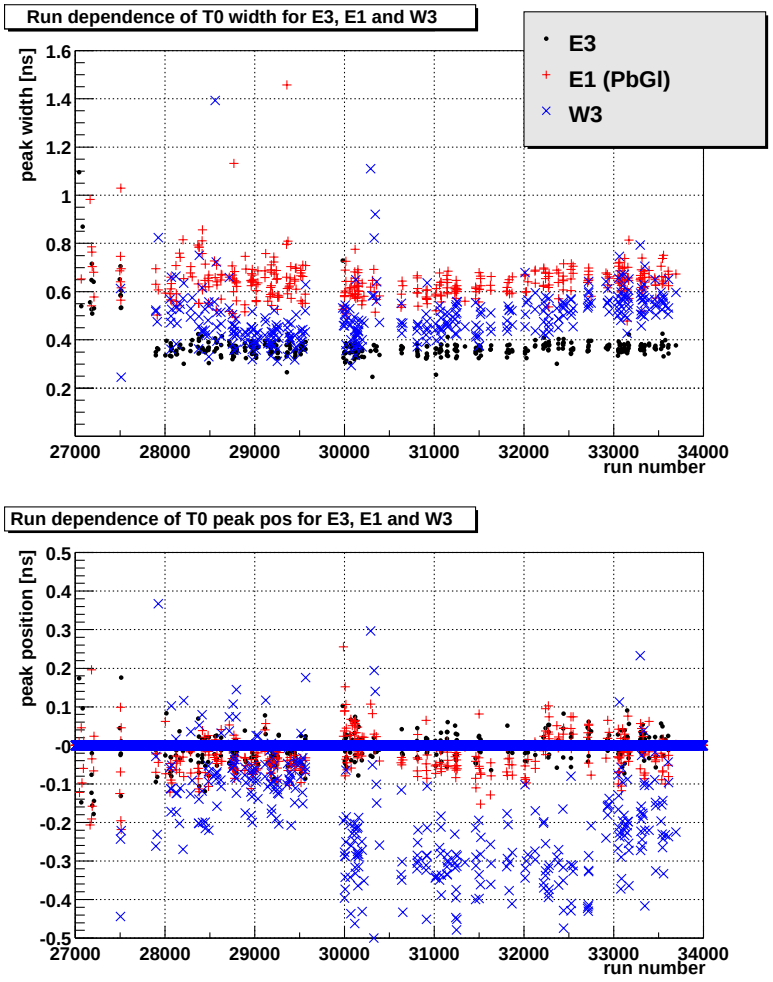

Figure 4.6: Photon peak width and position in the calorimeter after the calibration in the best (E3) and the worst (W3) of the PbSc sectors and in one of the PbGl sectors (E1).

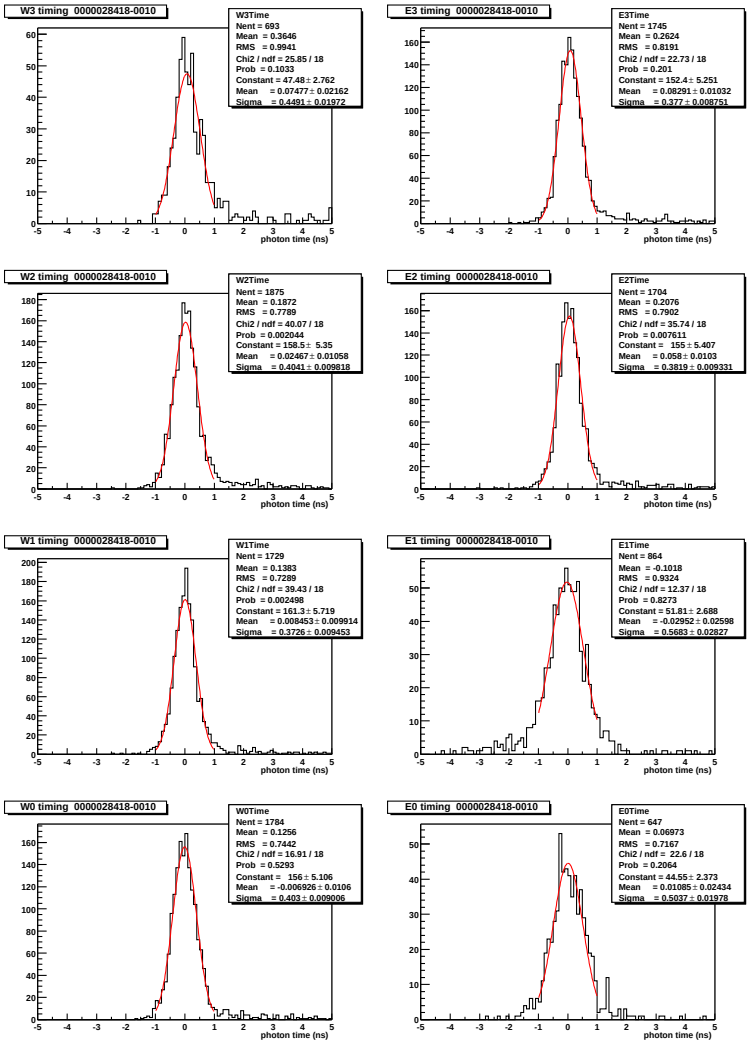

Figure 4.7: The photon peak in the calorimeter in one segment of one detector run.

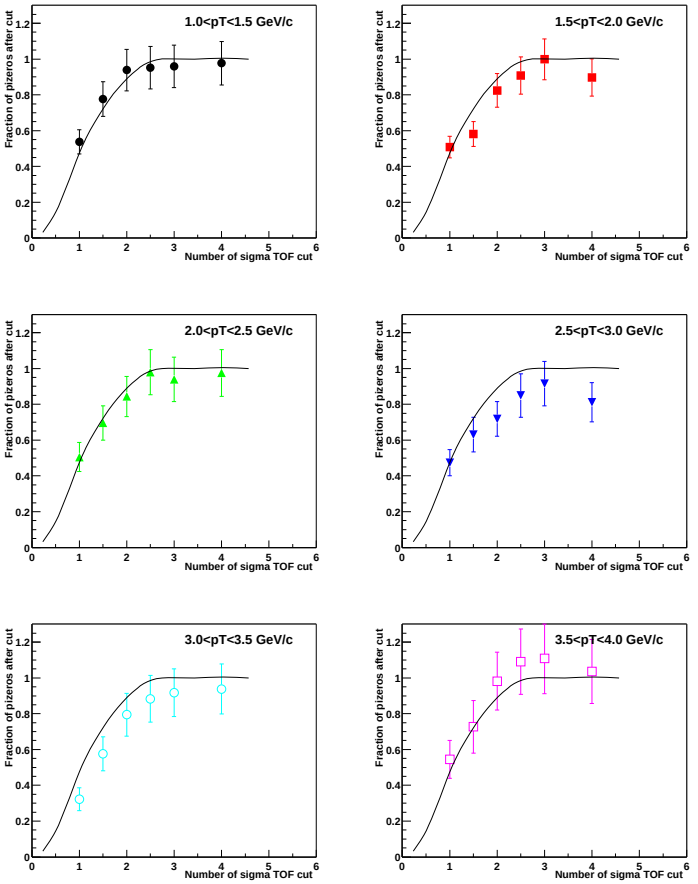

Figure 4.8: Fraction of counts extracted with Time of Flight cut to counts extracted with no Time of Flight cut vs the width of the Time of Flight cut. Points are data, the continuous line is the theoretical value calculated from the Gaussian lineshape only. Data are consistent with the assumption of a Gaussian distribution.

at $\approx c$, whereas the scintillation signals travel only at $c/1.7$ in the fibers, the light from deeper showers will arrive earlier than that from shallower showers.

There are three known possible sources of energy (momentum) dependence of the ToF measurement in EMCal. One major source is the so called slewing effect, i.e. an energy dependent readout of the TDC coming from the fact that the readout is triggered by a certain signal level which is achieved earlier in case of signals of higher amplitudes (their slope is also steeper). Another source, which can cause similar effect, is the variation of depth of EMCal showers. Light signals from deeper showers of higher energy reach the electronics faster then those from shallower ones. A third possible known effect can come from the cross talk of adjacent channels in EMCal timing electronics.

There had been attempts to compensate for these effects in the calibration of the calorimeter before RHIC Run 2 as well, but the limited available statistics had made such work difficult and apparently unreliable. We think that the reason for the shift to the wrong direction were probably due to corrections that overcompensated the slewing effect. With more statistics available from RHIC Run 2, we did a study of the energy dependence, without trying to explain its cause. For the study we selected a relatively clean sample of photons, requiring that the time of flight be within 3 ns of the ideal 0; that there should be no track in the Drift Chamber corresponding to the hit in the calorimeter; and the shower shape be sufficiently photon-like. We collected data separately for both parts of the calorimeter. We noted that this unexplained effect can result in an efficiency loss in any analysis that applies a cut on the EMCal ToF and does not take into account its energy dependence. As our studies have shown, photons and charged particles are affected similarly. The photon timing peak position and width were calculated at various energy ranges. The results are shown in Fig. 4.9 and in Table 4.1.

Energy

Energy calibration was based on hadrons, punching through the calorimeter, acting as Minimum Ionizing Particles (MIPs). The average energy deposit of MIPs depends on the thickness and the composition of the detector and is well-known: 270 MeV in the PbSc calorimeter and 350 MeV in the PbGl.

The scale factors which convert ADC counts into physically meaningful energies were established using a large quantity of hadrons. The calculation was done for each individual tower. The scale factors were calculated such that

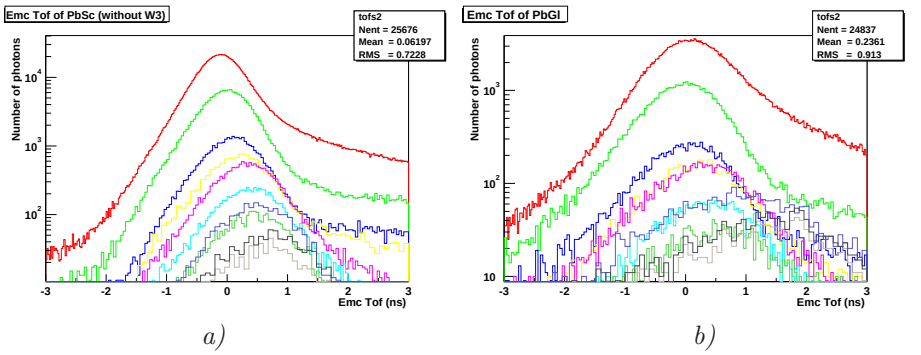

Figure 4.9: EMCal ToF in different energy bins in *a)* PbSc *b)* PbGl. The colors correspond to the energy bins in Table 4.1.

they bring the MIP peak positions of all towers to a common value; towers that did not have a good MIP peak fit were corrected with a scale factor of their respective supermodule. (This method is justified by the observed correlated behavior of towers in the same supermodule.) Just as during the timing calibration, we found severe problems with the uppermost sector in the West Arm of the calorimeter (W3) and we recommended excluding it from every analysis until those problems are better understood, addressed and fixed.

After establishing initial gains for each channel of the detector, the gain tracing system was supposed to monitor (and compensate for) the changes in the output of the calorimeter. While testing the calibrations by looking at MIP peak positions and E/p ratios for electrons, however, an energy scale mismatch was revealed between different sectors and along three intervals of RHIC Run 2. This mismatch manifested itself in the MIP energies not being aligned in the different sectors with respect to each other and also in having sudden jumps around certain run numbers. This behavior was also observable in the QA output. This was clearly non-physical, so the gain tracing system was turned off, and all calibrations were done with constant, time-independent gains.

Based on the results of QA, the entire RHIC Run 2 was divided into three periods, and it was decided that for each period a separate correction table should be inserted into the database. Within each of these three periods a straight line of slope zero was fit to the run-dependent MIP peak positions. The new corrections arose by multiplying the original tower by tower correction

Table 4.1: Mean photon peak position and its σ as observed in PbSc data and PbGl data as a function of photon energy.

E (GeV)	PbSc mean (ns)	PbSc σ (ns)	PbGl mean (ns)	PbGl σ (ns)
0.5–1.0	−0.107	0.35	0.09	0.62
1.0–1.5	−0.01	0.39	−0.33	0.60
1.5–2.0	0.1	0.43	0.13	0.65
2.0–2.5	0.21	0.48	0.18	0.72
2.5–3.0	0.32	0.50	0.3	0.7
3.0–3.5	0.38	0.52	0.34	0.77
3.5–4.0	0.38	0.54	0.5	0.85
4.0–5.0	0.45	0.54	0.84	1.1
5.0–6.0	0.6	0.6	1.44	0.94
5.0–10.0	0.7	0.6	1.4	1.0

factors with the fit constants, thus creating 3 tables out of 1. As shown in Fig. 4.10*b)* the MIP peak in the middle period is about 2.5% lower in W2 and W3 than in the other sectors. For this reason those energies were multiplied by another factor to bring W2 and W3 in line with the rest of the PbSc.

The green points in Fig. 4.11 indicate that the energy scale has become consistent, and the expected run-by-run energy resolution is several percents.

The energy calibration of the PbGl calorimeter was done independently, but similarly to that of the PbSc calorimeter, and those studies provided us with a way to cross-check both calibrations.

Hot and dead towers

The method for identifying hot towers in the PbSc EmCal sectors which were then added to the cluster warnmaps in the data files was a simple one based on hit frequency. The general method was as follows. First, on a run by run basis, the number of hits above a certain energy threshold were histogrammed for each tower. Second, again on a run by run basis for each of these thresholds, a histogram was made of the number of towers hit, and a Poisson or Gaussian was fit around the mean value. Third, one of the thresholds was chosen for each run, and all towers whose number of hits were above a certain number of standard deviations, defined by the fit function in the second step, were recorded for each run in text files based on the QA EMC extra reject list format. Last, the text files

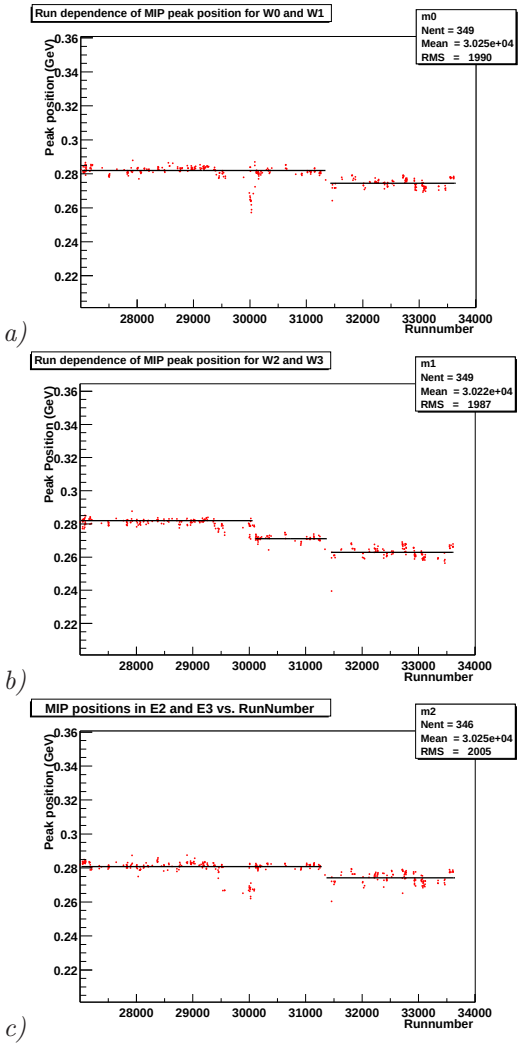

Figure 4.10: Run dependence of MIP peak positions in the 3 PbSc granules. *a)* Sectors W0 and W1; *b)* sectors W2 and W3; *c)* sectors E2 and E3.

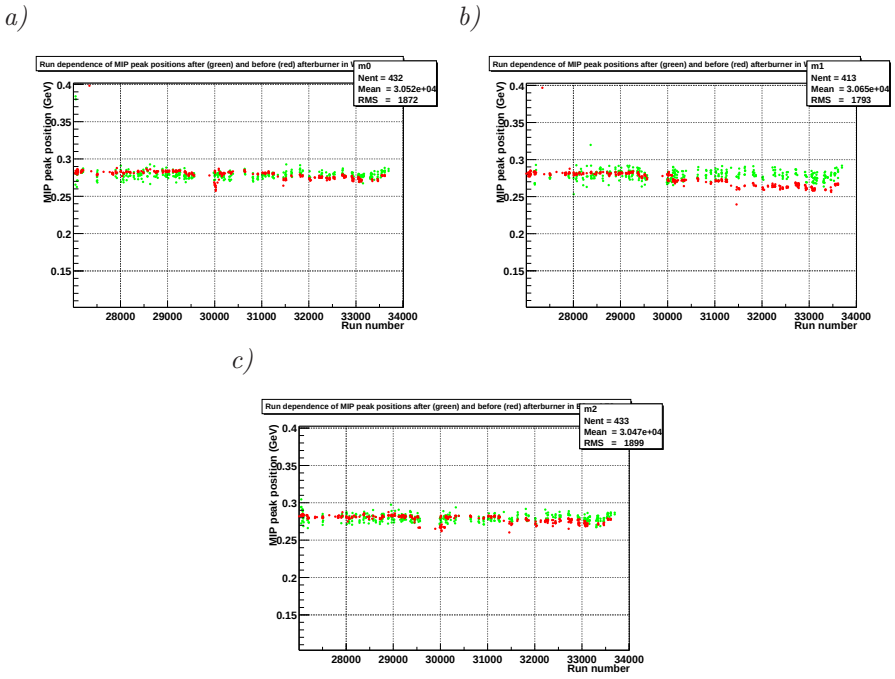

Figure 4.11: Fluctuation of MIP peak positions before (red) and after (green) the recalibration of the energy – as seen by the QA. *a)* Sectors W0 and W1; *b)* sectors W2 and W3; *c)* sectors E2 and E3.

for all processed runs were combined into one large file containing the union of all identified hot towers, and these list were inserted into the calibration database. Since there is a wider scale of tower behaviors than just good and bad, we had to strike a balance between excluding too many or too few towers. Excluding too few towers has the obvious drawback of using potentially misbehaving ones in our analyses, which may lead to artifacts. Excluding many towers reduces the acceptance of the detector even more than mere numbers would suggest: since showers in the calorimeter extend to several towers, any cluster of hit towers identified as one passing particle that has a bad one in it must be discarded.

In the **histogramming phase**, the number of hits above a certain energy threshold were put into a histogram, the bins of which corresponded to one tower in the detector. Four thresholds were studied: 0 GeV (no threshold), 0.5 GeV, 1.0 GeV and 1.5 GeV. Fig. 4.12 shows an example of these histograms for one detector run.

In the **fitting phase**, we made 4 histograms (for the 4 thresholds) of how many times individual towers were hit in each detector run. This distribution has a peak and we fitted it with a Poisson or a Gaussian to get the average number of tower hits for each run. Whether to use the Poisson or the Gaussian results was decided on a run-by-run basis by the χ^2 result of the fit. In most cases, the results of the Gaussian fit were used. An example is shown in Fig. 4.13.

In the **identification phase**, a limit was chosen (based on the result of the fit) as the maximum number of hits a tower could have for the run and not be considered hot. The limit and its definition were studied extensively: limits of 3–12 standard deviations (defined by the fitting functions or the raw RMS), as well as limits based on the statistics in a certain sample were studied and appropriate limits were chosen on a run by run basis. Four standard deviations was the value used most often. All towers with numbers of hits above the limit were written to files formatted according to the QA EMCal extra reject list format. Then, for the PbSc this run-by-run information was merged into a global (i.e. run-independent) reject list as follows. A tower was considered globally hot (and, consequenly, made it into the global reject list) if it was hot in at least 10% of the runs processed. This conservative threshold still resulted in a relatively low number of hot towers outside W3, as shown in Table 4.2. The 5 good PbSc sectors have 26 hot towers (0.2%) out of a total of 12960.

The compiled list of dead and hot towers was used to mark individual particle hits as suspect, based on the cluster of towers the particle hit. This was done as follows. A cluster is considered bad if

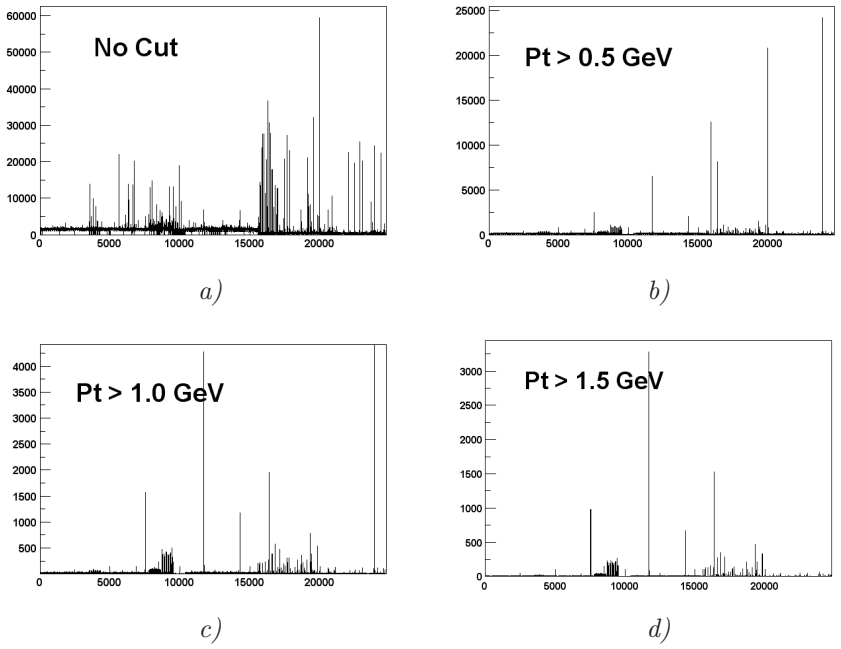

Figure 4.12: Number of hits vs EMCal tower index with 4 different p_T cuts for run 30009.

Table 4.2: Number of hot towers in the PbSc reject list.

sector	hot towers
W0	1
W1	12
W2	3
W3	400
E3	6
E2	4

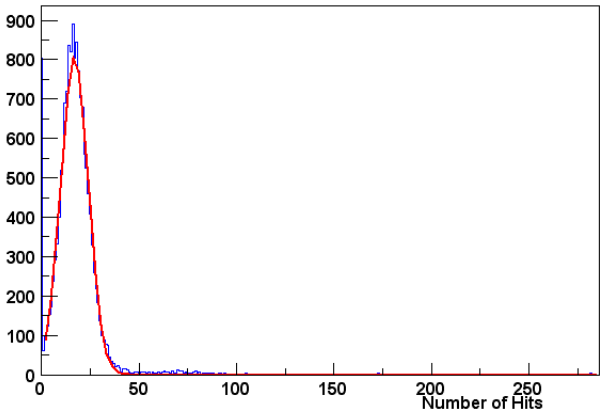

Figure 4.13: Gaussian fit to the distribution of number of hits with the cut $p_T > 1.0$ GeV for run 30009.

- either its "central" tower, i.e. the one with the highest energy deposit is marked as bad;
- or any tower in a 5×5 square minus the 4 corner towers around the central tower is bad.

An example for run 32123 is shown in Fig. 4.14 revealing the resulting improvement in the high energy cluster spectrum. Notice the dramatic reduction of the spectrum at high energies, which brings it in line with the expected exponential/power law drop off.

A similar study was carried out for the PbGl part of the calorimeter to tag towers with erroneous energy and/or timing response.

Quality Assurance

The Quality Assurance effort in PHENIX for RHIC Run 2 ([16]) actually served two purposes: one, as the name implies, to make sure that the data we process is physically meaningful and is not distorted by misbehaving detector parts. Two, with the results gained in assessing data quality we aimed to identify and

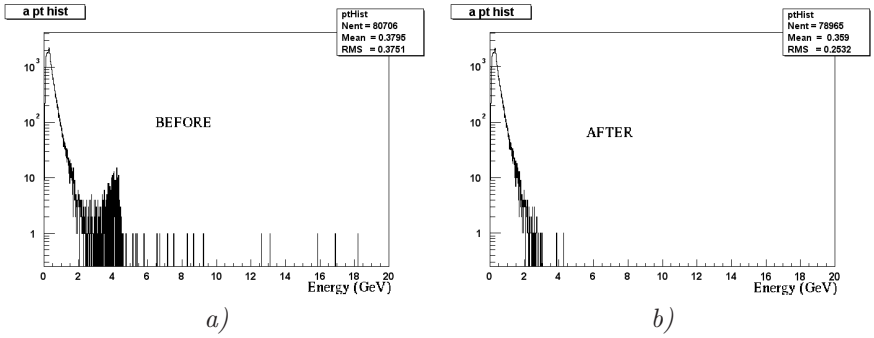

Figure 4.14: Energy spectrum *a)* before the hot tower removal; *b)* after the hot tower removal. Notice how the erroneous high energy tail of the distribution is gone.

correct any remaining detector miscalibrations. Since we lacked the capacity to process all data on tape for QA, it was decided to use data from the beginning of each detector run.

The framework set up for quality assessment worked as follows. Each subsystem provided their own QA code, which scanned the data event-by-event. Based on criteria set up within the individual subsystem working groups, the QA code created histogram files for each run. Another code evaluated those histograms and wrote out QA summary text files as well as assigned a numerical QA status to the run from that detector's point of view. Status 0 meant that the run had no problems, whereas any other number indicated various problems, the exact nature of which varied by subsystem.

The QA code written by me looked at both energy and timing performance of the Electromagnetic Calorimeter. Timing histograms were created for each sector and energy histograms were created for granules (pairs of sectors).

A relatively clean sample of photons went into the timing histograms; I only kept clusters meeting the following requirements:

- cluster energy $> 0.5\,\mathrm{GeV}$;
- photon probability > 0.1;
- no dead or hot towers in the cluster;

The energy histograms were filled with clusters from minimum ionizing particles that had:

- a matching charged track;
- cluster energy $> 0.17\,\mathrm{GeV}$;
- a shower shape not resembling that of a photon;

The positions, widths and fit parameters of the photon timing peak and the MIP peak were then extracted into the QA summary file.

Looking at this kind of information it had been quite clear at an early stage that W3 had serious problems:

1. W3 was not fully instrumented. That meant that before October 11 only 10 supermodules were working out of 18. Then an additional 4 were instrumented, making a total of 14. This fact not only dramatically lowered its acceptance (especially for the pair measurements) but also made acceptance calculations more complicated.
2. As W3 was instrumented last, it had the most faulty electronics board of all sectors, which also shows in its timing: its performance was significantly worse than those of the other 5 PbSc sectors.
3. W3 had literally hundreds of hot towers, many more than the rest of the PbSc sectors combined.

Therefore it was decided to exclude W3 from every analysis wherever timing was an issue.

After the work described above, the energy calibration seemed to be in quite a good shape (with the MIP peaks being stable and at the same level in all sectors), so the decision what status word individual runs should get was based mainly on the timing information. The basic scheme can be seen in Table 4.3.

We divided the EMCal into 3 logically different parts with different status words: PbSc West, PbSc East and PbGl. The status words for the 3 calorimeter parts were set as follows:

- **status=0**: there were no known problems with the run.
- **status=1**: there were no runs with PBSCW=1 or PBSCE=1, the reason being that even if the timing is bad, the run may still be perfect for analyses only using EMCal energy. PBGL=1 resulted in a list of 10 runs in the range 30000-30019, a relatively small portion of the data.

Table 4.3: Definition of the calorimeter status words

status word	meaning
−1	no QA status is set
0	run is good
1	run is bad
2	use at your own risk: bad timing
3	more dead towers in W3 than usual

- **status=2**: for PbSc this meant that a considerable fraction of the run had a photon peak more than 0.2 ns off zero *or* with $\sigma > 0.6$ ns in any of the 5 "good" PbSc sectors. There were no runs with PBGL=2.
- **status=3**: only applicable to PBSCW – it meant that there was a higher than usual number of dead towers in W3, but all other sectors looked fine.

We ended up with 278 runs in the database that had a status word of 0 for all 3 EMCal parts, 119 with PBSCW=2, 91 with PBSCE=2, of which 87 have status=2 for both. 17 runs (including those with PBGL=1) between runs 30000 and 30089 were marked with status=3.

Some results of the QA have been described above: it was the first to show there were problems with the tower-by-tower calibration in timing, helped to make sure the energy calibration was correct and every part of the detector was aligned, and, of course, it pointed out what data should be excluded from analyses.

Chapter 5

Experimental Technique

5.1 Principles

The extraction of neutral pions from the immense number of particles created in nucleus-nucleus collisions and the subsequent analysis thereof is one of the very elegant analyses aimed to reveal the properties of matter at high densities and temperatures. The analysis relies almost entirely on the electromagnetic calorimeter.

As described earlier, neutral pions decay to two photons with a lifetime of $\approx 10^{-16}$ s. Photons travel through the tracking detectors undetected and arrive at the calorimeter, where their energy is fully absorbed. To reconstruct the properties of the parent pion from them, we have to match up the directions and energies with those of their correct partner. Since it is not known which photon belongs to which, reconstruction of individual pions is impossible.

It is, however, possible to make statistical observations about the pions. This is done via the *combination method*, which works as follows. With some loose cuts, we select all particles that are potentially photons; then we make all possible pair combinations of those. With the assumption that the pair came from the same parent, the invariant mass and momentum of this virtual parent are calculated. The distribution of invariant masses (Fig. 4.4) will have a large background from the random incorrect combinations. The correct combinations, on the other hand, yield an invariant mass which is around the mass of the π^0, thus resulting in a peak on top of the background at $\approx 135\,\mathrm{GeV}/c^2$.

The amount of combinatorial background is estimated using the *event mixing method*. In event mixing, photons of one event are combined with similar photons of other events. This guarantees that paired photons can not have the same parent, and therefore, there are no correct combinations. Appropriately normalizing their invariant mass distribution, it can be subtracted from the real distribution, which allows the almost complete elimination of background.

Since the colliding ions are finite-sized, and the processes that occur in the collisions depend heavily on how "head-on" or "glancing" collisions are, we have to be able to characterize them in that respect. For that a variable called *centrality* is used. This is an experimentally determined percentile, which – somewhat counter-intuitively – is defined so that small values mean more central ("head-on") and large values more peripheral ("glancing") collisions. The centrality of a collision determines some geometrical parameters, like the number of individual nucleon-nucleon collisions (N_{coll}) and the number of nucleons that actually participate in at least one nucleon-nucleon collision (N_{part}). With the help of a Glauber model calculation (see e.g. [17]), the measured values of these give an estimate of the centrality of a collision. The percentage of the total collision cross section indicates the fraction of the data relative to all possible collision geometries, corrected for triggering inefficiencies. Events are categorized into centrality classes, for example the $0-10\%$ class means the 10% of the data with the most central collisions [18].

To make it easier to see if "new physics" happens in heavy ion collisions, spectra are often compared to corresponding spectra from $\mathrm{p}+\mathrm{p}$ collisions. The *nuclear modification factor* R_{AA} is a quantity introduced to make such comparisons straightforward. R_{AA} is defined as the ratio of the production cross sections in heavy ion collisions and $\mathrm{p}+\mathrm{p}$ collisions, respectively, scaled by the number of binary collisions N_{coll} in the former:

$$R_{\mathrm{AA}}^{\mathrm{h}} = \frac{\mathrm{d}^3\sigma^{\mathrm{AA}\to\mathrm{h}}/\mathrm{d}y\mathrm{d}^2p_{\mathrm{T}}}{\mathrm{d}^3\sigma^{\mathrm{pp}\to\mathrm{h}}/\mathrm{d}y\mathrm{d}^2p_{\mathrm{T}}} \cdot \frac{1}{N_{\mathrm{coll}}}\,, \tag{5.1}$$

where y and p_{T} are the hadron rapidity and transverse momentum, respectively. A mathematically less rigorous but perhaps more expressive definition is

$$R_{\mathrm{AA}} = \frac{\text{Yield in A + A collisions}}{\text{Yield in p + p collisions}} \cdot \frac{1}{N_{\mathrm{coll}}}\,. \tag{5.2}$$

If R_{AA}'s value is consistent with 1 that means that processes occuring in heavy ion collisions are probably not different from what happens in $\mathrm{p}+\mathrm{p}$ collisions, only there is more of them. On the other hand, if R_{AA} significantly differs from 1, that indicates qualitatively different physics in heavy ion collisions.

5.2 Au + Au collisions at 62.4 GeV

5.2.1 Event selection

Two essentially independent analyses of a total of 40 million events of the 62.4 GeV data set were performed. The two analyses were done by different people, using different codes, cuts, bad modules maps, energy scale corrections and systematic error estimates. Analysis1 was performed on both the PbSc and PbGl parts of the calorimeter, while Analysis2 was done using the PbSc sectors only. (The auther participated in Analysis2.) Differences between the two analyses will be pointed out below.

We required that each event satisfy the following criteria:

- the z coordinate of the collision vertex as determined by the BBC detectors be within 300 mm of the geometrical center of the detector;
- both BBCs have at least 2 hits.

5.2.2 Cuts

We used a moderate energy threshold cut of $E > 0.2$ GeV.

We required that the central tower (tower with largest energy) be at least 8 cm from the edges of the sectors.

Clusters at least partly in a 3 tower by 3 tower square around bad towers were also excluded. Bad module maps were determined statistically for each analysis and the efficiency losses incurred thus were taken care of with corrections. The bad module maps differ quite significantly for the two analyses ($\approx 35\%$ of towers are rejected in Analysis1 but only $\approx 5\%$ in Analysis2), but the yields corrected for the different acceptances agree well. This shows that the bad module maps and the corresponding loss in acceptance are well under control.

We used a cut on the energy asymmetry (defined as $\alpha = \frac{|E_1 - E_2|}{E_1 + E_2}$) of the photon pair $\alpha < 0.8$ for Analysis2 and $\alpha < 0.7$ for Analysis1. Real photon combinations have a flat asymmetry distribution, so this cut removes only a fraction of them and the efficiency loss is well known. On the other hand, a lot of false photon combinations (combinatoric background) are very asymmetric in energy, and this cut removes those.

Furthermore, in Analysis2 when making invariant mass distributions we used only photon pairs in the same sector.

Table 5.1: Centrality bins and the corresponding cuts in BBC percentile.

centrality	BBC percentile
0 –10	0–11.9
10–30	11.9–35.8
30–60	35.8–71.7
60–83.7	71.7–100

5.2.3 Centrality determination

Events were assigned into centrality classes based on the charge sum in the two BBCs. As already mentioned, only events with at least 2 hit phototubes in each BBC were accepted. With this requirement, the BBC efficiency is 83.7%.

Cutting on the charge sum allows for only a rough centrality determination. Also, the BBC alone is not able to resolve centralities beyond 60%. However, BBC was the only detector we could use to determine centrality, because at 62 GeV most of the spectator neutrons do *not* hit the ZDC.

Based on the corrected charge sum, a quantity called *BBC percentile* was determined for each event, and for classifying events into centrality bins, we cut on this variable. The cuts made on the BBC percentile had to be scaled by the BBC efficiency for our event selection to get the true centrality. Our cuts on the BBC percentile and the corresponding centrality bins are summarized in Table 5.1. When scanning the data we used finer binning (see the next chapter) then results from different bins were added up.

5.2.4 π^0 yield extraction

The π^0 extraction code for this analysis fills a number of multi-dimensional histograms with several combinations of cuts. (Multi-dimensional histograms were chosen over ntuples early on because of the prohibitive size of ntuple files.) The multi-dimensional histograms contain invariant mass distribution of photon pairs in different p_{T} and centrality bins. Photons are paired both within the same event (real histograms) and, for background determination, across events (mixed event histograms). Only events of the same centrality class and vertex class are mixed. Up to 7 events per event class are buffered for mixing. Our centrality bins for mixing were $0-5\%$, $5-10\%$, $10-15\%$, $15-20\%$, $20-30\%$,

$30-40\%$, $40-50\%$ $50-60\%$, $60\%-83.7\%$; the vertex bins were 5 cm wide from -30 cm to 30 cm.

The mixed event histograms are normalized to the corresponding real photon pair invariant mass distributions below and above the π^0 peak. The mixed event background is then subtracted from the real distribution, which in turn is fitted with a Gaussian. The peak position, width, yield with their respective errors are all recorded on the count sheet (see Figs. 5.1, 5.2). The yield is determined by counting the number of entries in the histogram in a $\pm 2\sigma$ interval around the (smoothed) peak position (see Fig. 5.3). Results for wider centrality bins are obtained by adding up the raw yields from the narrower centrality bins.

5.2.5 Acceptance and efficiency

The geometrical acceptance is calculated by a fast Monte Carlo that generates π^0s with a vertex within $-300\,\mathrm{mm} < z_{\mathrm{vertex}} < 300\,\mathrm{mm}$ in a rapidity range of $-0.5 < y < 0.5$. The rapidity distribution of particles produced in Au + Au collisions is symmetric with respect to $y = 0$ and was assumed to be flat.

The dead, hot, or (in most cases) mis-calibrated towers and neighboring towers are rejected in the analysis of real data as well as in the FastMC. In both analyses the immediate neighbor-towers are rejected (3×3 around a bad module). The pure acceptance for pairs in PbSc is shown in Fig. 5.4.

The reconstruction efficiency for neutral pions was defined as

$$\epsilon(p_T) = \frac{f(p_{T_{out}})}{f(p_{T_{in}})}$$

where $f(p_{T_{in}})$ denotes the input spectrum of neutral pions for which both decay photons lie on an active region of the detector and $f(p_{T_{out}})$ the actually measured spectrum.

The efficiency is calculated using a FastMC (different ones for the 2 analyses) by generating a flat input p_{T} distribution that is weighted by a physically realistic function. This is done iteratively until convergence is reached with the parameters of the corrected π^0 spectrum. Analysis cuts and fiducial cuts are applied in the simulation. The energy of the decay photons is smeared using functions derived as follows.

We simulated π^0s with a flat spectrum in the $0 < p_{\mathrm{T}} < 10$ GeV/c range and with a uniform ($|z| < 30$ cm) vertex distribution. Next we selected only the events in which both photons ended up in the calorimeter ("forced acceptance').

The energy of the simulated decay photons was first smeared with an additional constant term so that the resolution matched the one observed in the

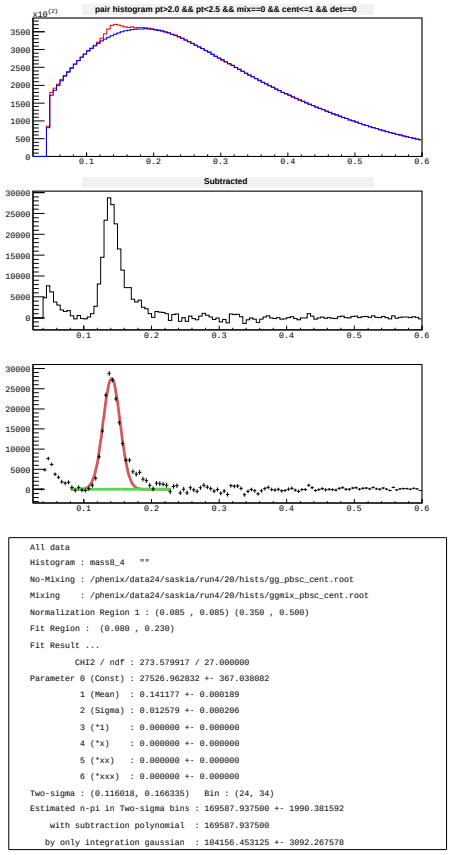

Figure 5.1: Sample control output of the π^0 extraction program. This plot shows the π^0-peak measured in the PbSc in the range $2.0 < p_T < 2.5$ GeV in our most central events $(0 - 10\%)$. The top plot shows the invariant mass distribution in real events along with the scaled mixed events background. The middle plot shows the π^0 after background subtraction, and finally, the bottom plot shows the Gaussian fit to the π^0 peak.

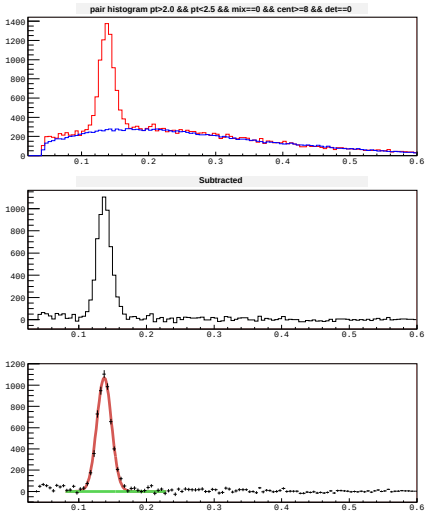


```
All data
Histogram : mass8_4   ""
No-Mixing : /phenix/data24/saskia/run4/20/hists/gg_pbsc_periph.root
Mixing    : /phenix/data24/saskia/run4/20/hists/ggmix_pbsc_periph.root
Normalization Region 1 : (0.085 , 0.085) (0.350 , 0.500)
Fit Region :  (0.080 , 0.230)
Fit Result ...
         CHI2 / ndf : 56.892227 / 27.000000
Parameter 0 (Const) : 1068.442398 +- 20.662791
          1 (Mean)  : 0.137607 +- 0.000202
          2 (Sigma) : 0.010830 +- 0.000190
          3 (*1)    : 0.000000 +- 0.000000
          4 (*x)    : 0.000000 +- 0.000000
          5 (*xx)   : 0.000000 +- 0.000000
          6 (*xxx)  : 0.000000 +- 0.000000
Two-sigma : (0.115947, 0.159268)   Bin : (24, 32)
Estimated n-pi in Two-sigma bins : 5562.311035 +- 88.904442
    with subtraction polynomial  : 5562.311035
    by only integration gaussian  : 3480.662109 +- 128.461197
```

Figure 5.2: Sample control output of the π^0 extraction program showing the π^0 peak as measured in the PbSc in the range $2.0 < p_T < 2.5$ GeV in our most peripheral $(60-83\%)$ events.

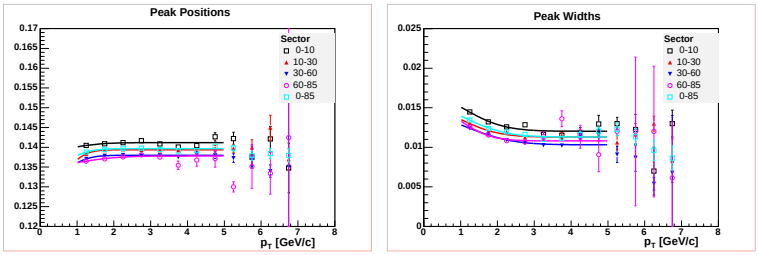

a) *b)*

Figure 5.3: Extracted π^0 peak positions and widths as a function of π^0 p_T for different centralities. The fit functions were used to smooth the p_T-dependence of the yields: in every bin the π^0 peak area was integrated over a $\pm 2\sigma_m$ interval around m, where both m and σ_m were taken from fit functions.

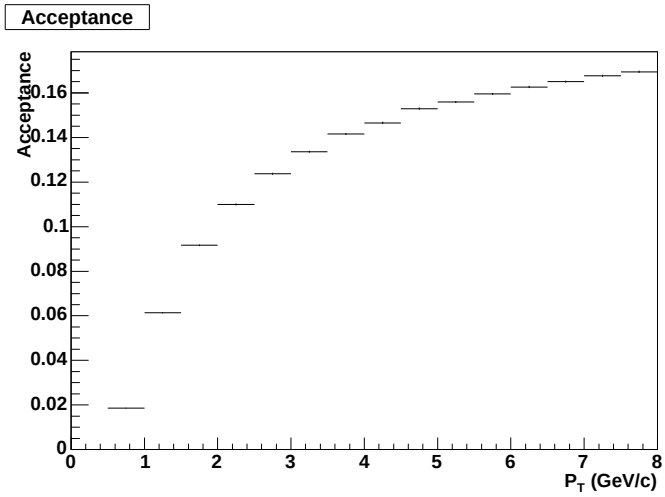

Figure 5.4: Acceptance for pairs in PbSc.

data. Next the deadmap used in the data analysis was applied, and the surviving towers were embedded in real events (without any attempt to match the vertices), finally we ran the clustering again and wrote out all clusters that had any contribution from simulated towers. We then formed the $E_{\mathrm{core}}/p_{\mathrm{tot}}$ ratio as a function of the simulated photon momentum p_{tot}, where E_{core} is the measured energy of the simulated photon after embedding and re-clustering. Examples of these *smearing functions* are shown in Fig. 5.5. (The peak is centered at 1, because the energy and the momentum of a photon differ only by a factor of c and in high energy physics units $c = 1$.) These smearing functions are then applied to the energy of the decay photons in the FastMC before additional cuts are made and invariant mass is reconstructed.

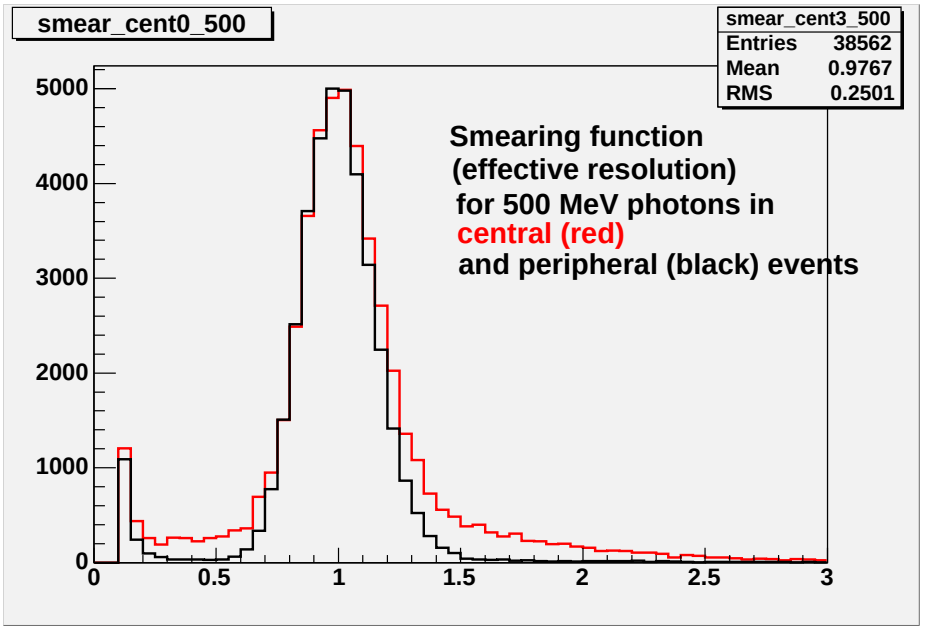

Figure 5.5: Smearing functions ($E_{\mathrm{core}}/p_{\mathrm{tot}}$ ratios) for 500 MeV simulated photons embedded in real data for peripheral (black) and central (red) events. The effect of overlaps is clearly visible as the long tail in central events.

A threshold energy cut of 0.2 GeV on the smeared photon energies is applied. Smeared photon energy asymmetry is required to be less than 0.7 (0.8)

in Analysis1 (Analysis2). Both analyses extract yields with and without a PID cut. (The PID cut in essence characterized the shower shape in the calorimeter, relying on the fact that the shape of electromagnetic showers caused by photons or electrons differ from hadronic showers. The cut relies on an analytic parametrization of energy sharing and fluctuations between towers in electromagnetic showers; then a simple χ^2 test is used to characterize the degree of matching.)

The reconstruction efficiency accounts for the effects of energy smearing and photon losses due to PID cuts. The first step is to match the width obtained in the FastMC to that measured in peripheral events. This allows one to determine the resolution with the current calibration. This was determined to be

$$\sigma_E/E = 8.2\%/\sqrt{E(\mathrm{GeV})} \oplus 5.8\%.$$

for the PbSc. The energy smearing of the decay photons is parametrized as a ratio of reconstructed energy to true energy as a function of true energy, for each centrality selection. This parameterization is implemented in the FastMC, and the π^0 line-shapes (see Fig. 5.6) are shown to reproduce those in the data for each centrality.

The energy smearing for the PbGl in the FastMC was

$$\sigma_E/E = 8.5\%/\sqrt{E(\mathrm{GeV})} \oplus 9\%,$$

the large constant term coming mainly from the unbalanced gains of towers. The position smearing was parametrized by

$$\begin{aligned} \sigma_x(0^\circ) &= 6.7\,\mathrm{mm}/\sqrt{E(\mathrm{GeV})} \oplus 1.6\,\mathrm{mm} \\ \sigma_x(\vartheta) &= (28\,\mathrm{mm} \cdot \sin\vartheta) \oplus \sigma_x(0^\circ) \end{aligned}$$

where ϑ is the incident angle with respect to the detector surface ($\vartheta = 0^\circ$: perpendicular impact). The products of the acceptance and the calculated reconstruction efficiencies are shown in Fig. 5.7.

5.2.6 Corrections for photon conversion

Due to the material in front of the calorimeter a certain fraction of photons are converted ($\gamma \rightarrow e^+e^-$). However, these photons are not necessarily "lost" for the π^0 analyses (except if a charge veto is applied in the photon identification - which wasn't the case in either of the analyses). If the conversion happens "late", at large radii, close to the EMCal, the e^+e^- pair ends up as one single

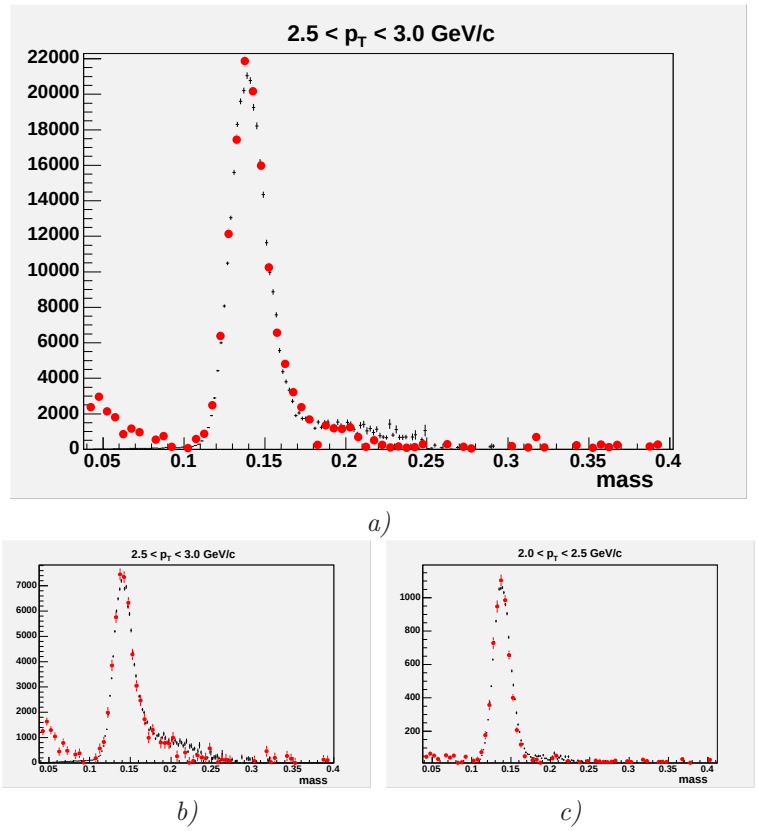

Figure 5.6: π^0 mass peaks in the p_T range $2.0\,\mathrm{GeV} < p_T < 3.0\,\mathrm{GeV}$ in our *a)* minimum bias, *b)* most central, and *c)* most peripheral bin. Red dots are data and black points are from FastMC.

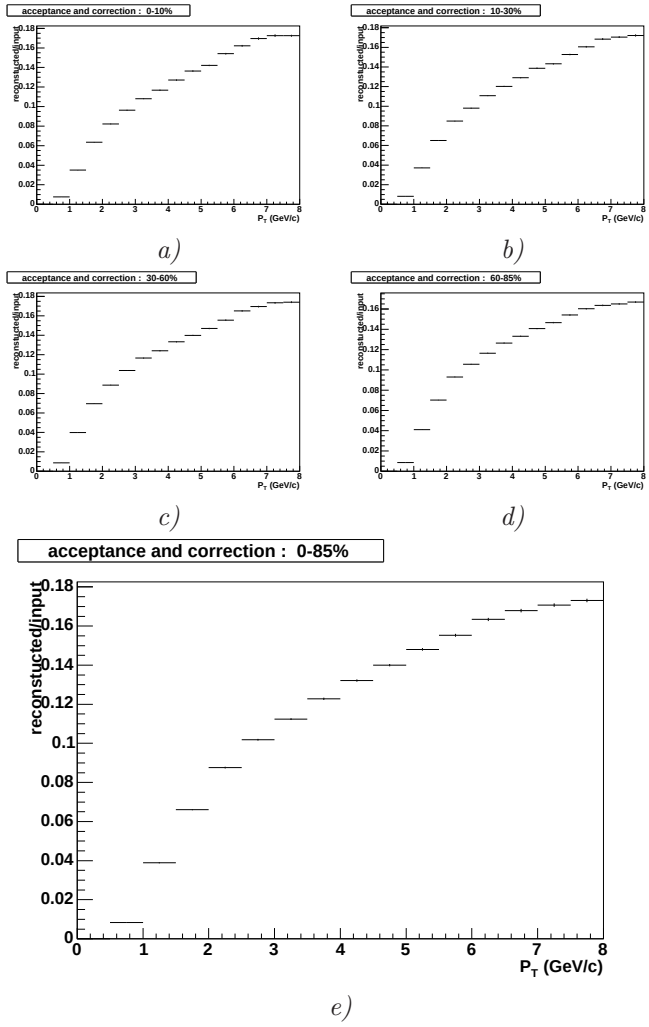

Figure 5.7: Acceptance×efficiencies for centrality bins *a)* $0-10\%$, *b)* $10-30\%$, *c)* $30-60\%$, *d)* $60-83.7\%$ and for *e)* minimum bias data.

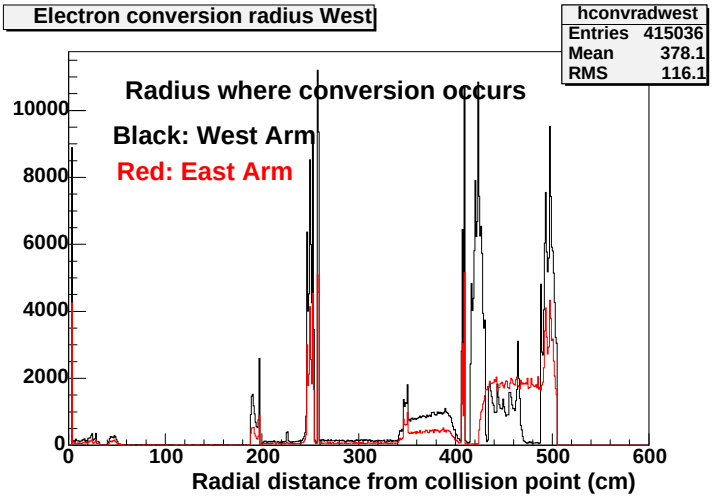

Figure 5.8: Radius (in cm) where conversions occur in the West Arm (black) and in the East Arm (red) PbSc sectors if at least one electron reaches the PbSc calorimeter.

cluster, passes the (loose) shower shape cut (if any), and the energy is close to the original E_γ. Therefore, the original π^0 is reconstructed with the proper mass and $p_{\rm T}$. If the conversion occurs "early", still inside the magnetic field, the decay electrons are swept in the opposite direction, and the photon is lost. The same happens if the photon converts "late" but the decay is very asymmetric, and the electrons don't end up in the same cluster. Obviously, both effects depend not only on the radius where the decay occurs, but also on the photon momentum.

The radii where conversions occur in the East and West Arm PbSc calorimeter is shown in Fig. 5.8. The peaks in the East Arm are smaller since East has only two PbSc sectors. Different detectors (PC2, TEC vs Aerogel) are clearly visible. Note that many of these conversions produce e^+e^- pairs that ultimately end up in the same cluster.

As opposed to previous analyses, where the photon conversion probability was expressed as a single number, we made more detailed studies of conversion losses as a function of photon energy. Based upon single π^0 and HIJING simulations, we established the *net conversion loss function*, the probability as a

function of E_γ that the photon converts *somewhere* and the two decay electrons do not end up in the same EMCal cluster. We found (see Fig. 5.9) that

- this function is slightly different in the East and West Arm of the detector;
- it stabilizes quickly at a constant value;
- but it changes rapidly at very low energies (influencing the observed yields from very asymmetric π^0 decays).

One motivation for the $E_\gamma > 0.2$ GeV cut is to avoid the steeply varying part of the new conversion loss function.

The actual functions used in the FastMC were

$$0.0619108\, e^{-1.85309E+1.05974E^2} \quad \text{if E} < 1.0 \text{ GeV;} \quad 0.028 \text{ otherwise}$$

for the East Arm and

$$0.0549512\, e^{(-1.69132E+1.05333E^2)} \quad \text{if E} < 1.0 \text{ GeV;} \quad 0.029 \text{ otherwise}$$

for the West Arm.

5.2.7 Off-vertex, but reconstructed π^0s

Due to the limited energy and position resolution (i.e. the width of the π^0 mass peak) pions that are not from the collision vertex might also be properly reconstructed and add to the raw pion count. There are two major sources of such pions: real secondaries (from nuclear interaction with structural elements of the detector) and feed-down pions from decay of higher mass mesons (the primary source being K^0_S, because the 3-body decays of η, etc. have limited phase-space at moderate and high p_T).

Simulations using HIJING and the full detector geometry (see Fig. 5.10) reveal that

- the probability to reconstruct off-vertex π^0s decreases rapidly with radial distance from the beampipe, but is almost constant with z;
- the main source of off-vertex, but reconstructed π^0s is the beampipe and the magnet poleface;
- the contribution from kaons changes from 14% in the most peripheral events to 19% in the most central events (although most of these are at very low p_{T});

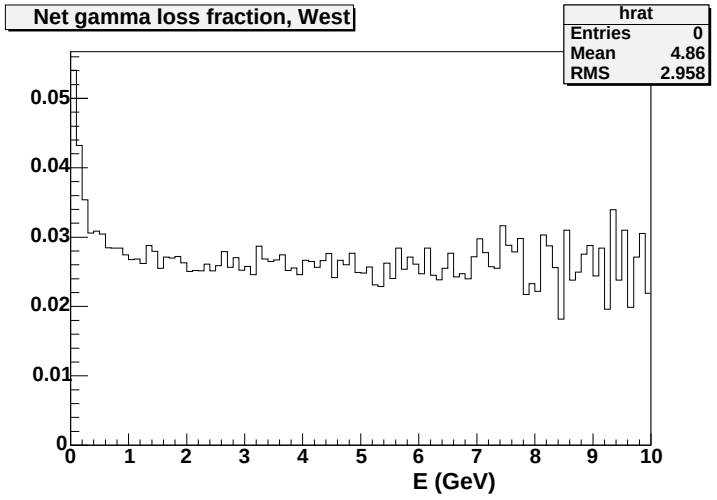

Figure 5.9: Fraction of photons lost due to conversions in the West Arm as a function of photon energy.

- the contamination from off-vertex pions is 4% of the raw yield at $p_T = 1.5\,\mathrm{GeV/c}$ and probably decreases with increasing transverse momentum.

5.2.8 Systematic errors

The various sources of systematic errors are described in this sections. All errors are estimated as 1σ errors.

The systematic errors are summarized in Table 5.2 and are characterized as follows:

Type A (probably) p_T-correlated error, however, the correlation is not known (e.g. points at low p_T might move down while points at high p_T move up). Thus, it is most conservative to treat this error as p_T-uncorrelated.

Type B p_T-correlated error, all points move in the same direction.

Type C p_T-correlated error, all points move by the same factor (scale error).

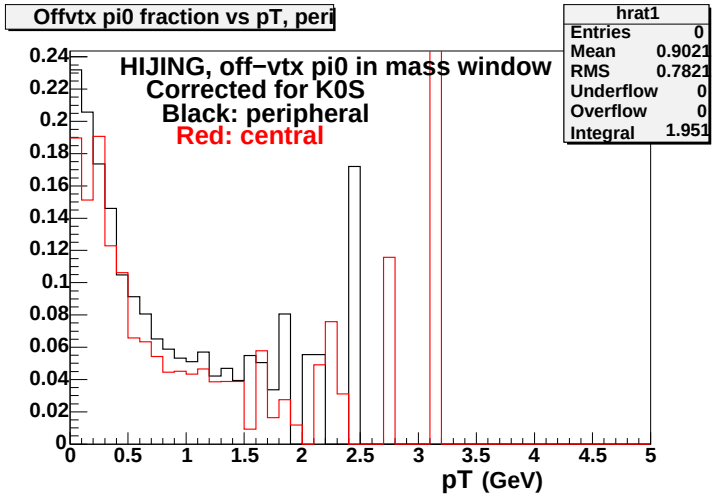

Figure 5.10: Fraction of off-vertex, but reconstructed π^0s as a function of p_T based upon HIJING simulations. These are pure secondaries, feed-down from K^0_S is not included.

If the systematic error of type B is parametrized by a linear function then the constant term of this function can be treated as a scale error (type C). The following sections describe in some detail how the errors were estimated.

Table 5.2: Systematic errors of the neutral pion invariant yields. The error sum for a given p_T column is the quadratic sum of the p_T-dependent errors given in that column and the p_T-independent errors. The errors are the same for PbSc and PbGl.

	$p_T$indep.	2 GeV	6 GeV	type
peak extraction	5.0%			A
geometric acc.		3.0%	2.0%	B
π^0 reconstr. eff.		5.0%	5.0%	B
energy scale		4.0%	9.0%	B
Conversion corr.	3.0%			C
Total error		9.1%	12%	

Peak extraction

The error in the peak extraction is estimated by varying fit parameters and the normalization window. This was done in previous analyses (see for instance [19]). The error is $\approx 5\%$.

Energy scale

The tuning of the energy scale with the FastMC was done on a per-sector (Analysis1) or a per-granule (Analysis2) basis. The maximum difference in the energy corrections of the two independent analyses is about 1%. After tuning, the π^0 masses from the real data and the FastMC agree mostly to within 1% even at high p_{T}. Therefore, the systematic uncertainty on the absolute energy scale is estimated to be $\sim 1\%$. Since our spectra are steeply falling, however, a 1% uncertainty on the energy scale can cause several percent uncertainty in the yields.

Reconstruction efficiency

The comparison of corrected spectra with different PID cuts give an idea of the reconstruction efficiency. Figs. 5.11 to 5.14 show the ratios of corrected spectra with and without the shower shape cut for Analysis2 for the different centralities. (Comparison between different PID cuts in Analysis1 looks similar.) The agreement is within 5% with the largest deviations in the central bins.

This total error in the reconstruction efficiency is the quadrature sum of the two contributions and is shown in Table 5.2.

Conversion correction

The error in the correction for losses due to conversions is 3.0% for both PbSc and PbGl, independent of centrality. This number allows for 1.5% error on the net conversion loss function, which in turn is the maximum variation of this function at low photon energies (see Fig. 5.9). Off-vertex π^0s are not subtracted (also the fraction from kaon feed-down above $2\,\mathrm{GeV}/c^2$ is not known).

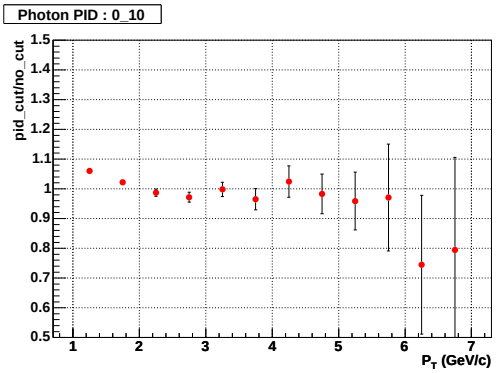

Figure 5.11: Reconstruction efficiency for neutral pions (shower shape cut) as obtained with the FastMC for $0-10\%$ central events. The energy asymmetry cut is $\alpha < 0.8$.

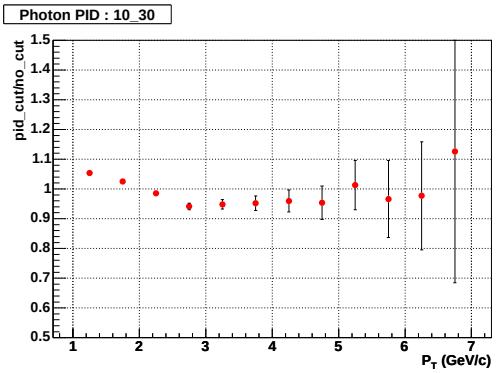

Figure 5.12: The ratios of corrected spectra with and without the shower shape cut for Analysis2 for $10-30\%$ centrality, which gives an idea of the reconstruction efficiency. The energy asymmetry cut is $\alpha < 0.8$.

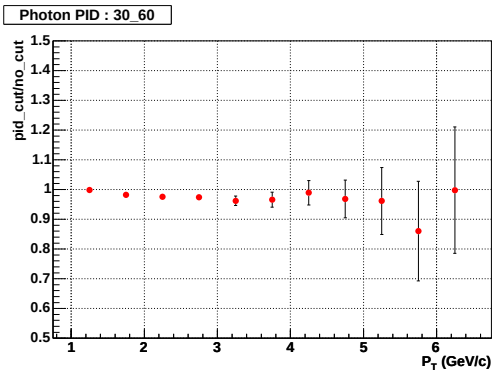

Figure 5.13: The ratios of corrected spectra with and without the shower shape cut for Analysis2 for $30-60\%$ centrality, which gives an idea about the reconstruction efficiency. The energy asymmetry cut is $\alpha < 0.8$.

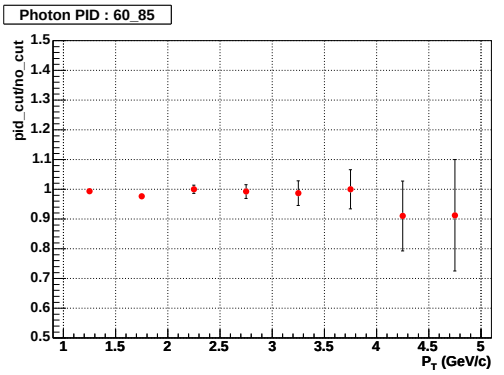

Figure 5.14: The ratios of corrected spectra with and without the shower shape cut for Analysis2 for $60-84\%$ centrality, which gives an idea about the reconstruction efficiency. The energy asymmetry cut is $\alpha < 0.8$.

5.3 Au + Au collisions at 200 GeV

5.3.1 Data reduction

This analysis was performed on a subset of the 200 GeV Au + Au data taken in the second year of RHIC's running. We required that the following criteria be met:

- the magnet was on at its full current for the whole run ("full field");
- no problems in the PbSc sectors in the East Arm (PBSCE status=0, cf. 4.3.2);
- either no problem in the calorimeter in the West Arm or problem only in sector W3 (PBSCW status=0 or 3). We allowed runs with problematic W3 because we excluded that sector from our analysis.

As for individual events, we only used minimum bias events where $|z| < 30\,\mathrm{cm}$. The cuts on individual clusters were the following:

- cluster energy $> 0.05\,\mathrm{GeV}$,
- fiducial cuts,
- PID cuts,
- asymmetry cut $\alpha < 0.8$.

Event mixing was done for every 5 events within the same centrality and vertex class. The vertex bins for mixing were 5 cm wide, the centrality classes were 0-5%, 5-10%, 10-15%, 15-20%, 20-30%, 30-40%, 40-50%, 50-60%, 60-70%, 70-80%, 80-92%.

5.3.2 Particle identification

To gain a better understanding of the π^0 yields, particularly at high p_{T}, we stored invariant mass distributions for the following combinations of PID cuts.

- No PID cuts
- $|\mathrm{TOF}| < 3.0\,\mathrm{ns}$
- $|\mathrm{TOF}| < 1.2\,\mathrm{ns}$

- shower shape $\chi^2 < 10.0$
- shower shape $\chi^2 < 3.0$
- $|\mathrm{TOF}| < 3.0\,\mathrm{ns}$ and $\chi^2 < 10.0$ (final "favorite" cuts)
- $|\mathrm{TOF}| < 3.0\,\mathrm{ns}$ and $\chi^2 < 3.0$
- $|\mathrm{TOF}| < 1.2\,\mathrm{ns}$ and $\chi^2 < 10.0$
- $|\mathrm{TOF}| < 1.2\,\mathrm{ns}$ and $\chi^2 < 3.0$

The yields were extracted for all combination of cuts and the spectra corrected by the efficiencies (as determined by the embedding) were compared. Since the tighter TOF cut ($|\mathrm{TOF}| < 1.2\,\mathrm{ns}$) is known not to be reproduced well by simulation, we did not use this cut in our systematic error determination. The systematic error due to the PID cuts was determined by comparing all other corrected spectra to the loose PID cuts ($|\mathrm{TOF}| < 3.0\,\mathrm{ns}$ and $\chi^2 < 10.0$). The raw yields used to produce the final spectra were also using these loose ("favorite") PID cuts.

5.3.3 Peak extraction

After careful study of the peak position and width vs. p_{T} for all centrality classes, we fixed the extraction window. We integrated the background-subtracted histogram within $\pm 2\sigma$ of the fixed mean.

The position and width are determined from the plots in such a way that a smooth curve goes through the majority of the points. This is done for each centrality class. This new fitting procedure permits to go further in p_{T}, since the former "fitting" method was not reliable below $N_{\pi^0} \approx 20$ counts. The new minimum number of counts in the last p_{T} bin of the raw spectra was $N_{\pi^0} \approx 5$ counts (i.e. we exclude p_{T} bins having less than this statistics).

5.3.4 Pion yields for different PID cuts

When we compared the raw yields for different PID cuts with the raw yields extracted with no PID cuts, we obtained the following "efficiencies":

Peripheral:

- $|\mathrm{TOF}| < 3.0\,\mathrm{ns}$ efficiency $\approx 90\%$
- $|\mathrm{TOF}| < 1.2\,\mathrm{ns}$ efficiency $\approx$ 90-60% with increasing p_{T}

Table 5.3: Parameters of the PbSc acceptance fit, Eq. (5.3), used in the present analysis.

A	$2.37 \cdot 10^{-1} \pm 7.92 \cdot 10^{-4}$
B (GeV/c)	$2.88 \cdot 10^{-3} \pm 9.35 \cdot 10^{-5}$
a	$1.06 \cdot 10^{-1} \pm 1.28 \cdot 10^{-2}$
b (GeV/c)	$1.04 \pm 1.68 \cdot 10^{-2}$

- (shower shape) $\chi^2 < 10.0$ efficiency $\approx 100\%$
- $\chi^2 < 3.0$ efficiency $\approx 95\%$

Central:

- $|\mathrm{TOF}| < 3.0\,\mathrm{ns}$ efficiency $\approx$ 100-90% with increasing p_{T}
- $|\mathrm{TOF}| < 1.2\,\mathrm{ns}$ efficiency $\approx$ 100-65% with increasing p_{T}
- $\chi^2 < 10.0$ efficiency $\approx 90\%$
- $\chi^2 < 3.0$ efficiency $\approx$ 70-60% with increasing p_{T}

The efficiency of the tight TOF cut is not reproduced by simulation, but the looser TOF cut and the χ^2 cut efficiencies are reasonably well reproduced.

5.3.5 PbSc acceptance correction

For the PbSc acceptance correction we used an improved fit to the acceptance function with respect to the one used earlier in the collaboration. The following improved fit reproduces better the shape of the acceptance distribution at low p_{T}. ($p_{\mathrm{T}} < 1.5\mathrm{GeV}/c$):

$$\mathcal{A}(p_{\mathrm{T}}) = (A + B \cdot p_{\mathrm{T}}) \cdot \left(1 - \mathrm{e}^{a - b \cdot p_{\mathrm{T}}}\right), \tag{5.3}$$

as can be seen in Fig. 5.15. The parameters of the fit are reported in Table 5.3.

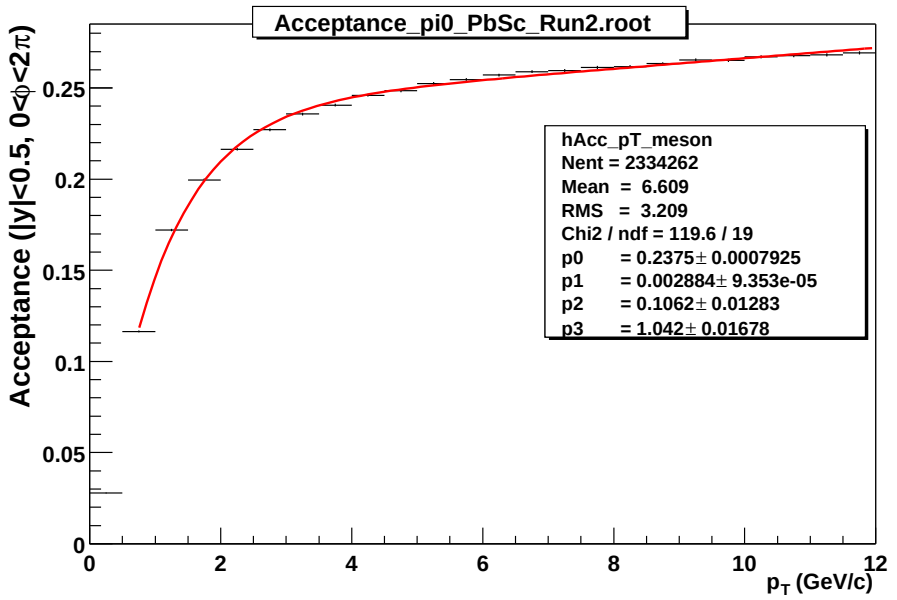

Figure 5.15: PbSc acceptance for $\pi^0 \rightarrow \gamma\gamma$ (per unit pseudorapidity and full ϕ) as a function of the π^0 p_{T}. The solid line is the result of a fit with Eq. (5.3).

5.3.6 PbSc final efficiency determination

Efficiencies were determined by detailed embedding studies. After obtaining the efficiencies for each p_{T} bin, set of analysis cuts and centrality class, each distribution was fitted as a function of π^0 p_{T} with the following expression:

$$\mathcal{E}(p_{\mathrm{T}}) = C_0 + C_1 \cdot p_T + C_2 \cdot p_T^2 + C_3 \cdot \ln(p_T) + C_4 \cdot \ln^2(p_{\mathrm{T}})\,. \qquad (5.4)$$

This function reproduces very well the shape of the efficiency distributions as can be seen from the low χ^2 values of the fits in the left plot of Fig. 5.16. Data and fit are in similarly good agreement in the efficiency plots of each centrality class, not included here.

Above 7 GeV/c the computed efficiencies drop because of the absence of feeding from higher p_{T} values in the $0-8$ GeV/c embedding (end-point effect), thus

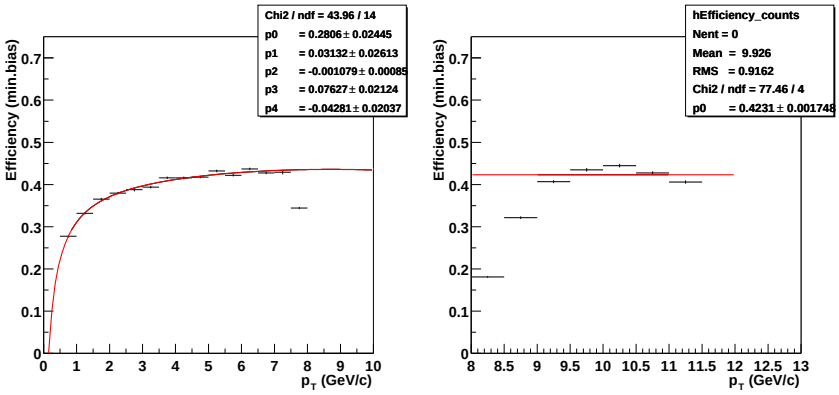

Figure 5.16: Efficiency 0-10% as a function of p_T ("favorite" set of cuts). Left: $0-8\,\mathrm{GeV}/c$ single-π^0 embedding efficiencies fitted with Eq. (5.4). Right: $8-14\,\mathrm{GeV}/c$ single-π^0 embedding efficiencies fitted with a linear function between 9 and $12\,\mathrm{GeV}/c$. (For explanation, see the text.

we fit the distributions below $7\,\mathrm{GeV}/c$ and then extrapolate their asymptotic behaviour to larger transverse momenta.

We then make use of the second high-p_{T} ($8-14\,\mathrm{GeV}/c$) pion merged production to cross-check the quality of the extrapolation (unfortunately we could not merge both productions since they had different statistics and the efficiency calculations were performed independently for both sets). Because of p_{T}-smearing and end of the input π^0 distribution at $14\,\mathrm{GeV}/c$ (i.e. absence of cluster "feeding" from the lower and higher energy side), the high-p_{T} efficiencies are only reliable in the range $\approx 9-12\,\mathrm{GeV}/c$. In this range, we then perform a linear fit of the efficiency distributions (plot in the right hand side of Fig. 5.16 and the corresponding plots in each centrality class). The value of the fit (p_0 in the plot boxes) is, in all cases, very close to the extrapolated value from lower p_{T} efficiencies. (The absolute differences are below 2.5%.) This fact allows us to perfectly rely on our efficiency fit for all relevant p_{T} values between 0 and $12\,\mathrm{GeV}/c$.

5.3.7 Yield shift correction for finite binning of the spectra

In order to take into account the effect of the finite binning ($0.5\,\mathrm{GeV}/c$) in the steeply falling p_{T} spectra, we apply a correction to the final combined invariant yield in each bin according to the following procedure.

- We fit the final spectrum with the standard power-law form $A/(p_{\mathrm{T}}+p_0)^n$ (fixed $p_0 = 1.72\,\mathrm{GeV}/c$) above $p_{\mathrm{T}} = 1\,\mathrm{GeV}/c$.
- For each p_{T} bin we compute the value of the integral of the power-law fit at the bin. The integral divided by the bin width gives us the average value of the yield for that bin.
- We then multiply the value of the yield at the bin by the factor: [value of the power-law fit at the center of the p_{T} bin]/[average value of the yield at the bin].

The net effect of this recipe is a small (few %) shift downwards of the invariant yield (y-axis) as can be seen in Fig. 5.17. The advantage of this "y-shifting" method as opposed to "x-shifting" is that we can straightly divide p + p and Au + Au fully corrected yields *at exactly the same p_T bin value* (the p_{T}-shift method gives different bin positions for spectra with different shapes).

5.3.8 PbSc systematic errors

The major sources of systematic error are summarized in Table 5.4. In each case, the error is classified as "(non) centrality-correlated" and/or "(non) p_{T}-correlated". The definitions of these classifications are given here:

CCC = "Centrality-correlated error": Errors that cancel in ratios of centralities.

PTC = "p_{T}-correlated error": Errors that move the spectrum consistently up/down (i.e. the "non PTC" is the "bin to bin" error).

Systematic errors were estimated by studying the effect of varying various parameters in the work processes shown in Table 5.4.

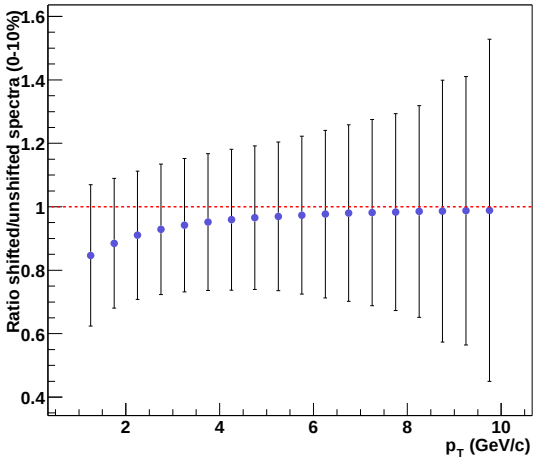

Figure 5.17: Ratio of shifted over unshifted yield for the 0-10% π^0 spectrum.

Table 5.4:

List of systematic uncertainties. When a range of values is given, then the first number in the range is the error at low p_T and the second is the error at high p_T.

Source of Error	Percent Error	[(non) CCC]	[(non) PTC]
Raw yield extraction	10%	[non CCC]	[non PTC]
Energy scale	3-8%	[CCC]	[PTC]
PID cuts	8%	[non CCC]	[non PTC]
Fiducial cuts	5%	[CCC]	[PTC]
Acceptance fit	4-2%	[CCC]	[non PTC]
Efficiency fit	2%	[non CCC]	[non PTC]

Chapter 6

Results

6.1 Au + Au collisions at 62.4 GeV

The agreement between Analysis1 and Analysis2 results, as well as between the PbGl and PbSc results from Analysis1 is very good in the two most central bins. Fig. 6.1 shows the ratio of the spectra obtained from the PbSc by Analysis1 and Analysis2, while Fig. 6.2 shows the ratio of the spectra obtained from PbSc by Analysis2 and PbGl by Analysis1. It should be pointed out that even the agreement between the PbSc spectra from Analysis1 and Analysis2 is a non-trivial result. First, because of the very different deadmaps (see 5.2.2) in the two analyses – the deadmap in Analysis1 cuts the PbSc acceptance in half! Also, the way corrections are calculated (including the code itself) is completely different. Therefore, it is fair to say that Figs. 6.1, 6.2 show the agreement of three *essentially independent* analyses.

The final spectrum combines both analyses and the combined spectrum is shown in Fig. 6.3. The combined yield is a point-to-point weighted average of the PbGl and PbSc spectra from Analysis1 and the PbSc spectrum from Analysis2.

The nuclear modification factor R_{AA} (introduced earlier in 5.1) is a measure of how conditions in a heavy ion collision are different from those in nucleon-nucleon collisions. If the value of R_{AA} is consistent with 1, a heavy ion collision can be considered an incoherent superposition of nucleons scattering on nucleons. Any deviation from 1 suggests additional processes taking place.

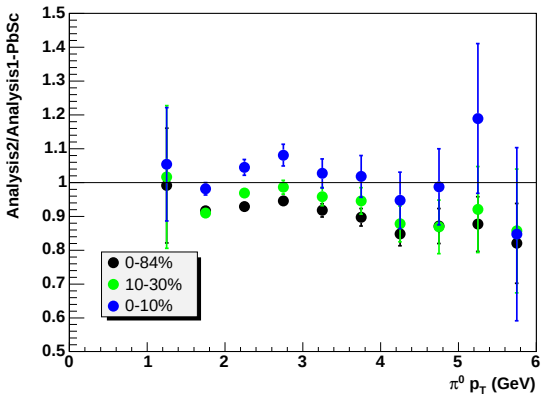

Figure 6.1: Ratio of spectra obtained from the PbSc by Analysis2 and by Analysis1 in $62.4\,\mathrm{GeV}$ $\mathrm{Au}+\mathrm{Au}$ collisions. Error bars are statistical only.

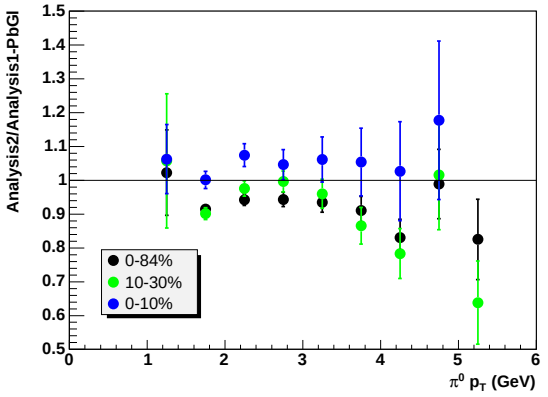

Figure 6.2: Ratio of spectra obtained from the PbSc by Analysis2 and the PbGl by Analysis1 in $62.4\,\mathrm{GeV}$ $\mathrm{Au}+\mathrm{Au}$ collisions. Error bars are statistical.

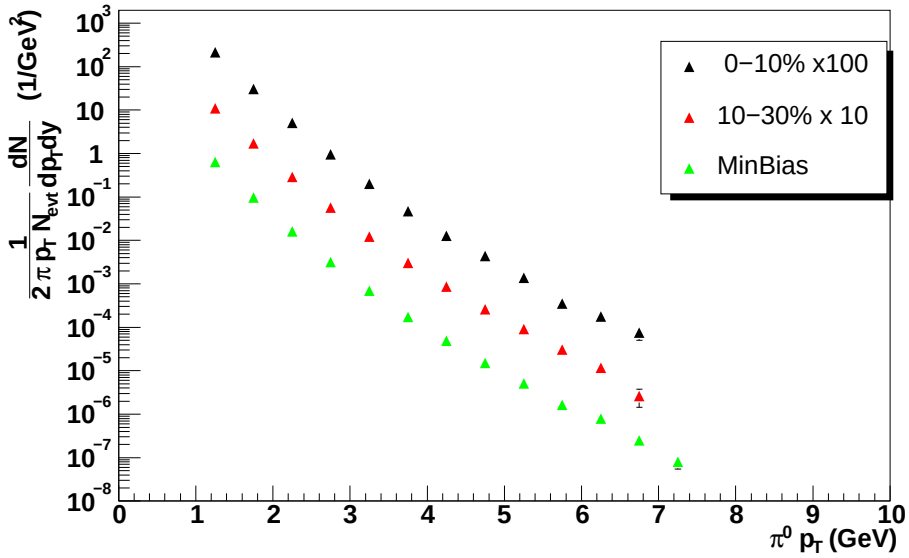

Figure 6.3: Combined (PbSc and PbGl) spectra of neutral pions produced in 62.4 GeV (per nucleon pair) Au + Au collisions.

Since there was no p + p data from RHIC at 62.4 GeV/c, the reference spectrum for calculating the nuclear modification factor (see 5.1) is a fit to the available CERN-ISR data. The procedure is described in detail in [22]. The functional form of the fit is

$$f(p_T) = \frac{A}{(e^{a \cdot p_{\mathrm{T}}^2 + b \cdot p_{\mathrm{T}}} + p_{\mathrm{T}}/p_0)^n} \tag{6.1}$$

with the parameters

$$\begin{aligned} A &= 273.3 \pm 20.4 \ \ [\text{mb GeV}^{-2} c^3] \\ a &= -9.6 \cdot 10^{-3} \pm 1.5 \cdot 10^{-3} \\ b &= 4.67 \cdot 10^{-2} \pm 1.13 \cdot 10^{-2} \\ p_0 &= 2.35 \pm 0.29 \ \ [\text{GeV}/c] \\ n &= 16.42 \pm 1.10\,, \end{aligned}$$

and has a (conservative) 25% error assigned to it. The number of collisions used is 845.4 ± 140.1 for $0 - 10\%$ centrality, 436.2 ± 66.5 for $10 - 30\%$ centrality.

RHIC took data with 62.4 GeV p + p collisions at a later time, so we had a chance to recalculate R_{AA} with PHENIX's own π^0 spectrum taken in p + p collisions. It turned out that our reference spectrum is about 70% higher than the fit the ISR data. The PHENIX data have a 19%, the ISR data a 25% normalization uncertainty, but the difference is higher than what these errors would explain. The effect of this on the calculated R_{AA} is shown in Fig. 6.4.

The plot indicates that π^0 yields in 62.4 GeV central Au + Au collisions are lower than expected from N_{coll}-scaled yields in p + p collisions. By comparing the yields at 62.4 GeV and 200 GeV we can observe that the suppression is not as pronounced as at a higher energy. Suppression sets in gradually with increasing p_{T}. The suppression factor $1/R_{\mathrm{AA}}$ is around 4 to 5 at the highest transverse momenta. More central events are suppressed more.

This suppression can be explained by assuming the formation of a hot and dense medium, which slows down and/or absorbs partons flying out of it. This phenomenon is called *jet quenching*. The results shown here, however, are not conclusive enough to decide whether the dense medium is standard nuclear matter or a medium consisting of deconfined quarks and gluons.

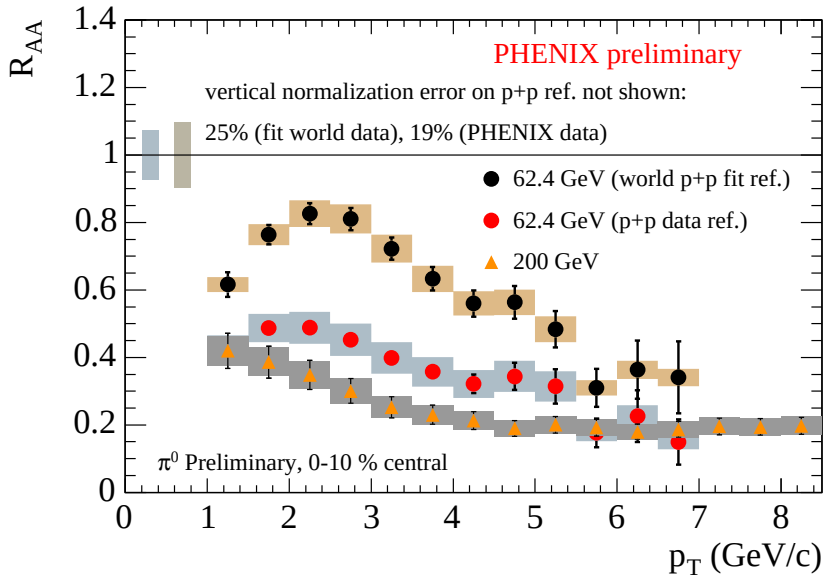

Figure 6.4: Nuclear modification factors for the most central bin (0-10%) of neutral pions produced in $62.4\,\mathrm{GeV}$ (per nucleon pair) $\mathrm{Au} + \mathrm{Au}$ collisions, using two different $\mathrm{p} + \mathrm{p}$ references. The error bars show point-to-point statistical errors; the shaded bands shows the systematic errors which can move all the points up or down together. The $200\,\mathrm{GeV}$ results are also shown for comparison.

6.2 Au + Au collisions at 200 GeV

Fig. 6.5 shows the fully corrected π^0 spectra from minimum bias data and 9 centrality classes. The distributions shown are the combined results of the independent PbSc and PbGl analyses. The spectra are scaled for better visibility.

Fig. 6.6 shows $R_{\rm AA}$ as a function of $p_{\rm T}$ for π^0 in the most central $(0-10\%)$ and the most peripheral $(80-92\%)$ centrality classes. The nuclear modification factor in peripheral data is consistent with 1, thus peripheral collisions seem to be the incoherent superposition of individual nucleon-nucleon collisions. The $R_{\rm AA}$ value for central collisions is significantly less than 1, as opposed to earlier results of enhanced π^0 production at the SPS, CERN (Cronin effect, [20]). The suppression sets in gradually from peripheral to central events. This suppression of neutral pions is smallest around $2\,{\rm GeV}/c$ and is approximately constant at higher transverse momenta. The suppression factor $1/R_{\rm AA}$ is 4-5; the $R_{\rm AA}$ value is $\approx 30\%$ higher than that expected from number-of-participants ($N_{\rm part}$) scaling (dotted line in Fig. 6.6).

Jet quenching calculations based on medium-induced energy loss can reproduce the magnitude of the π^0 suppression assuming the formation of a hot and dense partonic system [21]. The data shown here, however, is not sufficient for us to clearly distinguish between hadronic and partonic energy loss.

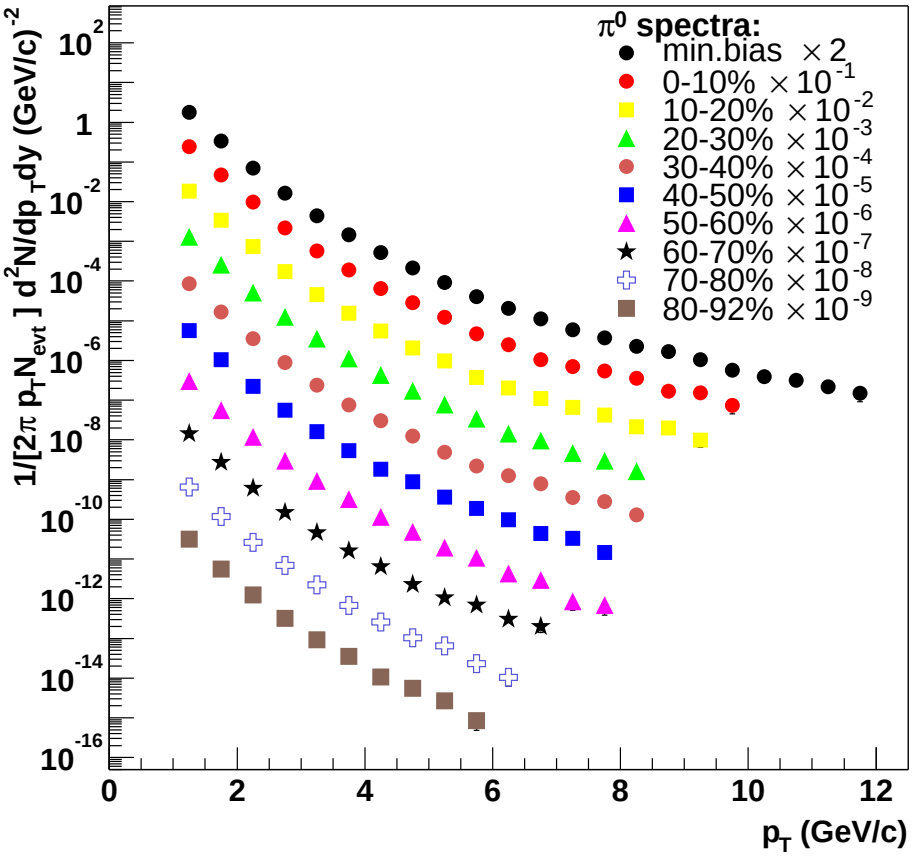

Figure 6.5: Invariant π^0 yields at mid-rapidity as a function of p_T for minimum bias and 9 centralities in 200 GeV (per nucleon pair) Au + Au collisions.

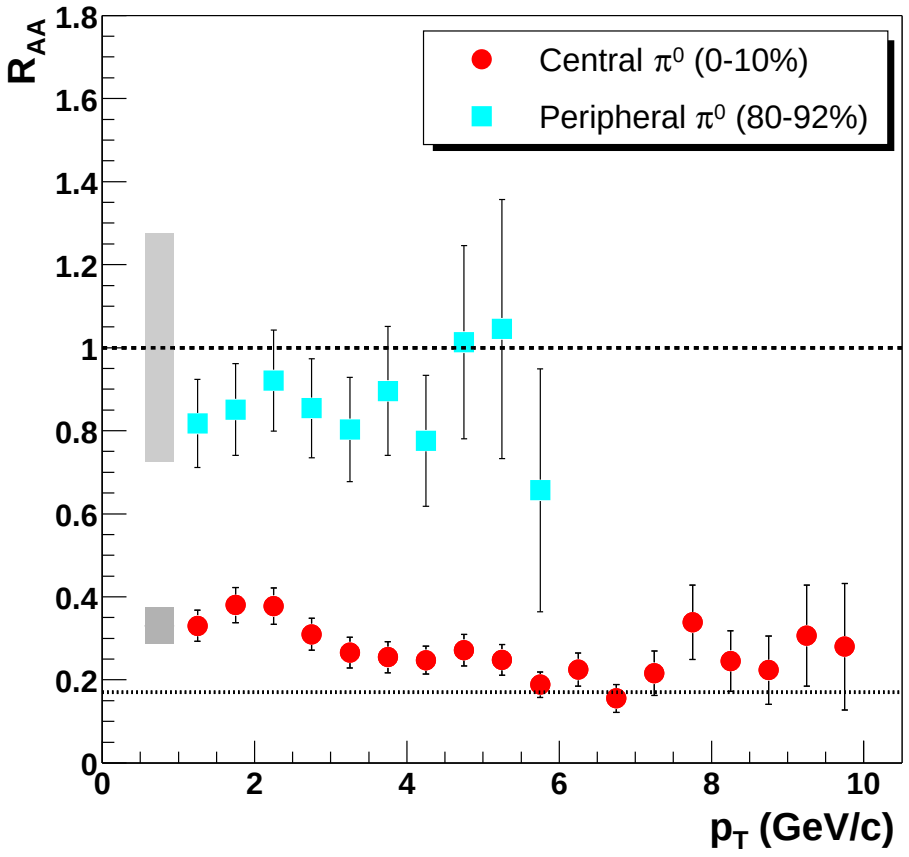

Figure 6.6: Nuclear modification factor for the most central and most peripheral collisions at $200\,\mathrm{GeV}$ (per nucleon pair) using the $200\,\mathrm{GeV}$ $\mathrm{p}+\mathrm{p}$ data from PHENIX as a reference. The error bars show all point-to-point errors, whereas the shaded bands show fractional systematic uncertainties, which can move all the points up or down together.

Chapter 7

Summary

7.1 Introduction

The existence of the Quark-Gluon Plasma is a crucial question in the theory of the strong force. If it exists, we hope that by creating it in accelerators, we would eventually be able to study its properties and gain invaluable knowledge about the nature of the strong force.

Creating the QGP, however, is technologically very challenging. It requires making heavy ions collide with each other in high energy accelerators. Understanding what happens in such a collision is an even more demanding task. Whether or not the QGP is created, the collisions take but a fleeting moment – then all kinds of particles come flying away from the interaction point by the thousands. We catch these particles in huge detector systems, measure their properties and try to analyze them in such a way that would reveal if the QGP has been created. Since we don't know the properties of QGP exactly, we can only surmise what observable effects hint at the formation of the QGP. These observable hints are called the signatures of QGP, and it is the aim of heavy ion experiments to unequivocally show that as many effects as they can measure confirm or disprove the existence of QGP.

This dissertation was written based on the research at the Pioneering High Energy Nuclear Interactions eXperiment (PHENIX) at the Relativistic Heavy Ion Collider (RHIC) of the Brookhaven National Laboratory, USA. One of the design aims behind RHIC was to create a machine which can accelerate heavy ions to energies that would enable us to create the QGP. The detectors built on

RHIC (including PHENIX) are built to measure and identify as many types of processes as possible, exploring several possible signatures of the QGP.

This dissertation describes the details of two analyses, both of which show one (weak) signature of the QGP, the suppression of neutral pions. Before any meaningful physics data can be extracted from the detector, however, its complicated systems need to be carefully calibrated; two such calibration efforts are also shown here.

7.2 Hardware

The PHENIX detector (see Fig. 7.2) at the Relativistic Heavy Ion Collider at Brookhaven National Laboratory is an experiment designed to look for rare processes in heavy ion collisions, with heavy emphasis on photons and leptons. It consists of a number of subsystems of different operating principles. These subsystems work together to provide the means to measuring the properties of dense nuclear matter created in those collisions.

The Electromagnetic Calorimeter (EMCal) is the final stage of the central arm spectrometers in PHENIX. It consists of two different detector subsystems, with one quarter of the central arm acceptance covered by 9216 lead glass (PbGl) Cherenkov modules and the other three quarters by 15552 lead-scintillator (PbSc) sampling calorimeter modules. The calorimeter is located at a radial distance of approximately 5 m from the beam axis in order to maintain an acceptable occupancy in the high particle multiplicity environment of central ("head-on") Au + Au collisions. It covers the range between -0.35 and 0.35 in pseudo-rapidity and $2 \cdot 90°$ in azimuth.

The calorimeter measures position, energy and time of flight of the incoming particles. The energy information is very accurate for electrons and photons, but not for hadrons – most hadrons in the energy range typical of RHIC only deposit part of their energy in the EMCal. Both parts of the calorimeter are equipped with their respective reference systems, the principles of which are very similar, but their implementations differ.

7.3 Calibration

The energy– and timing response of the EMCal have to be calibrated and the "dead" and "hot" towers need to be found before doing any analysis based on the calorimeter. We used a number of methods which complement one another

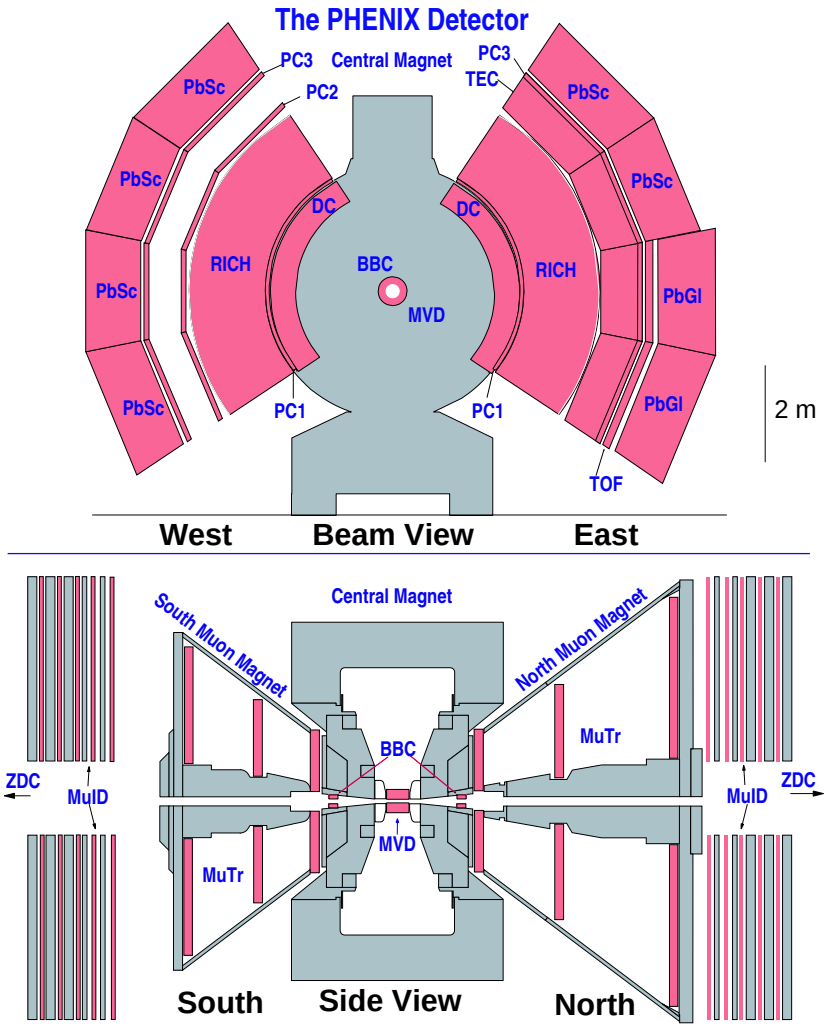

Figure 7.1: Schematic layout of the PHENIX detector in the 2003 RHIC run.

and provide valuable cross-checks. Our calibrations include test beam data from the construction phase; calibration inherited from WA98 (the original owners of our PbGl detector); calibration based on the reference system (both PbSc and PbGl, energy and timing); calibration based on physics data.

In RHIC's second year of running we discovered that the calibration based on the reference system is erroneous and we actually got better results when not using it. As a consequence, it was decided to base our calibrations mostly on physics data.

Finding *dead and hot towers* is done using a statistical approach. We take a sufficiently large data sample; count how many hits the individual hits registered in the sample; plot this hit frequency distribution; and tag towers that are too far off the average as either dead or hot depending on which side of the average they are on. This method has to be applied separately in different energy ranges, because there are towers which do not fire very frequently, but when they do, they indicate an unrealistically high energy.

For *energy calibration*, Minimum Ionizing Particles (MIPs), electrons and neutral pions were used.

Since the EMCal is not a hadron calorimeter, the hadrons created in the high energy collisions at RHIC usually don't stop in the detector, they go through it as Minimum Ionizing Particles. The typical energy deposited by them is almost independent of their total energy and it is characteristic to the calorimeter material. This energy is $\approx 270\,\mathrm{MeV}$ for the PbSc and $\approx 350\,\mathrm{MeV}$ for the PbGl. These values give a stable point of reference on the energy scale.

We can also exploit the fact that, due to their low mass, electrons and positrons are practically always relativistic. That means that their energy and momentum (measured in GeV and GeV/c^2, respectively) are equal. We can use the Ring Imaging Cherenkov detector to identify electrons and our tracking detectors measure their momentum. Energy is measured in the EMCal. Therefore, if we plot the distribution of E/p for electrons, we get a peak around 1. If the peak is not exactly at 1, the position gives us a correction factor for the energy scale. Unfortunately, this method is very statistics-intensive and electrons are produced rarely at RHIC.

Another method for checking and calibrating the energy scale is measuring the mass of neutral pions. Neutral pions decay to two photons, whose energies are accurately measured by the EMCal. The photon pair invariant mass distribution should have a peak at $135\,\mathrm{GeV}/c^2$, the mass of the π^0, which gives us another point in the energy scale. This method is also statistics-intensive, but much less so than the electron method, since neutral pions are produced copiously in heavy ion collisions.

For *timing calibration*, the most obvious choice is photons. We know when a collision occurs, so we know when photons created in a collision should reach the calorimeter. Using a few cuts it is straightforward to collect a photon data sample and the fitting the peak in the distribution of their times of arrival gives us a good estimate of the required shift in timing. The starting point of the time scale is chosen to be the instant when photons created in the collision should reach the front face of the calorimeter. Since the origin of the raw data time scale is chosen quite arbitrarily, we have to shift the photon peaks to conform with this convention. The procedure is the following: we select photons with a few cuts; check where the photon peak lies in the individual towers; and apply offsets to move them to 0. Such fits are shown in Fig. 7.2.

Since the timing response of the towers varies, shifting them by offsets to a common point is essential to getting a good timing resolution. The problem, just like with the energy calibration, is statistics: we have to collect a sufficient number of photons in each tower of the detector to be able to get a good fit of the photon peak – and the calorimeter has 24768 towers. Tracking the changes in the individual channels was not feasible, so we opted for a mixed system: we generated the (fixed) calibration constants for the towers, then changes were tracked on a sector by sector basis. That meant that for the long-time tracking we only needed a set of 8 values, separately determined for every interval in which the detector operating conditions could be considered constant.

The photon timing calibration method was supplemented by hadron timing. In this method, the momentum and path length of charged hadrons are measured by the tracking detectors and the time of arrival by the calorimeter. The mass of the hadrons can be calculated and plotted from these data. If the particle masses come out wrong, one or more of the underlying measurements are inaccurate and have to be corrected.

The *Quality Assurance* at PHENIX in RHIC's second year of running served two purposes: first, to make sure that the data we process is physically meaningful and is not distorted by misbehaving detector parts. Second, with the results gained in assessing data quality we aimed to identify and correct any remaining detector miscalibrations.

The QA procedure of the EMCal developed by me looked at both energy and timing performance of the Electromagnetic Calorimeter. Timing histograms were created for each sector and energy histograms were created for granules (pairs of sectors).

A relatively clean sample of photons was selected with a few cuts to go into the timing histograms. The energy histograms were filled with clusters from minimum ionizing particles. The positions, widths and fit parameters of

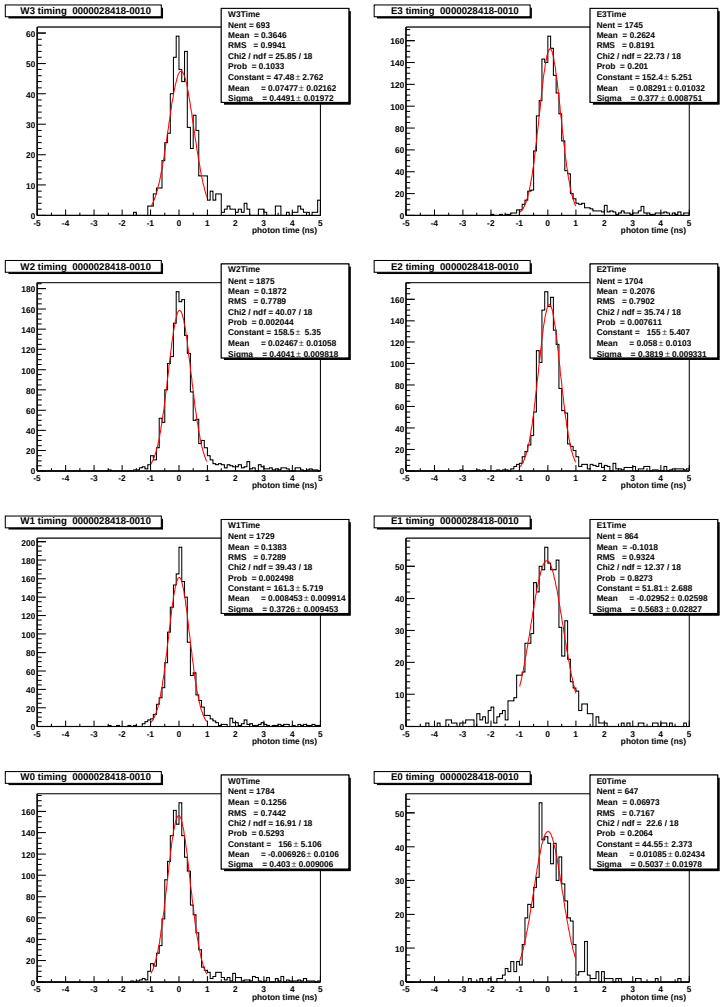

Figure 7.2: The photon peak in the calorimeter in one segment of one detector run for all 8 sectors (the PbGl sectors are E0 and E1 - their timing performance is worse). The fit results are shown in the boxes.

the photon timing peak and the MIP peak were then extracted into the QA summary file. The information collected this way revealed problems with both the energy calibration and timing and serious electronics faults with the West-3 sector of the calorimeter. Using the information from the QA, the calibrations were fine-tuned. Additionally, bad or spurious data were marked as such so that they could be excluded from analyses.

7.4 Experimental Technique

The extraction of neutral pions from the immense number of particles created in nucleus-nucleus collisions and the subsequent analysis thereof is one of the very elegant analyses aimed to reveal the properties of matter at high densities and temperatures. The analysis relies almost entirely on the electromagnetic calorimeter.

Neutral pions decay to two photons with a lifetime of $\approx 10^{-16}\,\mathrm{s}$. Photons travel through the tracking detectors undetected and arrive at the calorimeter, where their energy is fully absorbed. To reconstruct the properties of the parent pion from them, we have to match up the directions and energies with those of their correct partner. Since it is not known which photon belongs to which, reconstruction of individual pions is impossible.

It is, however, possible to make statistical observations about the pions. This is done via the *combination method*, which works as follows. With some loose cuts, we select all particles that are potentially photons; then we make all possible pair combinations of those. With the assumption that the pair came from the same parent, the invariant mass and momentum of this virtual parent are calculated. The distribution of invariant masses will have a large background from the random incorrect combinations. The correct combinations, on the other hand, yield an invariant mass which is around the mass of the π^0, thus resulting in a peak on top of the background at $\approx 135\,\mathrm{GeV}/c^2$.

The amount of combinatorial background is estimated using the *event mixing method*. In event mixing, photons of one event are combined with similar photons of other events. This guarantees that paired photons can not have the same parent, and therefore, there are no correct combinations. Appropriately normalizing their invariant mass distribution, it can be subtracted from the real distribution, which allows the almost complete elimination of the background. The area of the remaining peak yields the number of pions produced under the conditions imposed by the cuts. Doing this as a function of the energy and correcting for systematic effects, a spectrum of the neutral pions can be plotted.

Since the colliding ions are finite-sized, and the processes that occur in the collisions depend heavily on how "head-on" or "glancing" collisions are, we have to be able to characterize them in that respect. For that a variable called *centrality* is used. Events are categorized into centrality classes, for example the $0-10\%$ class means the 10% of the data with the most central collisions [18].

The high particle multiplicity in Au + Au collisions presents a number of technical difficulties. One of these is the overlapping of close showers from two different particles. This effect will increase the apparent mass of the π^0 and depends on the particle multiplicity. Therefore, the more central a collision is, the more the apparent mass shift.

This effect (along with several others) needs to be quantitatively understood, otherwise efficiency corrections to the spectra cannot be calculated. Due to the large multiplicities and the complexity of the PHENIX detector, however, getting large enough data samples with simulated particles and a complete detector simulation is rarely feasible. One of the methods we frequently use to circumvent this difficulty and study systematic effects is *embedding*.

With the embedding method, one generates a simulated particle and the detector's response to it. Then one convolves this information with a real event, effectively getting a simulated particle in a realistic environment – without having to simulate the whole detector's response to hundreds of particles. Analyzing these embedded events one can check what fraction of the simulated particles are reconstructed in the process, and what fraction is lots due to cuts and systematic effects (like overlapping showers). This gives a good estimate on the efficiencies.

To quantitatively characterize the effects of the dense medium created in heavy ion collisions on particle production, we use the nuclear modification factor:

$$R_{\mathrm{AA}} = \frac{\text{Yield in A + A collisions}}{\text{Yield in p + p collisions}} \cdot \frac{1}{N_{\mathrm{coll}}}\,, \tag{7.1}$$

where N_{coll} is the number of individual nucleon-nucleon collisions in a heavy ion event. (Or rather, what the number of individual nucleon-nucleon collisions would be if nucleons as we know them didn't disintegrate in the process.) If R_{AA} significantly differs from 1, that indicates qualitatively different physics in heavy ion collisions – the formation of a dense, strongly interacting medium.

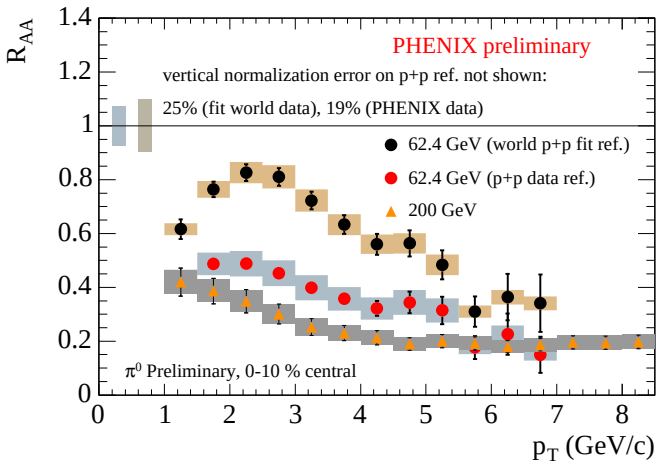

Figure 7.3: Nuclear modification factors for the most central bin (0-10%) of neutral pions produced in 62.4 GeV (per nucleon pair) Au + Au collisions, using two different p + p references. The error bars show point-to-point statistical errors; the shaded bands shows the systematic errors which can move all the points up or down together.

7.5 Results

We measured neutral pion spectra at RHIC in 62.4 GeV and 200 GeV (per nucleon pair) Au+Au collisions. Using p+p data as a baseline, we also calculated the nuclear modification factor as a function of the π^0 transverse momentum p_T (Fig. 7.3). At the time of our analysis, PHENIX did not have any 62.4 GeV p+p data, thus some earlier data were used as a baseline. Later, when PHENIX p + p data became available, R_{AA} was recalculated with the new reference. It turned out that our reference spectrum is about 70% higher than the fit the ISR data. The PHENIX data have a 19%, the ISR data a 25% normalization uncertainty, but the difference is higher than what these errors would explain.

What clearly shows, regardless of the choice of the baseline is that in central events at both energies, pion yields are suppressed. Suppression sets in gradually with increasing p_T and then levels out. The suppression factor $1/R_{AA}$ is around 4 to 5 at high transverse momenta. More central events are suppressed more.

This suppression can be explained by assuming the formation of a hot and dense medium, which slows down and/or absorbs partons flying out of it. This phenomenon is called *jet quenching*. The results shown here, however, are not conclusive enough to decide whether the dense medium is standard nuclear matter or a medium consisting of deconfined quarks and gluons. R_{AA} in Au+Au collisions alone in fact can not answer that question. Later measurements of neutral pion spectra in d + Au collisions, however, provide new clues. Due to the small interaction volume, no dense medium can form in d + Au collisions, thus R_{AA} is expected to be around 1 (no suppression), which was confirmed by the results. This, together with the earlier results, is a very strong argument in favor of the jet quenching explanation of suppression.

Moreover, the 62.4 GeV result had another important consequence: it showed that suppression sets in at a lower collision energy than expected. That in turn means that the dense partonic medium which is responsible for jet quenching already forms at this energy, and thus the critical temperature, the transition point between hadronic and partonic phases lies much lower than expected.

8. fejezet

Összefoglalás

8.1. Bevezetés

A kvark-gluon plazma (QGP) létezése az erős kölcsönhatás elméletének alapvető kérdése. Ha létezik, remélhetjük, hogy gyorsítóberendezésben előállítva előbb-utóbb tanulmányozhatnánk a tulajdonságait, ezáltal roppantul értékes tudásra tennénk szert az erős kölcsönhatás természetéről.

A QGP előállítása azonban technikailag nagyon nagy kihívás. Létrehozásához nehézionokat kell ütköztetnünk nagyenergiás gyorsítókban. Annak megértése viszont, hogy mi történik egy ilyen ütközésben, még monumentálisabb feladat. Akár létrejön a QGP, akár nem, az ütközések egyetlen pillanatig tartanak csupán – majd az ütközési pontból ezrével repül ki mindenféle részecske. Ezeket a részecskéket hatalmas detektorrendszerekben felfogjuk, megmérjük tulajdonságaikat, és megpróbáljuk őket oly módon elemezni, amiből kiderülhet, vajon keletkezett-e QGP. Mivel a QGP tulajdonságait nem ismerjük pontosan, legfeljebb feltételezhetjük, milyen megfigyelhető adatok sejtetik a QGP létrejöttét. Ezeket a jeleket a QGP szignatúráinak nevezzük, és a nehézion-kísérletek célja egyértelműen, minél több szignatúrával bebizonyítani vagy cáfolni a QGP létét.

Ez a disszertáció az amerikai Brookhaven Nemzeti Laboratórium Relativisztikus Nehézion-Ütköztetőjén (RHIC) működő PHENIX kísérletnél végzett kutatásokon alapul. A RHIC-et úgy tervezték, hogy nehézionokat tudjon ütköztetni olyan energián, ami lehetővé teszi a QGP keletkezését. A RHIC-re

épült detektorok (köztük a PHENIX) célja, hogy minél többféle folyamatot tudjanak mérni és azonosítani, a QGP számos szignatúrája után kutatva.

Ez a dolgozat két olyan analízis részleteit írja le, amelyek a QGP egyik (gyenge) szignatúráját, a semleges pionok deficitjét keresik. De mielőtt a detektorból egyáltalán fizikailag értelmes adatokat kapnánk, annak bonyolult rendszereit gondosan kalibrálni kell; két ilyen kalibrációs munkát is bemutatok itt.

8.2. Hardver

A Brookhaven National Laboratory Relativisztikus Nehézion-Ütköztetőjénél (a név angol rövidítéséből: RHIC) dolgozó egyik kísérlet a PHENIX. A PHENIX detektor célja, hogy nehézion-ütközésekben végbemenő ritka folyamatokat keressen, különös tekintettel a fotonok és a leptonok keletkezésére. A detektor számos, különböző elven működő alrendszerből épül fel, amelyek együtt vizsgálják az ütközésekben keltett sűrű közeg tulajdonságait.

Az elektromágneses kaloriméter (EMCal) a PHENIX középső spektrométerkarjának utolsó eleme.

Az EMCal két különböző detektor-alrendszerből áll, éspedig a középső spektrométerkar akceptanciájának negyedét kitevő, 9216 toronyból álló ólomüveg (PbGl) kaloriméterből és a maradék háromnegyedet lefedő, 15552 toronyól álló ólom-szcintillátor (PbSc) kaloriméterből.

A kaloriméter radiálisan kb. 5 m távolságban helyezkedik el a nyalábcsőtől, hogy a centrális („frontális") nehézion-ütközésekben keletkezett nagy számú részecske ellenére is alacsony maradjon a detektor foglaltsága.

Az EMCal pszeudo-rapiditásban a $-0,35$ és $+0,35$ közötti tartományt, azimutszögben $2 \cdot 90°$-ot fed le. A kaloriméter a beérkező részecskék helyét, energiáját és repülési idejét méri. Az energiamérés pontossága igen jó fotonokra és elektronokra, hadronokra viszont nem – a legtöbb, a RHIC-nél szokásos tartományba eső energiájú hadron energiájának csak egy részét adja le az EMCal-ban. A kaloriméter mindkét részéhez tartozik egy optikai elven működő referenciarendszer, amelyek elve nagyon hasonló, de a megvalósításuk különbözik. A referenciarendszer online minőségellenőrzési és kalibrációs lehetőségeket biztosít.

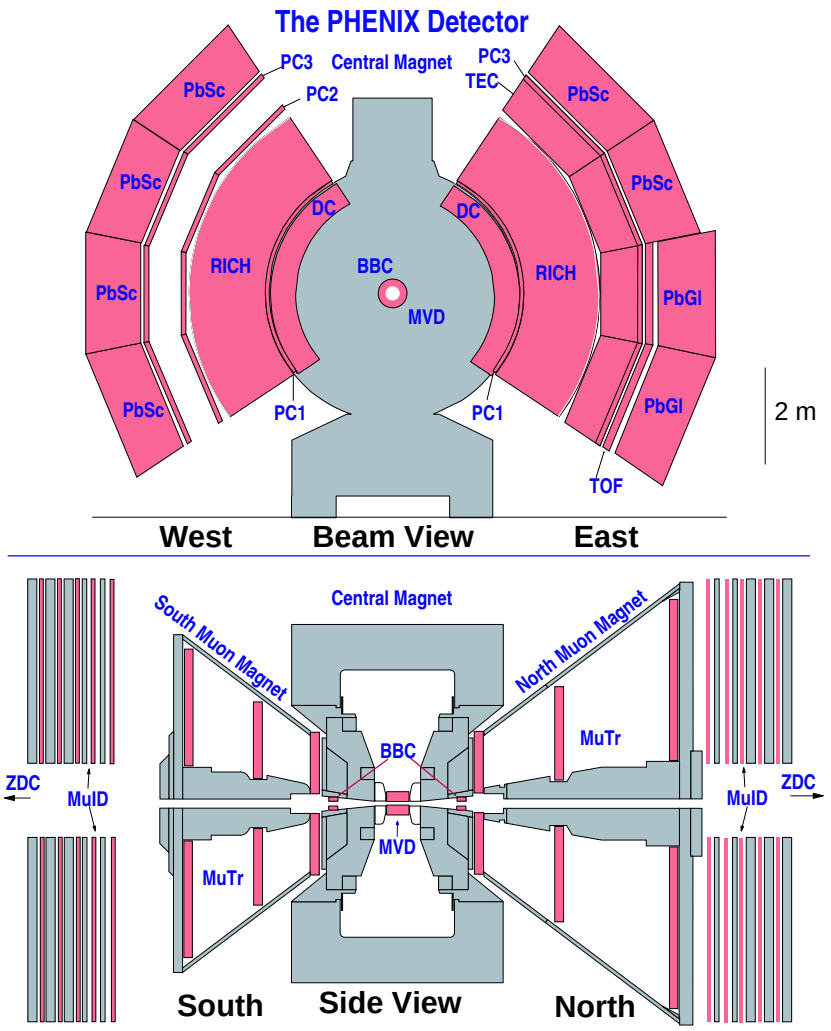

8.1. ábra. A PHENIX detektor 2003-as konfigurációja.

8.3. Kalibráció

Az EMCal energia- és időválaszát kalibrálni kell, továbbá azonosítani kell a „halott" és a „forró" tornyokat, mielőtt a kalorimétert fizikai analízisre használhatnánk. Ehhez számos módszert használunk, amelyek egymást kiegészítik és ellenőrzik. A kalibrációink forrásai: az építés idejéből származó tesztnyalábos vizsgálatok; a WA98 kísérlettől örökölt kalibrációk (a PbGl esetében; eredetileg a PbGl a WA98 része volt); a referenciarendszer; fizikai adatok.

A RHIC működésének második évében felfedeztük, hogy a referenciarendszeren alapuló kalibrálásunk hibás; jobb eredményeket kapunk, ha egyáltalán nem használjuk. Ennek következtében a kalibrációink nagy részét fizikai adatokból nyertük.

A *halott és forró tornyok* keresése statisztikai módszerrel történt. A recept a következő: vegyünk egy megfelelően nagy adatmintát; számoljuk meg, hogy a tornyok egyenként hányszor jeleztek részecsketalálatot; ábrázoljuk a gyakoriságeloszlást; jelöljük meg az ennek átlagától sokkal többször vagy sokkal kevesebbszer részecskét jelző tornyokat forró illetve halott toronyként. Ezt a módszert különböző energiatartományokban külön-külön kell alkalmazni, mert vannak olyan tornyok, amelyek összességében nem jeleznek túl gyakran, de amikor igen, akkor irreálisan nagy energiát.

Az *energiakalibrációra* minimálisan ionizáló részecskéket, elektronokat és semleges pionokat használtunk.

Mivel az EMCal nem hadronkaloriméter, a RHIC nagy energiájú ütközéseiben keltett hadronok nem nyelődnek el a detektorban, hanem minimálisan ionizáló részecskeként haladnak rajta át. A hadronok által az anyagban leadott tipikus energia majdnem teljesen független azok energiájától, de függ az abszorbens anyagi minőségétől. Ez az energia a PbSc detektorban $\approx 270\,\mathrm{MeV}$, a PbGl-ben $\approx 350\,\mathrm{MeV}$. Ezek az értékek kijelölnek egy stabil pontot az energiaskálán.

Kihasználhatjuk azt a tényt is, hogy alacsony tömegük miatt az elektronok és a pozitronok a részecskefizikában gyakorlatilag mindig relativisztikusak. Ez azt jelenti, hogy a GeV-ben mért E energiájuk és a GeV/c^2-ben mért p impulzusuk egyenlőek. Elektronazonosításra a PHENIX-ben használhatjuk a Cserenkovgyűrű-detektorunkat (RICH), az impulzust pedig mérik a nyomkövető detektorok. Az energiát az EMCal méri. Ezért, ha az elektronok E/p eloszlását ábrázoljuk, egy 1 körüli csúcsot kapunk. A csúcs helyének 1-től való eltérése korrekciós tényezőt szolgáltat az energiaskálára. Sajnos ez a módszer

nagyon statisztika-igényes, ráadásul elektronokból meglehetősen kevés keletkezik a RHIC-nél.

Az energiaskála ellenőrzésének és kalibrálásának egy másik módszere a semleges pionok tömegének mérése. A semleges pionok két fotonra bomlanak, amelyek energiájat az EMCal nagy pontossággal méri. A fotonpár invariáns tömegének eloszlását ábrázolva, annak $135\,\mathrm{GeV}/c^2$-nél, a pion tömegénél mutatnia kell egy csúcsot. Ez az energiaskála rögzítéséhez újabb pontot szolgáltat. Ez a módszer szintén statisztika-igényes, de sokkal kevésbé, mint az elektronokkal való kalibrálás, hiszen semleges pionok nagy számban keletkeznek nehézionütközésekben.

Az *időkalibráció* legkézenfekvőbb eszközei a fotonok. Tudjuk, mikor történik egy-egy ütközés, tehát azt is tudjuk, hogy az ütközésben keletkezett fotonoknak mikor kell elérniük a kalorimétert. Néhány vágás segítségével könnyen összegyűjthető egy fotonokból álló adatminta, és ezek érkezési idejének eloszlására illesztett csúcs helyéből megtudhatjuk, mennyivel kell eltolnunk az időskálánkat. A skála nullpontjának azt az időpillanatot választjuk, amikor az ütközésben keltett fotonoknak meg kell érkezniük a kaloriméter felszínére. Mivel a nyers, kalibrálatlan adatokban az időskála origója önkényesen van megválasztva, a fotoncsúcsot úgy kell eltolnunk, hogy az az általunk választott konvenciónak megfeleljen. Az eljárás a következő: néhány vágással fotonokat választunk ki; megnézzük, hol van a fotoncsúcs az egyes tornyokban; majd additív korrekciókkal a 0 pontba mozgatjuk azokat. Ilyen illesztéseket mutat a 8.2. ábra.

Mivel az egyes tornyok időválasza nem egyforma, azok skálájának összehangolása elengedhetetlen feltétele a jó időfelbontásnak. A probléma, csakúgy, mint az energiakalibrációnál, a statisztika: a detektor mind a 24768 tornyában elegendő számú fotont kell „összegyűjtenünk”, hogy a fotoncsúcsot meg tudjuk illeszteni. A változások tornyonkénti követése nem volt megoldható, ezért egy kevert rendszer mellett döntöttünk: a tornyok kalibrációs konstansai időben állandóak, az időbeli változásokat pedig szektoronként korrigáltuk. Ez azt jelentette, hogy a hosszútávú követéshez csak 8 (és nem 24768) korrekcióra volt szükség minden olyan időtartamra, amelyen belül a detektor működési paraméterei nem változtak.

A fotonokkal történő időkalibrálást hadronokkal egészítettük ki. Ezen módszerben szükség van a töltött hadronok impulzusára és úthosszára (amelyeket a nyomkövető detektorok mérnek) és a kaloriméterbe érkezés idejére. Ezekből az adatokból a hadronok tömege kiszámolható és ábrázolható. Ha a származtatott részecsketömegekre pontatlan vagy hibás eredményeket kapunk,

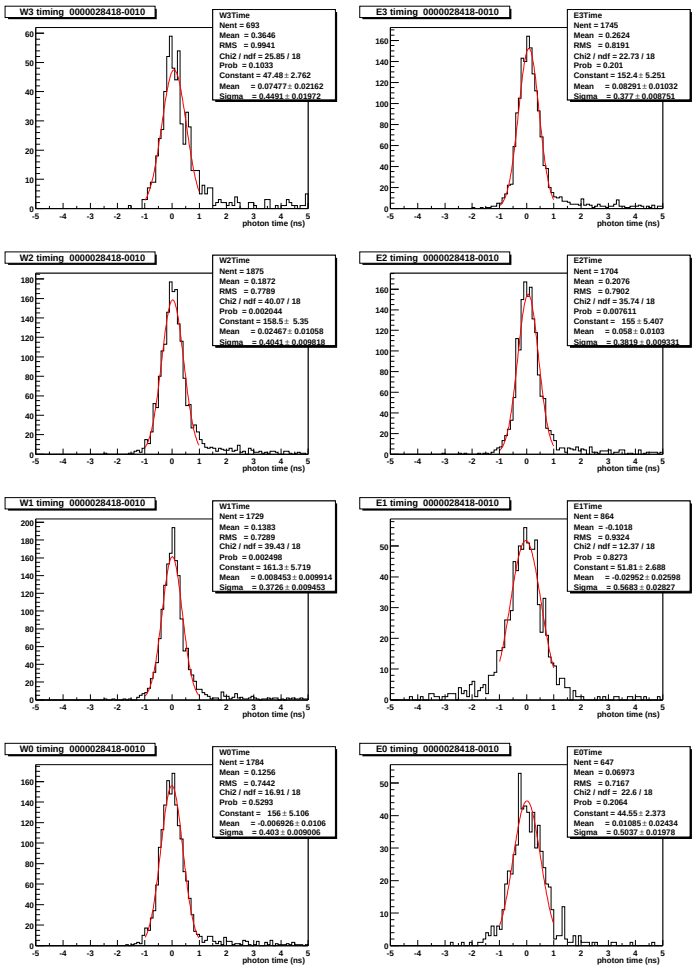

8.2. ábra. A kaloriméterben jelentkező fotoncsúcs egy adatgyűjtési szakasz egy szegmensében, mind a 8 szektorban. (A PbGl szektorok az E0 és az E1 – ezek időfelbontása rosszabb.) Az illesztések eredménye a keretes részen olvasható.

akkor az említett közvetlen mérések közül egy vagy több pontatlan vagy hibás, ami az eredmények alapján korrigálható.

A PHENIX-nél a RHIC második futási évében bevezetett *minőségbiztosítás* (QA) két célt szolgált: egyrészt, hogy meggyőződjünk arról, hogy a feldolgozott adatok fizikailag értelmesek és nem torzítja el őket esetlegesen rosszul működő detektorrészek hatása. Másrészt, az adatminőség kiértékelésében nyert eredményekkel a visszamaradó hibás kalibrációkat akartuk azonosítani és korrigálni.

Az EMCal általam fejlesztett minőségbiztosítási eljárása a kaloriméter energia- és időválaszát is vizsgálta. Első lépésben az adatokból hisztogramokat hoztunk létre; az időhisztogramokat szektoronként, az energiahisztogramokat szektorpáronként generáltuk.

Az időhisztogramokat néhány vágással kapott relatíve tiszta fotonmintával töltöttük. Az energiahisztogramokba minimálisan ionizáló részecskék által leadott energiák kerültek. A fotonok időeloszlásának csúcsát és a minimálisan ionizáló energiacsúcsot megillesztettük, és az illesztés paramétereit szöveges összegzőfájlokba mentettük. Az ily módon gyűjtött információ mind az energiakalibrációval, mind az időkalibrációval kapcsolatban feltárt hibákat; továbbá súlyos elektronikai problémákra hívta fel a figyelmet a kaloriméter nyugati 3. szektorában. A minőségbiztosítás visszajelzésének segitségével a kalibrációkat finomhangoltuk és azok hibáit kijavítottuk. Ezen felül a rossz minőségű vagy „gyanús” adatokat megjelöltük, hogy az analízisekből ki lehessen zárni azokat.

8.4. Kísérleti módszer

Az atommag-atommag ütközésekben keletkezett rengeteg részecske közül a semleges pionok azonosítása és ezt követő analízisük az anyag tulajdonságait nagy sűrűségeken és hőmérsékleten feltáró vizsgálatok egyik nagyon elegáns képviselője. Ez az analízis szinte kizárólag az elektromágneses kalorimétérre támaszkodik.

A semleges pionok $\approx 10^{-16}$ s életidővel két fotonra bomlanak. A fotonok a nyomkövető detektorokon detektálás nélkül haladnak át, és a kalorimétérben teljes energiájukat leadva elnyelődnek. Ahhoz, hogy az eredeti pion tulajdonságait rekonstruáljuk belőlük, az egyes fotonok irányát és energiáját össze kell párosítanunk a párjukéval. Mivel azt nem tudhatjuk, melyik foton melyikhez tartozik, az egyes pionok rekonstrukciója nem lehetséges.

Statisztikus alapon azonban lehet megfigyeléseket tenni a pionokról. Ez a *kombinációs módszer* révén történik, amely a következőképpen működik.

Néhány nem túl szigorú vágással kiválasztjuk azokat a részecskéket, amelyek potenciálisan fotonok; majd ezekből generáljuk az összes lehetséges párkombinációt. Feltételezve, hogy az ilyen párok mindkét fotonja ugyanabból a pionból jött, kiszámoljuk a anyarészecske invariáns tömegét és impulzusát. Az invariáns tömegek eloszlásának nagy háttere lesz a véletlenszerű helytelen kombinációkból; a helyes kombinációk viszont a π^0 tömegéhez közeli eredményeznek, így a háttéren kapunk egy csúcsot $\approx 135\,\mathrm{GeV}/c^2$-nél.

A kombinatorikus hátteret az *eseménykeverés* módszerével becsüljük meg. Az eseménykeverés során egy eseményből származó fotonokat egy másik eseményből származó hasonló fotonokkal párosítunk össze. Ez garantálja, hogy az ilyen párok biztosan nem származhatnak ugyanabból a részecskéből, tehát nincs pioncsúcs. Ezt az eloszlást megfelelően normálva levonhatjuk a valódi eloszlásból, ami a háttér majdnem tökéletes kiküszöbölésével jár. A visszamaradó csúcs területe a vágások jelentette megszorításokkal keltett pionok számát szolgáltatja. A pion energiájának függvényében elvégezve ezeket a műveleteket és a a szisztematikus hibákat korrigálva, felvehető a semleges pionok spektruma.

Mivel az ütköző ionok véges méretűek, továbbá az ütközésekben zajló folyamatok erősen függnek attól, mennyire „frontális" illetve „súroló" az ütközés, tudnunk kell jellemeznünk őket ilyen szempontból. Erre egy *centralitás* nevű változót használunk. Az eseményeket centralitásosztályokba soroljuk, például a $0-10\%$ centralitásosztály az ütközések legcentrálisabb 10%-ából származó adatokat jelenti.

Az Au + Au ütközésekben egyszerre keletkező sok részecske egy sor technikai problémát eredményez. Ezek egyike, hogy a kaloriméterbe egymáshoz közel megérkező két részecske által keltett zápor átfedheti egymást. Ez az effektus a π^0 látszólagos tömegét megnöveli, és mértéke az egyszerre keletkezett részecskék számától függ. Ezért minél centrálisabb egy ütközés, ez a tömegeltolódás annál hangsúlyosabban jelentkezik.

Ezt az effektust és más hasonlóakat kvantitatívan is meg kell értenünk, különben a spektrum hatásfokkorrekcióit nem lehet elegendő pontossággal meghatározni. A nagy részecskeszámok és a PHENIX detektor komplexitása miatt azonban elegendő mennyiségű részecske keltését és ezekre a teljes detektor válaszát szimulálni gyakorlatilag nem kivitelezhető. Az egyik módszer, amivel ezen nehézség megkerülésével mégis tudunk szisztematikus hibákat becsülni, a *beágyazás*.

A beágyazás módszerénél generálunk egy szimulált részecskét és a detektor válaszát a részecskére, majd ezt az információt beágyazzuk egy valódi esemény adatai közé. Így kaptunk egy szimulált részecskét realisztikus környezet-

ben, anélkül, hogy szimulálnunk kellett volna a detektor válaszát több száz részecskére. Ezen eseményeket analizálva ellenőrizhetjük, hogy a szimulált részecskék mekkora hányadát rekonstruáljuk helyesen, és mekkora hányadát veszítjük el a vágások és a szisztematikus effektusok (mint például az egymást átfedő záporok) miatt. Ezzel a módszerrel a hatásfokok jól megbecsülhetők.

A nehézion-ütközésekben keletkezett sűrű közegnek a részecskehozamokra gyakorolt hatását a „maganyag-módosultsági tényezőt" használjuk:

$$R_{\mathrm{AA}} = \frac{\text{Hozam A + A ütközésekben}}{\text{Hozam p + p ütközésekben}} \cdot \frac{1}{N_{\mathrm{coll}}}\,, \tag{8.1}$$

ahol N_{coll} az egyedi nukleon-nukleon ütközések száma egy nehézionos eseményben. (Pontosabban, amennyi az egyedi nukleon-nukleon ütközések száma lenne, ha a nukleonok nem esnének darabjaikra a folyamat során.) Ha R_{AA} jelentősen eltér 1-től, az a nehézion-ütközésekben kvalitatíve más fizika működésére, egy sűrű, erősen kölcsönható közeg létrejöttére utal.

8.5. Eredmények

Meghatároztuk a semleges pionok spektrumát a RHIC nukleonpáronként 62.4 GeV és 200 GeV energiájú Au + Au ütközéseiben. Viszonyítási alapként p + p ütközésbeli adatokat használva kiszámoltuk a maganyag-módosultsági tényezőt a π^0 p_{T} transzverzális impulzusa függvényében (8.3. ábra). Munkánk idején a PHENIX még nem rendelkezett 62.4 GeV-en gyűjtött p + p adatokkal, így viszonyítási alapként más kísérletek korábbi eredményeit használtuk. Később, amikor a PHENIX is gyűjtött adatokat ilyen energiájú p + p ütközésekben, az R_{AA}-t újraszámoltuk az új viszonyítási alappal. Kiderült, hogy a mi referenciaspektrumunk kb. 70%-kal magasabban van, mint a CERN-i ISR adatokra illesztett görbe. A PHENIX adatainak 19%, az ISR adatainak 25% normálási bizonytalansága van, de az eltérés így is nagyobb, mint amit ezek a hibák megnyugtatóan megmagyaráznának.

Ami a viszonyítási alap megválasztásától függetlenül világosan látszik, az az, hogy centrális eseményekben a pionok hozama mindkét energián alacsonyabb a vártnál. A deficit a p_{T} függvényében egy darabig fokozatosan nő, majd állandóvá válik. Az $1/R_{\mathrm{AA}}$ deficittényező magas transzverzális impulzusoknál 4 és 5 közötti. A centrális eseményekben jobban csökken a hozam.

Ez a deficit magyarázható egy forró, sűrű közeg kialakulásának feltételezésével, amely a belőle kifelé repülő partonokat lelassítja és/vagy elnyeli. Ezt a jelenséget *jetkioltásnak* nevezzük. Az itt bemutatott eredmények

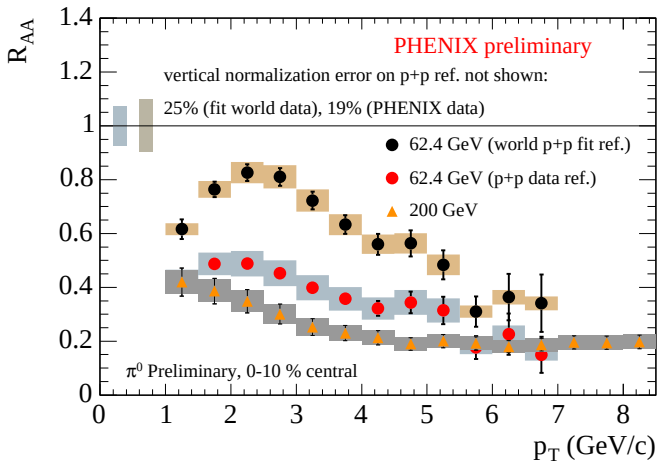

8.3. ábra. Nukleonpáronként $62.4\,\mathrm{GeV}$-es centrális (0-10%) $\mathrm{Au}+\mathrm{Au}$ ütközésekben keletkezett semleges pionok spektrumából számolt magmódosultsági tényező, két különböző viszonyítási alapot használva. A pontonkénti hibák a statisztikus bizonytalanságot jelzik, az $R_{\mathrm{AA}}=1$ körüli színes sávok a szisztematikus hibákat, amelyek az összes pontot egyszerre, egy irányba mozdíthatják.

azonban nem perdöntőek; ezekből nem tudjuk megmondani, hogy a sűrű közeg hagyományos maganyag-e vagy egy kiszabadult kvarkokból és gluonokból közeg. Az $\mathrm{Au}+\mathrm{Au}$ ütközésekben meghatározott R_{AA} erre önmagában nem is tud választ adni. A pionok spektrumának későbbi, $\mathrm{d}+\mathrm{Au}$ ütközésekben történt meghatározása azonban új nyomokat szolgáltat. A kis kölcsönhatási térfogat miatt a $\mathrm{d}+\mathrm{Au}$ ütközésekben ugyanis nem alakulhat ki sűrű közeg, így azt várjuk, hogy az R_{AA} 1 körül lesz (azaz nincs deficit); ezt az eredmények megerősítették. A korábbi eredményekkel együtt ez nagyon erős érv a jetkioltási magyarázat helyessége mellett.

A $62.4\,\mathrm{GeV}$-es eredménynek volt továbbá még egy fontos következménye: megmutatta, hogy az elnyomás a vártnál alacsonyabb energián is működik. Ez azt jelenti, hogy a jetkioltásért felelős sűrű partonikus anyag már ezen az energián is keletkezik, tehát a kritikus hőmérséklet, a fázisátmenet a hadronikus és a partonikus anyag között a vártnál sokkal alacsonyabb energián keresendő.

Bibliography

[1] J. C. Collins, M. J. Perry, Superdense matter: Neutrons or asymptotically free quarks?, Phys. Rev.. Lett. 34 (1975) 1353.

[2] E. V. Shuryak, Quantum Chromodynamics and the theory of superdense matter, Phys. Rept. 61 (1980) 71–158

[3] Formation of dense partonic matter in relativistic nucleus-nucleus collisions at RHIC: Experimental evaluation by the PHENIX collaboration, Nucl. Phys. A **757** (2005) 184 [arXiv:nucl-ex/0410003].

[4] M. Gyulassy, P. Levai, I. Vitev, Nucl. Phys. B**571**, 197 (2000); Nucl. Phys. B**594**, 371 (2001); Phys. Rev. Lett. **85**,5535 (2000)

[5] RHIC project overview, Nuclear Instruments and Methods in Physics Research A 499 (2003) 235–244

[6] ISABELLE
`http://en.wikipedia.org/wiki/ISABELLE`

[7] Siberian Snakes in High-Energy Accelerators, J. Phys. G: Nucl. Part. Phys. **31** (2005) R151–R209

[8] PHENIX detector overview, Nuclear Instruments and Methods in Physics Research A 499 (2003) 469–479

[9] PHENIX magnet system, Nuclear Instruments and Methods in Physics Research A 499 (2003) 480–488

[10] The RHIC Zero Degree Calorimeters, Nuclear Instruments and Methods in Physics Research A 499 (2003) 433–436

[11] PHENIX Central Arm Tracking Detectors, Nuclear Instruments and Methods in Physics Research A 499 (2003) 489–507

[12] PHENIX Central Arm Particle ID detectors, Nuclear Instruments and Methods in Physics Research A 499 (2003) 508–520

[13] PHENIX Muon Arms, Nuclear Instruments and Methods in Physics Research A 499 (2003) 537–548

[14] PHENIX Muon Arms, Nuclear Instruments and Methods in Physics Research A 499 (2003) 537–548

[15] Physics analysis with the PHENIX electromagnetic calorimeter, 2004 IEEE Nuclear Science Symposium Conference Record

[16] EMCAL QA study, 04/19-04/25/2002 (PHENIX internal note)
`https://www.phenix.bnl.gov/WWW/p/draft/ptarjan/QAstudy`

[17] Glauber model for heavy ion collisions from low energies to high energies, P. Shukla, nucl-th/0112039

[18] Using multiplicity as a fractional cross-section estimation for centrality in PHOBOS, Richard S. Hollis *et al* 2005 *J. Phys.: Conf. Ser.* **5** 46-54

[19] Pizero Measurement at PHENIX – Corrected minimum bias spectrum, S. Botelho *et al.*, PHENIX Analysis Note 031
`https://www.phenix.bnl.gov/phenix/WWW/p/info/an/031/`

[20] Production of Hadrons at Large Transverse Momentum in 200-GeV, 300-GeV and 400-GeV pp and pn collisions, D. Antreasyan *et al.*, Phys. Rev. **D19**, 764 (1979)

[21] Suppressed π^0 Production at Large Transverse Momentum in Central Au + Au Collisions at $\sqrt{s_{NN}} = 200\,\mathrm{GeV}$, S. S. Adler *et al.* (PHENIX Collaboration), Phys. Rev. Lett. 91, 072301 (2003)

[22] Nucleon-nucleon reference p_{T} distribution for inclusive pi^0 production in Au+Au collisions at $sqrts_{NN} = 62.4$ GeV", D. d'Enterria, *PHENIX Analysis Note 291*,
`https://www.phenix.bnl.gov/phenix/WWW/p/info/an/291/`

Appendix A

List of acronyms

ADC Analog-to-Digital Converter
AGEL Aerogel (material/detector)
AGS Alternating Gradient Synchrotron
BBC Beam-Beam Counter
BNL Brookhaven National Laboratory
BRAHMS Broad RAnge Hadron Magnetic Spectrometer
CERN Organization Européenne pour la Recherche Nucléaire (European Organization for Nuclear Research)
CM Central Magnet
DC Drift Chamber
EMCal ElectroMagnetic Calorimeter
FastMC Fast Monte Carlo simulation, a way to estimate systematic errors in PHENIX
FEE Front End Electronics
FODO Focusing-0-Defocusing-0 (a set of quadrupole magnets in an accelerator which focus the beam along both the x and the y axis)
HIJING Heavy Ion Jet INteraction Generator (particle generating code for simulation)
ISABELLE Intersecting Storage Accelerator + "belle" (cancelled accelerator project at BNL)
ISR Intersecting Storage Rings (an accelerator at CERN)
LED Light Emitting Diode
MIP Minimum Ionizing Particle/Peak
MMN Muon Magnet North
MMS Muon Magnet South

MuIdN Muon Identifier North
MuIdS Muon Identifier South
MuTrN Muon Tracker North
MuTrS Muon Tracker South
MVD Multiplicity-Vertex Detector
Nd:YAG Neodymium Yttrium-Aluminum-Garnet (laser)
NTC Normalization Trigger Counter
ONCS ONline Computing System
PbGl Lead Glass, part of the Electromagnetic Calorimeter in PHENIX
PbSc Lead-Scintillator "sandwich", part of the Electromagnetic Calorimeter in PHENIX
PC Pad Chamber
PID Particle IDentification
PIN Positive-Intrinsic-Negative semiconductor (photodiode)
PHENIX Pioneering High Energy Nuclear Interactions eXperiment
PHOBOS not an acronym: Phobos is a moon of Mars, which was the name of the original proposed detector
PMT PhotoMultiplier Tube
POPOP 1,4-bis(5-phenyloxazol-2-yl)benzene, a liquid scintillator
PTP p-terphenyl, a scintillating material
QA Quality Assurance
QCD Quantum ChromoDynamics
QM Quark Matter (conference)
QGP Quark-Gluon Plasma
R&D Research and Development
RCF RHIC Computing Facility
RHIC Relativistic Heavy Ion Collider
RICH Ring Imaging CHerenkov (detector)
RIKEN RIkagaku KENkyusho (Japanese organization for science and technology)
SMD Shower Max Detector
SPS Super Proton Synchrotron (an accelerator at CERN)
STAR Solenoidal Tracker At RHIC
SVT Silicon Vertex Detector
TDC Time-to-Digital Converter
TEC Time Expansion Chamber
TOF Time Of Flight (detector)
ToF Time of Flight (quantity)
TPC Time Projection Chamber
ZDC Zero Degree Calorimeter

Appendix B

Publications relevant to the dissertation

Papers:

1. Suppressed π^0 Production at Large Transverse Momentum in Central Au + Au Collisions at $\sqrt{s_{NN}} = 200\,\mathrm{GeV}$, S. S. Adler *et al.* (PHENIX Collaboration), Phys. Rev. Lett. 91, 072301 (2003)

2. Mid-rapidity neutral pion production in proton-proton collisions at $\sqrt{s} = 200\,\mathrm{GeV}$ S. S. Adler *et al.* (PHENIX Collaboration), Phys. Rev. Lett. **91** (2003) 241803 [arXiv:hep-ex/0304038].

3. Absence of suppression in particle production at large transverse momentum in $\sqrt{s_{NN}} = 200\,\mathrm{GeV}$ d+Au collisions,S. S. Adler *et al.* (PHENIX Collaboration), Phys. Rev. Lett. **91** (2003) 072303 [arXiv:nucl-ex/0306021].

4. Formation of dense partonic matter in relativistic nucleus nucleus collisions at RHIC: Experimental evaluation by the PHENIX collaboration, K. Adcox *et al.* (PHENIX Collaboration), Nucl. Phys. A **757** (2005) 184 [arXiv:nucl-ex/0410003].

Proceedings:

1. Physics analysis with the PHENIX electromagnetic calorimeter, IEEE NSS-MIC Conference Record (Rome, 2004)

Posters, talks:

1. New Results from the PHENIX experiment at RHIC, NPDC17 conference (Debrecen, 2002)
2. Physics analysis with the PHENIX electromagnetic calorimeter, IEEE NSS-MIC Conference Record (Rome, 2004)
3. Physics analysis with the PHENIX Electromagnetic Calorimeters, 4th Budapest Winter School on Heavy Ion Physics (Budapest, 2004)